HYDROLOGICAL MODELING IN THE MARMOT CREEK BASIN

YANZHEN OU

Hydrological Modeling in the Marmot Creek Basin

By

©Yanzhen Ou

A thesis submitted to the school of graduate studies

in partial fulfillment of the requirement for

the degree of Master of Engineering

Faculty of Engineering and Applied Science

Memorial University of Newfoundland

August 2009

ST. JOHN'S NEWFOUNDLAND AND LABRADOR CANADA

Acknowledgements

I am very grateful to my supervisor, Dr. Ken Snelgrove, for his constant guidance, feedback, encouragement, and for keeping me focused in my research. During the past two years, Dr. Snelgrove has given me consistent trust and support which greatly encouraged me to improve and finish my work.

I have to acknowledge Mr. Sitotaw Yirdaw and Mr. Clement Agboma who always encouraged me and helped me. I would also thank Dr. Wolock and Dr. Beven who provided me with FORTRAN source codes and gave me precious suggestions. Lots of thanks go to the IP3 research network for providing me with the hydrologic data used in this study.

This is also a chance to thank all rest of the friends in the Memorial University of Newfoundland during these years. Special thanks to Jing Ping, Liang Jing, Haijie Cai, Pu Li, Yao Xu, Xiao Jiang, and Rashed for their precious friendship and their co-operation as well as valuable suggestions.

I have to thank the funding of Memorial University, CFCAS, IP3 research network for their financial support.

I am also indebted to my parents. Thank you for you continuous support and love during two years of my Master study.

I would like to thank my husband, Shiliang Lu, for his selfless supporting and encouraging me to pursue this degree.

Abstract

Two primary purposes of this research were to assess the hydrologic response and to detect the hydrologic similarity of a 9.5 km^2 needle-leaf forested watershed in the Canadian Prairie province of Alberta known as the Marmot Creek basin. In order to achieve these two objectives, three hydrologic models and several analysis methods were applied in this study.

Topographic index, $\ln(a/\tan\beta)$, was calculated by different flow routing algorithms (single flow and biflow direction algorithms) with 1- and 90-meter resolution digital elevation models (DEM) in this research. A series of maps and tabular outputs showed that in high resolution DEM, the distinction of the frequency distribution of $\ln(a/\tan\beta)$ was pronounced between different algorithms. However, in low resolution DEM, the difference was not obvious.

Evaporative resistances (stomatal and aerodynamic), which was used to calculate potential evapotranspiration (PET), was estimated by Canadian Land Surface Scheme (CLASS). Aerodynamic resistance was also produced by the Monteith method (1965) under neutral conditions. The maximum stomatal resistance in the Marmot Creek basin could reach 2000 m s^{-1}; however, the minimum value was only 0 m s^{-1}. A series of

comparisons showed that aerodynamic resistance computed by CLASS and Monteith method (1965) were fairly close.

PET, as one of the input data sets to drive TOPMODEL in this research, was estimated by Penman-Monteith formulation. The peak of PET over the Marmot Creek basin occurred in July, and October had the lowest rate, which was equal to half the peak value in July. The effects of evaporative resistances on PET were also discussed. From the results, it could be concluded that compared to aerodynamic resistance, stomatal resistance had main control of PET.

TOPMODEL, a topographically-based hydrologic model, was used to assess the hydrologic response in the Marmot Creek basin. This hydrologic model was combined with genetic algorithm (GA) to do calibration and, subsequently, validation with historical streamflow datasets retrieved from the Environment Canada hydrometric database. According to streamflow simulation with TOPMODEL, subsurface flow accounted for 84.9% of the total simulated streamflow during the calibration periods for the Marmot Creek basin. The simulations yielded a Nash-Sutcliffe efficiency of about 0.611, which was acceptable given the limitations of climate data. However, during the validation phase of the model assessment, there were some discrepancies between the simulated streamflow response and the observed values. Moreover, different $\ln(a/\tan\beta)$ distributions were observed using different grid sizes in different flow direction algorithms, but these did not lead to significant departures in all the cases of the simulated streamflow.

Four-meter resolution IKONOS images were used to perform land cover classification in the Marmot Creek basin through a Decision Tree classifier using Normalized Difference

Vegetation Index (NDVI) input. The variation of $\ln(a/\tan\beta)$ between different land covers was investigated using one-way analysis of variance (ANOVA). The results of ANOVA showed that no obvious relationship between $\ln(a/\tan\beta)$ and the land cover classes could be determined.

Table of Contents

List of Figures

List of Tables

List of Nomenclature

ANOVA	Analysis of Variance
CFCAS	Canadian Foundation for Climate and Atmospheric Sciences
CLASS	Canadian Land Surface Scheme
D8	Single flow direction algorithm
D∞	Biflow direction algorithm
DEM	Digital Elevation Model
DEMON	Digital Elevation Model Network algorithm
ET	Evapotranspiration
FD8	Multiple flow direction algorithm
GA	Genetic Algorithm
IP3	Improved Processes and Parameterization for Prediction in Cold Regions
LAI	Leaf Area Index
NDVI	Normalized Difference Vegetation Index
PET	Potential Evapotranspiration

PET_e	Potential Evapotranspiration with aerodynamic resistance is obtained from CLASS.
PET_n	Potential Evapotranspiration with the aerodynamic resistance computed under neutral conditions
RPC	Rational Polynomial Coefficient
SRMAX	Maximum Value of Storage in Root Zone
SRTM	Shuttle Radar Topography Mission
SRZ	Root Zone Storage
SUZ	Unsaturated Zone Moisture Storage
SVAT	Soil-Vegetation-Atmosphere Transfer Scheme
TOPMODEL	The Topographic-Based Hydrologic Model
USGS	United States Geological Survey
VI	Vegetation Index

Chapter 1

Introduction

1.1. Background

This study is part of the ongoing IP3 (**Improved Processes and Parameterization for Prediction**) research network being funded by the Canadian Foundation for Climate and Atmospheric Sciences (CFCAS). IP3 network spans a period of four years commencing in 2006 and ending in 2010. The primary objective of the IP3 network is geared towards improving the understanding of hydrology and weather systems in cold regions that remain poorly understood but are critical for developing a predictive capability for weather and water resource. Understanding of the underlying hydrologic processes, especially as they relate to the cold region, is of high importance in water management and policy making for agriculture, communities, recreation, sustainable industrial development, and environmental conservation in western and northern Canada.

As part of the many tasks the IP3 research network is involved, the estimation of streamflow from ungauged basins is the most important one. Measured streamflow,

presenting the integrated hydrologic response of a watershed, is a fundamental requirement for water supply. An understanding of the streamflow generation processes from a catchment is a prerequisite for conceptualizing how water interacts with rocks and sediments in that catchment. Incidentally, hydrologic models, otherwise known as watershed models, can provide a way to assess streamflow generation mechanisms from a catchment. These rely on modeling input such as precipitation and temperature fields. From a hydrologic modeling perspective, simulated runoff can be considered to be quick or slow depending on the associated mechanism involved in its formation.

Topography is recognized as an important factor for the spatial patterns of hydrological response at catchment scales. Beven and Kirkby (1979) developed the topographic index to describe steady-state moisture storage as a function of topography, where local hillslope segment slope is used as a surrogate for the hydraulic gradient. Use of this terrain index has enabled an incorporation of spatial heterogeneity on the scale of the hillslope in a hydrologic model called TOPMODEL.

TOPMODEL was first developed by Beven and Kirkby (1979). This model is one of the few conceptual models that account explicitly for the saturation excess overland flow mechanism and integrate the variable contributing area concept into their parameterization. This model has a simple but mathematically elegant conceptual basis that allows distributed predictions of hydrological processes whilst maintaining parametric and computational efficiency. It is a suitable model for hillslope watersheds, and reasonably simulates the effects of watershed topography on hydrologic response. The underlying physics in this model is robust for predicting the spatial distribution of water content and lateral flows at the time step of the model.

The Marmot Creek basin in Western Canada is one of the research basins being used to develop and test the regional water cycle by the IP3 research network. This basin is selected in our study, as water well records exist with the basin to validate and test the models. Stream system of the Marmot Creek basin is small mountain drainage on the eastern slope of the Rocky Mountain and is located at longitude 115°10'W and latitude 50°57'N, which is about 110 km southwest of Calgary, Alberta.

1.2. Objectives

Two primary purposes of this research are to assess the hydrologic response and to detect the hydrologic similarity of the Marmot Creek basin. In order to achieve these two objectives, three hydrologic models (TOPMODEL, CLASS, and Penman-Monteith approach) and several analysis methods are implemented in this study. These models and methods extend the objectives of this study, which can be concluded:

i) To estimate the topographic index using single flow direction and biflow direction algorithms with 1- and 90-meter resolution digital elevation model (DEM), and to determine the effects of flow direction and the grid size of DEM on the runoff generation.

ii) To estimate the potential evapotranspiration over the Marmot Creek basin using the Penman-Monteith approach (Monteith, 1965). Additionally, to ascertain the effects of stomatal resistance and aerodynamic resistance on potential evapotranspiration.

iii) To assess the adequacy of the TOPMODEL application in the Marmot Creek basin as well as obtain the best possible reproduction of observed streamflow with realistic values of model parameters.

iv) To undertake the calibration of TOPMODEL by using Genetic Algorithm (GA) approach to arrive at a best-fit parameter set.

v) To ascertain the correlation, if any, between the soil moisture deficits with the topographic index from the simulation results of TOPMODEL. The relationship between this topographic index and the land cover classes across the Marmot Creek basin would also be undertaken.

1.3. Organization of the Thesis

There are 9 chapters in this thesis. Chapter 2 presents a review of literature concerning topographic index, potential evapotranspiration, TOPMODEL, and vegetation cover. Chapter 3 provides a description of the study area and the data collected. Chapter 4 calculates the topographic index using the single flow and the biflow direction algorithms with 1- and 90-meter resolution DEMs. Chapter 5 uses CLASS to simulate stomatal resistance and aerodynamic resistance. Aerodynamic resistance is also estimated by Monteith method (1965) under neutral boundary condition. Chapter 6 estimates the potential evapotranspiration using the Penman-Monteith method with the stomatal resistance and aerodynamic resistance data from chapter 5, and compares the two sets of potential evapotranspiration values computed with different aerodynamic resistance. Chapter 7 describes the framework of TOPMODEL, and discusses the results with three topics: i) model calibration and validation, ii) effects of spatial variability on streamflow simulation, and iii) the relationship between soil moisture deficit and topographic index. Chapter 8 undertakes a land cover classification using Decision Tree analysis from NDVI

values. A one-way ANOVA is applied to explore the relationship between topographic index and land cover classes. Chapter 9 presents conclusions and recommendations.

Chapter 2

Literature Review

2.1. Topographic Index

Topographic index, ln(a/tanβ), the natural logarithm of the ratio of the specific flow contributing area (a) to the ground surface slope (tanβ), was first proposed by Kirkby (1975). a is defined as the total flow contributing area (A) through a unit contour length (C) at any given point (Pan *et al.*, 2004), which is illustrated in Figure 2-1. For a grid based DEM, A can be generalized as the number of cells that drain into a specific cell multiplied by the area of a grid cell. A represents not only the flow direction of water, but the accumulated area draining through a point. ln(a/tanβ) is used to as an indicator of the spatial distribution of the soil saturation (Quinn *et al.*, 1995). It is an estimate of the accumulated water flow at any point in a watershed. Higher ln(a/tanβ) values indicate higher potential for saturation, while a lower ln(a/tanβ) indicates the ground area is less likely to be saturated. Areas of saturation are the source areas for overland flow given precipitation input. ln(a/tanβ) can be calculated from DEMs using various algorithms,

which differ mainly in the way A computed. An appropriate estimate of A is critical for the correct calculation of $\ln(a/\tan\beta)$.

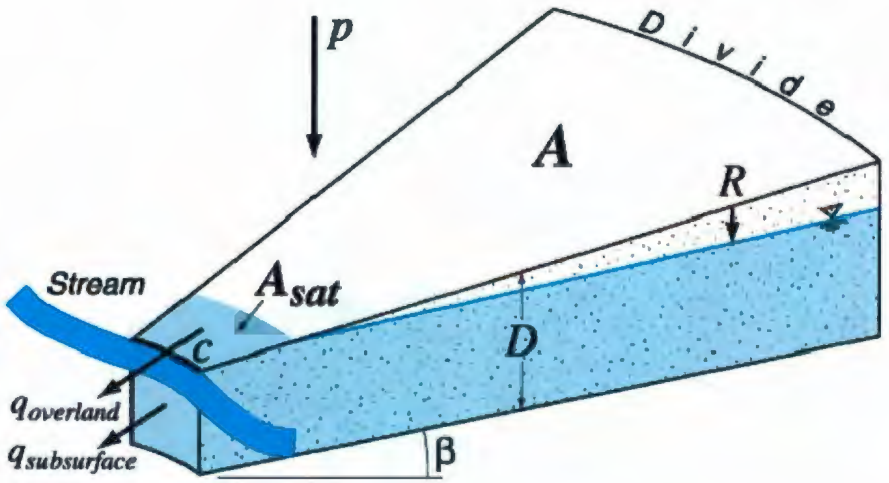

Figure 2-1: The water balance for a catchment hillslope segment. A is total flow contributing area, and C is a unit contour length at any given point (Hornberger *et al.*, 1998).

2.1.1. Different Flow Routing Algorithms to Determine ln(*a*/tanβ)

Many different flow routing algorithms have been implemented to calculate $\ln(a/\tan\beta)$. Four of the most commonly adopted algorithms are: i) the single flow direction algorithm, D8 (O'Callaghan and Mark, 1984); ii) the multiple flow direction algorithm, FD8 (Quinn *et al.*, 1991); iii) the Digital Elevation Model Network algorithm, DEMON (Costa-Cabral and Burgès, 1994); iv) and the biflow direction algorithm, D∞ (Tarboton, 1997).

In D8, all the flow from one cell is routed into the steepest of its eight neighboring cells based on the slope gradient. There is no possibility for flow to be distributed into two cells. Using D8, a tiny elevation difference between two of downslope cells will cause a great effect, as only one of the cells receives all the area. In FD8, each pixel discharges

into all neighboring downslope cells weighted according to slope (Quinn *et al.*, 1991), which means that the cell of interest will receive only a fraction of the discharge from each upslope cell (Costa-Cabral and Burges, 1994). Therefore, the upslope contributing area is dispersed to a large degree even for convergent hillslopes. The DEMON approach determines the flow direction based on the local aspect angle. This algorithm assumes that flow moves across a planar surface in the direction of steepest slope, or aspect angle, similar to a "rolling ball", which would travel down the steepest grade (Costa-Cabral and Burges, 1994). The algorithm D∞ allows only single flow direction but allows water to flow into one or two downslope cells relying on the direction of the steepest descent. This algorithm is still limited to a single flow direction, which becomes increasingly important on convex slopes (Seibert *et al.*, 2007).

The above mentioned algorithms provide a series of rules for directing flow across the land surface where the latter is represented as a square-grid DEM. Many studies have compared and contrasted the performance of these algorithms using a variety of criteria. However, they generally stop short of describing their coincidence with observed runoff behavior and their impact on runoff prediction (Peters *et al.*, 1995).

Wolock and McCabe (1995) compared the $\ln(a/\tan\beta)$ distributions computed by D8 and FD8. They concluded that FD8 produced smoother patterns of $\ln(a/\tan\beta)$ across the DEMs. The mean $\ln(a/\tan\beta)$ values generated with FD8 were also greater than those generated with D8, and the magnitude of this difference tended to increase as the DEM resolution decreased. They also examined how the $\ln(a/\tan\beta)$ distributions calculated with D8 and FD8 affected the hydrologic characteristics simulated by TOPMODEL. The results showed that the differences in model efficiency and simulated paths were

negligible when the model was calibrated by adjusting the subsurface hydraulic parameters.

Tarboton (1997) compared the performance of D∞ with that of D8, FD8, and DEMON. He argued that the D∞ predictions were superior because D8 resolved flow directions too coarsely and introduced grid error, whereas FD8 introduced substantial dispersion resulting in inefficient data storage. Tarboton (1997) did not apply the results to any hydrologic model to further demonstrate the model performance with different $\ln(a/\tan\beta)$ distributions produced by different algorithms.

An appropriate selection of flow routing algorithm is critical for the calculation of $\ln(a/\tan\beta)$, because different algorithms will result in different A and a. In this study D8 and D∞ are applied to determine $\ln(a/\tan\beta)$ in the Marmot Creek basin. The comparison of these two algorithms is to clarify how much variation is warranted, and whether the $\ln(a/\tan\beta)$ distributions will vary with the DEM resolutions that are used.

2.1.2. The Effects of DEM Resolutions on $\ln(a/\tan\beta)$

The resolution of DEMs significantly affects both the representation of the land surface and hydrologic simulation. The resolution of DEMs has direct effects on the calculation of accumulated contributing areas and slope. Different grid sizes will also cause different $\ln(a/\tan\beta)$ distributions that are closely related to the runoff simulation in TOPMODEL.

Zhang and Montgomery (1994) applied high resolution DEMs from two small catchments in the western United States to examine the effects of DEM resolutions on the hydrologic simulation. They calculated $\ln(a/\tan\beta)$ for 2- ,4-, 10-, 30-, and 90-meter scales DEMs, and concluded that DEM resolutions significantly affected topographic

parameters and hydrographs. They pointed out that DEM grid size influenced physically based models of runoff generation and surface processes. Zhang and Montgomery (1994) suggested that for many landscapes, a 10-meter resolution DEM provided a compromise improvement over the other resolution DEMs for simulating geomorphic and hydrological processes.

Wolock and Price (1994) used TOPMODEL to investigate the effects of DEM resolutions (30- and 90-meter) on watershed model predictions for 71 areas in Pennsylvania, New York, and New Jersey. They found that the model predictions of the depth to the water table, the ratio of overland flow to total flow, peak flow, and variance and skew of predicted streamflow were affected by the DEM resolutions. They indicated that these effects were due to the sensitivity of the predictions to the mean of $\ln(a/\tan\beta)$ distributions, which were influenced by the DEM resolutions.

This section reviews the influence of different DEM resolutions on the distributions of $\ln(a/\tan\beta)$, which would further affect the hydrologic simulations. It can be ascertained that topographic parameters and hydrographs will be definitely impacted by different DEM resolutions. In this study 1- and 90-meter resolution DEMs will be used to quantify the variability of the performance of these two resolutions on the hydrologic simulations across the Marmot Creek basin.

2.1.3. The Relationships between Terrain Indices and Soil Moisture

The relationship between soil moisture and terrain indices has been studied in a variety of landscapes and summarized by Western *et al.* (1999, 2002). It is rare for terrain indices to explain more than half the spatial variability in soil moisture, often significantly less.

Andrew *et al.* (1999) found that at the small catchment and hillslope scales, soil moisture varied as a result of water routing processes, radiative effects (aspect, slope, etc.), heterogeneity in vegetation, and soil characteristics besides $\ln(a/\tan\beta)$. $\ln(a/\tan\beta)$ represented the main factor controlling the spatial distribution of soil moisture. Andrew *et al.* (1999) indicated that $\ln(a/\tan\beta)$ had performed well in some circumstances but poorly in many others. Whether this was due to the processes leading to topographic organization being incorrectly represented or whether it was due to limited topographic organization was uncertain.

Limitations of terrain indices to explain the variability of soil moisture are partly due to the assumptions in their derivation. No static index can be expected to continuously successfully represent all the details of dynamic processes. Terrain indices assume that terrain is the dominant control on the spatial soil moisture pattern, but the importance of soils, precipitation and vegetation in controlling soil moisture content has also been recognized (Wilson *et al.*, 2004). The spatial distribution of soil moisture may be significantly affected by these factors.

Even through $\ln(a/\tan\beta)$ has been shown to provide limited representation of soil moisture, it remains as an important parameter from which to study hydrologic similarity. In this thesis, the soil moisture deficit, estimated by TOPMODEL, is derived on the basis of $\ln(a/\tan\beta)$. The relation between soil moisture deficit and $\ln(a/\tan\beta)$ will be studied.

2.2. Methods of Potential Evapotranspiration Estimation

Potential evapotranspiration (PET) expresses as the amount of water that can evaporate and transpire from a vegetated landscape without restrictions other than the atmospheric

demand. This concept was introduced as part of a scheme for climate classification by Thornthwaite (1948). The concept of PET provides a convenient index to represent and estimate the maximum water loss to the atmosphere.

PET can be measured directly by lysimeters or eddy correlation method from well watered areas. But these measurements are implemented only in research over small plots for a short time periods, as they are expensive. Usually, PET is estimated by theoretical or empirical equations, or derived simply by multiplying standard pan evaporation data by a coefficient (Grismer *et al.*, 2002). There are approximately 50 methods available to estimate PET, but these methods give inconsistent values due to their different assumptions and input data requirements, or because they are often developed for specific climatic regions (Grismer *et al.*, 2002). These methods can be classified on the basis of their data requirements (Dingman, 2002): i) Temperature-based methods, which use only air temperature and sometimes day length; ii) Radiation-based methods, which use net radiation and air temperature; iii) Pan-based methods, which use pan evaporation, sometimes with modifications depending on wind speed, temperature, and humidity; iv) Combination methods, which use net radiation, air temperature, wind speed, and relative humidity.

In 1948, Penman combined the energy balance and the bulk aerodynamic method to calculate evapotranspiration. This has become known as the combination method. The combination method includes an energy term and an empirical wind function term based on meteorological measurements at one level above the surface. Penman's method was improved by Monteith (1965), who introduced a surface resistance parameter

representing plant physiological and a more general aerodynamic resistance term for the entire vegetation. This equation is now known as the Penman-Monteith equation.

Biftu *et al.* (2000) found that the Penman-Monteith approach predicted PET very well for dry, dense canopy situations, but underestimated PET in mixed and wet forest situations. Drexler *et al.* (2004) suggested that reliable results might be obtained only with detailed spatially distributed information on surface cover variability and land surface resistance for wetland applications.

However, the Penman-Monteith approach for computing PET still has had numerous successful applications in the field of hydrology (e.g. Biftu *et al.*, 2000; Kite *et al.*, 2000; Bigelow, 2001; Liu *et al.*, 2003). This method of estimating PET has been proved to be superior to a further 20 methods according to the results of a regression analysis of lysimeter measurement (Jensen *et al.*, 1989).

This thesis will use PET, calculated from the Penman-Monteith method, to serve as input to the TOPMODEL hydrologic model.

2.2.1. The Effects of Stomatal Resistance and Aerodynamic Resistance on Evapotranspiration

Stomata are pores on the surfaces of leaves. They open in sunshine, allowing the diffusion of carbon dioxide into the leaves. When they are open, water vapor can diffuse from the wet cell walls to the outside air (Szeicz, 1969). Transpiration thus represents an unavoidable loss of water from the leaves (Szeicz, 1969). When soil moisture is limiting or the rate of transpiration is fast, leaf stomata may close to retard transpiration (Szeicz,

1969). Stomatal resistance (r_c) can be defined as the molecular diffusion resistance to the flux of water vapor from the wet cell walls to just outside the leaves (Szeicz, 1969).

The vertical transfer of fluxes of a water vapor or heat is influenced by the turbulence, which is generated by surface roughness elements. The resistance encountered by fluxes of water vapor or heat or momentum along the path of transfer is known as the aerodynamic resistance (r_a). This resistance is from the source to a given reference air level above.

Water loss from plant leaves is controlled by r_c and r_a operating in series (Meinzer *et al.*, 1997). The extent to which stomatal movements control evapotranspiration is largely a function of the ratio of r_c to the resistance of the boundary layers surrounding the leaves. Stomatal control evapotranspiration is strong only when r_a is low in relation to r_c. Many models of evapotranspiration depend not only on meteorological parameters but also on surface parameters such as the stomatal and aerodynamic resistances to the diffusion of water vapour from the vegetation. A limitation on the use of these models is a difficulty in measuring or estimating these resistance terms. The Penman-Monteith approach, used in this study to estimate PET, contains both stomatal and aerodynamic resistance. One objective of this study is to determine which resistance is the dominant controller for PET compared with the other resistance over the Marmot Creek basin.

2.3. TOPMODEL

2.3.1. The Development of the TOPMODEL

In any catchment the hydrologic modeling is faced with a wide variety of geology, soils, vegetation, land use, and topographic characteristics that will affect the relationship

between rainfall and runoff. Models taking all these characteristics into account are difficult to apply, because the input data is not directly measurable and if available would require large computational resources. However, there may be many points within the watershed that act in a hydrological similar way with a similar water balance and similar runoff generation mechanism. If it was possible to classify points in the catchment in terms of their hydrological similarity, then a simpler form of model could be used. In this study, TOPMODEL is employed to define the hydrological similarity through topography and soils information. The simplicity of TOPMODEL comes from its use of $\ln(a/\tan\beta)$, which is developed into a full catchment rainfall-runoff model. The basic assumption of TOPMODEL is that all points in a catchment with the same value of $\ln(a/\tan\beta)$ will respond in a hydrological similar way. It then becomes no necessary to complete calculations for all points in the catchment, but only for representative points with different values of the index. While many runoff models succeed in predicting flow without the benefit of topographic information, the TOPMODEL is attractive because it can provide a physically realistic, but parametrically simple rainfall runoff model, with the ability to predict different types of hydrological response (Seibert *et al.*, 1997).

2.3.2. The Applications of the TOPMODEL

TOPMODEL is originally developed to simulate upland watersheds for humid temperate areas. As it is adaptable for hillslope watersheds with few parameter inputs for runoff prediction, TOPMODEL has been applied in a variety of counties such as Australia, Canada, Finland, France, Italy, New Zealand, Spain, Switzerland, the United Kingdom, and the United States. Due to the simplicity of implementation, TOPMODEL is widely used to study a range of topics, including flood frequency derivation (Beven, 1987),

model parameter calibration (Homberger *et al.*, 1985), topographic effects on streamflow (Beven and Wood, 1983), climate change effects on hydrologic processes (Wolock and Homberger, 1991), the prediction of spatially distributed groundwater levels (Seibert *et al.*, 1997), and the effects of DEM resolution on model prediction (Quinn *et al.*, 1995).

Güntner *et al.* (1999) tested TOPMODEL's capability for adequately representing dominant hydrological processes in the humid and mountainous Brugga catchment (40 km^2) in south-west Germany. The authors explained that although runoff simulations were satisfactory, inadequacies of the model structure compared with the real situation in the study area were found. These differences were mainly caused by the concept of variable contributing areas for saturation excess overland flow and their dynamics which were overestimated by the model.

Iorgulescu and Jordan (1994) applied TOPMODEL in two subcatchments of the Haute-Mentue (Switzerland) research basin. Parameters were calibrated with the Nash-Sutcliffe efficiency (EFF) criteria. Even if an acceptable numerical fit was reached (EFF=0.84) and although it was possible to verify some of the underlying concepts of TOPMODEL for that basin, it was still thought that the model could not be validated fully with respect to field measurements and knowledge of the physical processes involved in that catchment response.

Holko and Lepistö (1996) used TOPMODEL to simulate the hydrological behavior of a mountain catchment at Jalovecky Creck, Western Tatras, Slovakia. The results showed that more effort would be required to improve the simulation, even through the total simulated runoff for the whole period was close to the measured runoff.

It is worth stressing at this point that TOPMODEL is not a hydrological modeling package, but rather a set of concepts that can be used to simulate distributed catchment responses with simple physical theory and a small number of parameter values. TOPMODEL will be employed in this study to simulate the streamflow and soil moisture deficit in the Marmot Creek basin.

2.4. Effect of Topography on Vegetation Cover

Topography affects the amount of land cover through its effect on moisture availability via runoff. Pickup and Chewings (1996) studied the correlations between DEM-derived topographic indices and remotely-sensed vegetation cover in a mountain and piedmont area of arid central Australia. The regression approach showed that patterns of vegetation cover were related to topography but the most important predictors were biological processes such as the percentage of bare area upslope of a point.

Dargie (1984, 1987) investigated the relationship between topography and vegetation biomass in a semi-arid, mid-latitude, mountainous area in Spain and concluded that soil moisture was the dominant predictor for biomass. Kirkby *et al.* (1990) also studied the factors related to the vegetation biomass in a semi-arid, mountainous area in Spain, and found that soil moisture, as well as aspect, were the dominant controller. In contrast, Velázquez-Rosas *et al.* (2002) performed a correlation analysis between elevation and plant morphometry for La Chinantla, a hyper-humid, mountainous region of southern Mexico. They presented that leaf area had a significant, negative correlation with elevation, possibly due to wind exposure, soil fertility, and/or the negative temperature gradient as elevation increases. From these studies, Nemani *et al.* (2003) deduced that

topography exerted a dominant control on vegetation greenness along with other climatic factors such as temperature, radiation, and water availability.

The objective of this research is to ascertain the correlation, if any, between the land cover classes with $\ln(a/\tan\beta)$ in the Marmot Creek basin. That is, this study wants to determine if each class of land cover that can be described by what is known of $\ln(a/\tan\beta)$ of the target basin. Then these two factors can be integrated into a model to describe hydrologic similarity.

2.5. Summary

This chapter has given a background on the methodologies used in this thesis, such as $\ln(a/\tan\beta)$ calculation, PET estimation, and TOPMODEL simulation. The effects of flow routing algorithms on $\ln(a/\tan\beta)$ calculation, and the effects of r_c and r_a on PET are reviewed. The relationships between terrain indices and soil moisture, and the relationship between topography and land cover classes are also introduced. A detailed explanation of this research on these components will be given from chapter 4 to chapter 8.

Chapter 3

Study Area and Data Preparation

3.1. Study Area Description

The Marmot Creek basin was selected in 2006 as a site to study the hydrology of Canada's cold regions by the IP3 research network. IP3 is comprised of several dozen investigators and collaborators across Canada, the US, and Europe. IP3 is devoted to an improved understanding of surface water and weather systems in cold regions, particularly in Canada's Rocky Mountains and Western Arctic. These issues are important to agriculture, regional planning, policy making, streamflow forecasting, water management, environmental conversion, and urban and industrial development.

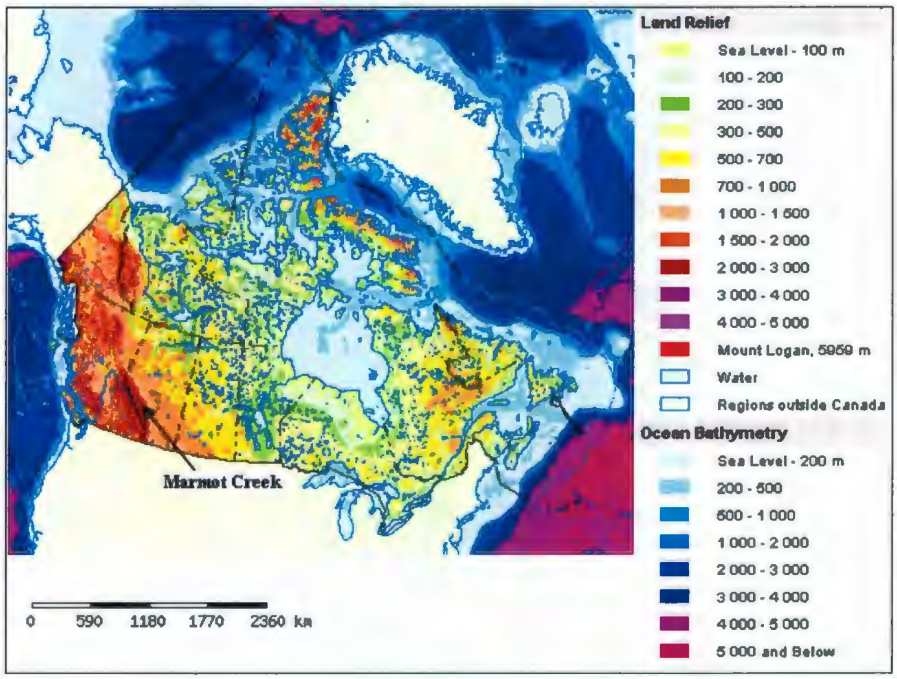

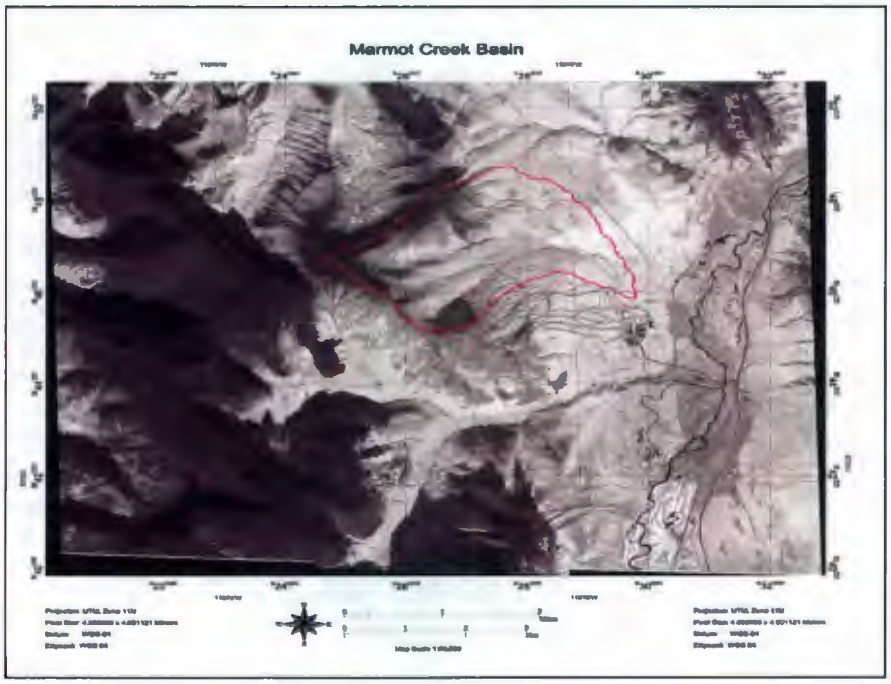

Figure 3-1: Location of the Marmot Creek basin.

The Marmot Creek system is a small mountain drainage which is located at latitude 50°57'N and longitude 115°10'W on the east flank of Mount Allan in the Kananaskis River valley (Figure 3-1). The basin is about 110 km southwest of Calgary, Alberta. The drainage waters of the Marmot Creek basin result from precipitation in the lee of the Rocky Mountains.

The total area of the Marmot Creek basin is approximately 9.5 km^2. Elevations in the basin range from 1,585 to 2,805 m with a mean elevation of approximately 2,112 m. This basin is divided into three sub-basins: Twin Fork, Middle Fork, and Cabin Creek. Twin Creek and Middle Fork Creek conjoin just below the 1,768 level, and Cabin Creek joins the Marmot Creek basin at the 1,707 m elevation. These three sub-streams come together to form a single larger stream which drains into the Kananaskis River.

In the Marmot Creek basin, the forest covers nearly 60% of the basin area from the basin outlet to the tree line. The remaining 40% of the area lies above the tree line, which consists of 80% alpine meadow and rock, and 20% Krummholz (Stevenson, 1967). Krummholz is a feature of subarctic and subalpine tree line landscapes, where continual exposure to fierce, freezing winds causing vegetation to become stunted and deformed (Wikipedia, 2008). The forest vegetation is dominated by spruce-subalpine fir. The non-forest plants are small trees, shrubs, grass, herbs, and mosses.

The sequence of soil development in the Marmot Creek basin appears to be controlled by elevation, parent material, slope, and moisture conditions. The main types of soil in the basin are Brunisolic Grey Wooded soils, podzolic soils, regosolic soils, alpine black soils, and local gleysolic and organic soils (Stevenson, 1967). The Brunisolic Grey Wooded soils are found in lower part of the Marmot Greek basin, podzolic soils are found in the

mid-slope areas, brunisolic soils are at higher elevations than podzolic soils, and alpine black soils can be found in the alpine zone (Stevenson, 1967). The soils are porous in the Marmot Creek basin and, when not frozen, allow most of the precipitation to enter the soil.

The climate is characterized by short, cool summers and long, cold winters. The mean annual precipitation in the Marmot Creek basin is approximately 1,080 mm, about three-quarters of which falls as snow (Singh and Kalra, 1972). Rain occurs during the period from June to September. Precipitation in the Marmot Creek basin is frozen for more than six months of the year. The soil layer begins to freeze in October or November (Telang *et al.*, 1982). The average July temperature ranges from 18 to 2 °C, and the average January temperature ranges from -6 to -18 °C.

In the Marmot Creek basin, the groundwater table generally follows the relief of the ground surface (Osborn and Jackson, 1974). The table is lowest where it intersects the surface in the valley bottoms (Stevenson, 1967). Much of the stream flow in the Marmot Creek basin is derived from groundwater (Telang *et al.*, 1982). This is particularly true during the late fall and winter when the precipitation reaching the stream through overland flow is minimal. The groundwater reservoirs are recharged in the spring when part of the snow melts and rainfall percolates through the soil to the water table (Telang *et al.*, 1982). Spring snowmelt begins at a low elevation and gradually moves upslope, into heavier snowpack areas. Snowmelt typically starts in late April to early May and peaks in early June, continuing into midsummer. In midsummer, nearly 70% of the stream flow results from the melting of snow in protected alpine areas (Telang *et al.*, 1982).

3.2. Topographic Data

The most common digital data of the Earth's surface is the cell-based digital elevation model (DEM) because of its ease of computer implementation and computational efficiency (Beven, 2001). DEMs with a fixed grid size are known as raster data. These data represent a continuous surface of the ground by a large number of selected points with known *xyz* coordinates.

DEMs, adopted in this study, are based on both Shuttle Radar Topography Mission (SRTM) data and Light Detection and Ranging (LiDAR) topographic data for the Marmot Creek basin. SRTM has obtained elevation data on a near-global scale to generate the most complete high-resolution digital topographic database of Earth. SRTM elevation data can be downloaded from U.S. Geological Survey (USGS), which has 90-meter resolution. A Leica SR530 dual frequency survey grade GPS receiver is set up over a survey monument at the Kananaskis Research Station by the IP3 research network to get LiDAR data, which has 1-meter resolution. Survey flight lines are flown over the Marmot Creek basin polygons using the lidar survey specification. The airborne data collection and calibration take over 70 hours and are performed out of the Calgary airports. The DEMs with 1- and 90-meter resolutions are showed in Figure 3-2.

In this study, DEMs are applied through the RiverTools software to determine the slope, accumulated area, flow direction, main stream length, watershed area, and $\ln(a/\tan\beta)$ of the Marmot Creek basin.

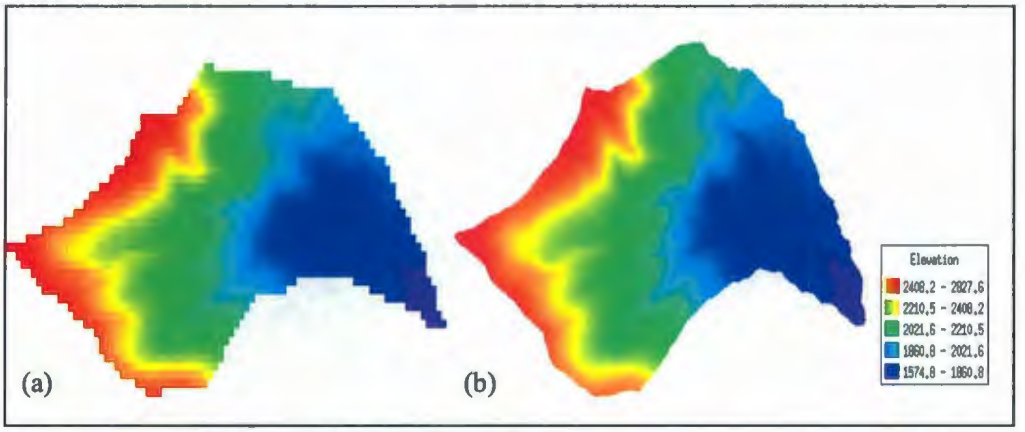

Figure 3-2: DEMs for the Marmot Creek basin: (a) 90-meter resolution, (b) 1-meter resolution.

3.3. Meteorological Data Collection

The Canadian Land Surface Scheme (CLASS), a land-surface parameterization scheme for use in large-scale climate models, is employed in this study to do evaporation resistances simulation. CLASS requires half hourly values of seven meteorological variables to run the model. These variables are incoming short wave radiation (K↓) or net short wave radiation (K*), incoming long wave radiation (L↓) or net long wave radiation (L*), air temperature (T), wind speed (v_a), specific humidity (q), atmospheric pressure (p), and precipitation rate (P). TOPMODEL, on the other hand, requires only daily rainfall, and PET, which can be calculated by the Penman-Monteith function. All of the required data are measured at, or close to, the Marmot Creek basin. The meteorological data, used to run CLASS, come from two stations listed in Table 3-1. P and p are measured in the Hay Meadow station. T, q, K↓ and L↓, and v_a come from the Vista View station. These meteorological data have been recorded every fifteen minutes since 2006. Hay Meadow station (50°56'N, 115°08'W), locating at 1,436.8 m level, is not within the Marmot

Creek basin boundary, but very close to it. Vista View station is near to the Cabin Creek, which is presented as star in the map. The Meteorological instrumentation sites pertinent to this study are shown in Figure 3-3.

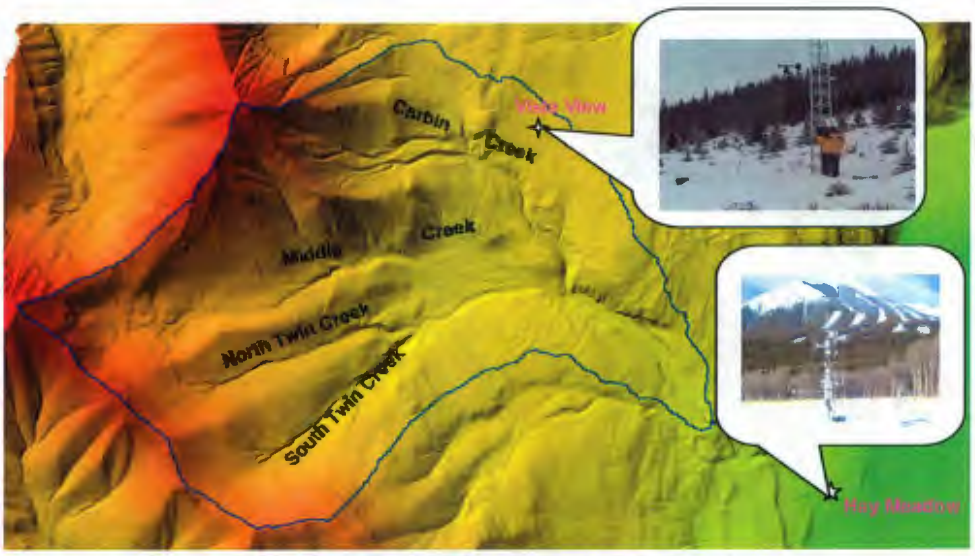

Figure 3-3: Station site photos and site locations.

L↓ and K↓ respectively, are measured with Kipp & Zonen 4 component net radiometer (model CNR1, manufactured by Kipp & Zonen for applications requiring research-grade performance). Radiation instruments are mounted at a height of 1.27 m at the Vista View station. At the Hay Meadow station, Air Eye optical total precipitation sensor gives the information about precipitation and visibility in the meteorological terms.

Figure 3-4 shows mean diurnal trends of K↓, T, P and vapor pressure deficit (Δe) in 2006 and 2007 (July 12th to October 30th in 2006, and April 30th to October 30th in 2007). In 2006 and 2007, daily mean air temperatures showed a partial correlation with the radiative forcing. In 2006, cloudy with showery or rainy conditions prevailed for much of the time. In 2007, except major storms on June 7th and September 12th, total daily precipitation was generally modest. From June 20th to August 10th, the 50-day period was

generally dry, and only on 7 days did precipitation fall. The total precipitation over the study period reached 982.10 mm, in 2006, and 2734.88 mm in 2007, and the maximum daily precipitation was observed in June 6th, 2007 (0.358 m day^{-2}). Calculated values of $\overline{\Delta e}$ showed little variation and rarely exceeded 1.6 kPa. The maximum daily value of K↓ and T, which were 36.87 W m^{-2} and 22.11 °C respectively, were observed in the summer months, between June and August.

Table 3-1: Summary of instrumentation and measurement locations for each Meteorological data.

Parameter	Site	Height(m)	Instrument
Incoming long wave radiation (L↓)	Vista View station	1.27	CNR1(4-component radiation sensor)
	Hay Meadow station	1.66	CNR1(4-component radiation sensor)
Incoming short wave radiation (K↓)	Vista View station	1.27	CNR1(4-component radiation sensor)
	Hay Meadow station	1.66	CNR1(4-component radiation sensor)
Net radiation (K+L)	Hay Meadow station	1.66	CNR1(4-component radiation sensor)
Air temperature (T) /humidity (q)	Vista View station	2.62	HMP35A sensor
	Hay Meadow station	1.86	HMP45C212 sensor
Wind speed (v_a)	Vista View station	2.3	Metone 50.5 2-D sonic anemometer
	Hay Meadow station	3.0	RMYoung Propellor anemometer
Soil moisture	Hay Meadow station	0.25B.G.S	CS616 soil; moisture capacitance probe
Pressure (p)	Hay Meadow station	1.25	BP61025V barometric pressure sensor
Precipitation (P)	Hay Meadow station	3.00	Air Eye optical total precipitation sensor

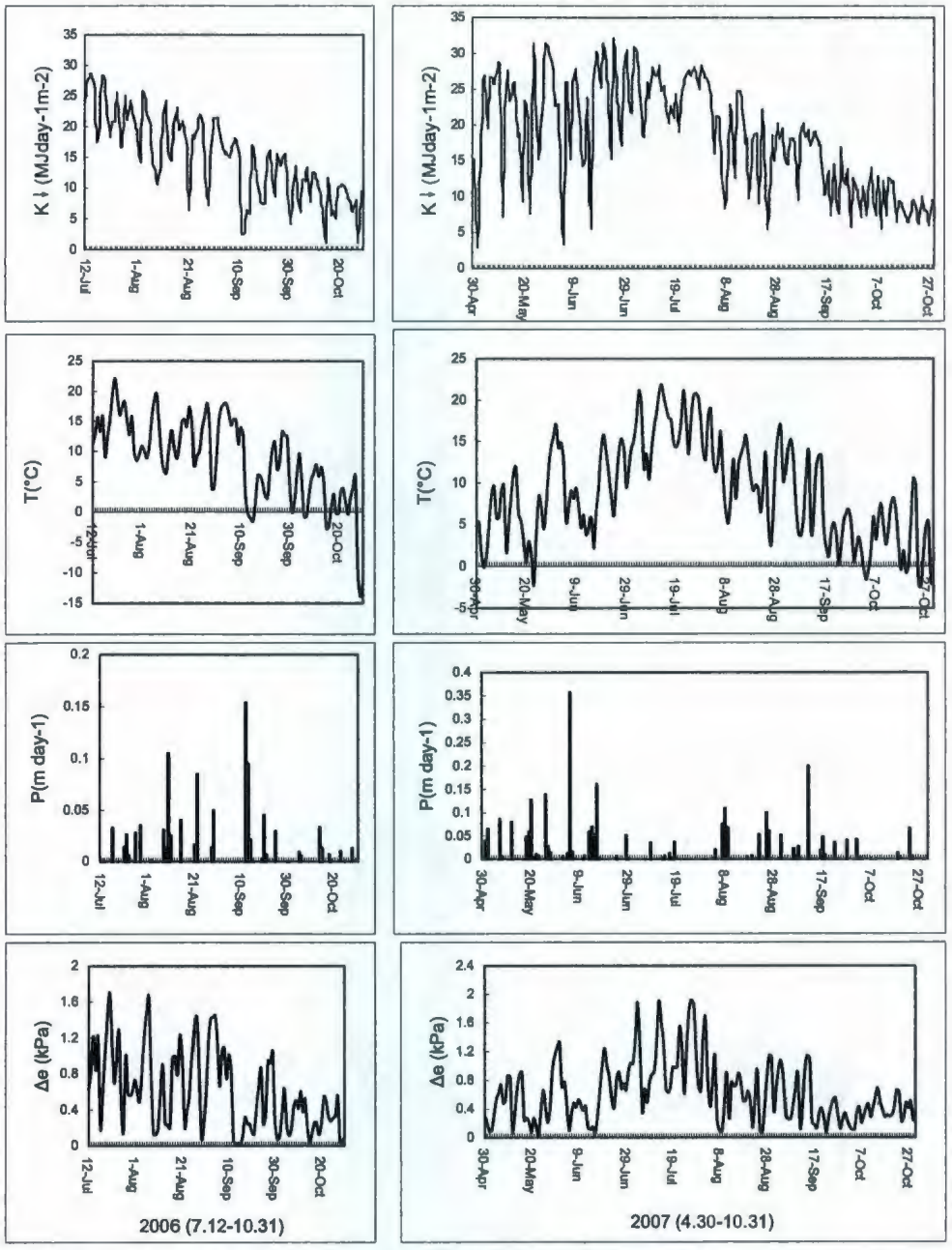

Figure 3-4: General meteorological conditions during the field measurement programs. Variables shown are: daily mean incoming short wave radiation (K↓); mean air temperature (T); daily total precipitation (P); and daily mean vapor pressure deficit (Δe).

Figure 3-5 shows the measured streamflow (Q) in 2006 and 2007. Streamflow is measured in the Marmot Creek Main Stem near Seebe (50°57'1"N, 115°09'10"W) gauging station. The maximum streamflow in 2006 was 0.0000751 m h^{-1} which was occurs on October 1st. The maximum streamflow in 2007 was nearly 0.000431 m h^{-1} greater than that in 2006, which was on June 6th. Good responses between precipitation and runoff could be observed from July to October 2006 and from April to August 2007. However this seems not true after August 2007. The inconsistent rainfall and runoff response is likely due to data error, particularly with the interpolation of rainfall data. Other possible reasons include differences in antecedent moisture, storm location relative to the drainage network, temporal and geographic distribution of the rainfall, changes in basin routing parameters between events, and the possibility of rain on snow inputs for some events. The peaks at July 12th 2006 might be caused by snowmelt from the alpine region in the Marmot Creek basin.

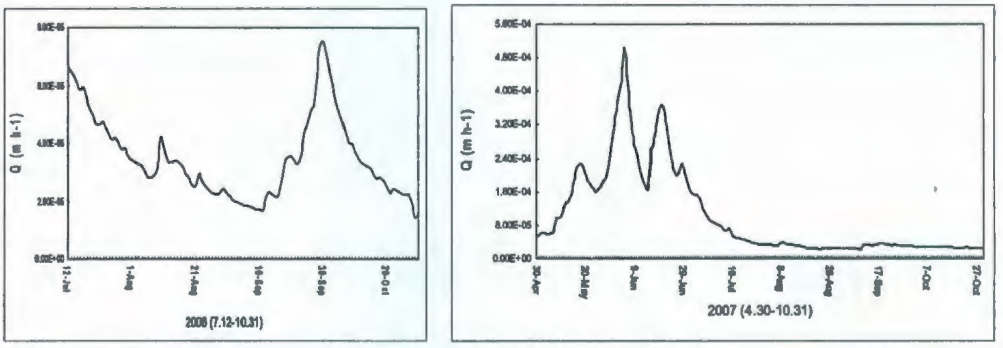

Figure 3-5: Streamflow measurements in 2006 and 2007 in the Marmot Creek basin.

3.4. Summary

This chapter briefly describes the characteristics of the Marmot Creek basin including forest cover, soil condition, average annual meteorological situation, and streamflow

mechanisms. Understanding these attributes is very helpful to analysis the simulation results. Topographic and meteorological data preparations are detailed described in this chapter. All these data will be used to do simulations in the following chapters.

Chapter 4

Topographic Index Calculation

$\ln(a/\tan\beta)$ is an estimate of the accumulated water flow at any point in a watershed. It is calculated for each cell in a DEM. To do this, the slope and flow direction must first be determined. In this chapter, two common types of flow routing algorithms, single flow and biflow direction algorithms, are used to calculate $\ln(a/\tan\beta)$ in the Marmot Creek basin with 1- and 90-meter resolution DEMs. The aim of this chapter is to examine which algorithm is more appropriate.

4.1. Flow Routing Algorithms

Different flow routing algorithms will, of course, result in different slope and contributing area. Guth (1995) found that the choice of algorithm could influence average slope calculations as much as 25%. Such a variation emphasizes that the care should be taken in selecting an algorithm which will produce an accurate representation of the terrain.

4.1.1. Single Flow Direction Algorithm

Single flow direction algorithm was first introduced by O'Callaghan and Mark (1984), and has been widely used in DEM data analysis and GIS softwares. This algorithm, designated as D8 (eight flow directions), is the earliest and simplest method to route flow from an individual grid cell to one of its eight neighbors. Water is assigned either adjacent or diagonal in the direction with steepest downward slope.

D8 computes the distance-weighted drop of the center cell along eight directions. The distance-weighted drop is calculated by subtracting the neighbor's elevation value from the center cell's value and dividing by the distance from the center cell. This distance is weighted as $\sqrt{2}$ for a corner cell and 1 for a non-corner cell. The flow direction is assigned to the greatest distance-weighted drop, shown in Figure 4-1.

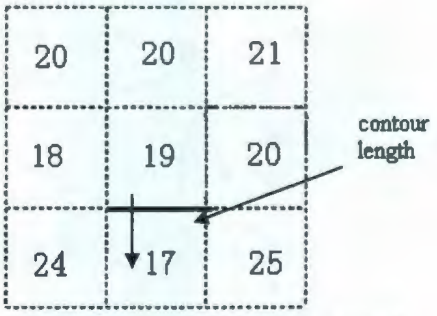

Figure 4-1: Downslope direction for D8.

In some situation, when the central cell is surrounded by higher elevation values, the distance-weighted drop is negative. If the greatest calculated slope was less than zero, this central cell is called a sink or a pit, which only has inflow and no outflow. Some sinks are data errors introduced in the surface generation process, while others represent real topographic features (Jenson, 1988). As it is always computationally required to force watersheds to have outlet, sinks in DEM data are usually filled before analysis. One

common filling method, which was introduced by Jenson and Domingue (1988), is to raise the elevation of a sink to the lowest elevation among its neighbors. Thus the slope value of the "filled" cell is now zero. The central cell and its neighbors form a flat area.

Once the flow directions are assigned to all cells, the next procedure is to determine the total contributing area, A.

$$A = (n+1) \times DX^2 \qquad \text{Equation 4-1}$$

where n is the number of upslope cells, DX is the grid cell length. The magnitude of local slope, tanβ, is calculated as:

$$\tan\beta = \frac{\Delta H}{\Delta L} \qquad \text{Equation 4-2}$$

where ΔH is the change in elevation between neighboring grid cells, and ΔL is the horizontal distance between centers of neighboring grid cells. Here, the change in elevation will be reset to 0.5× (vertical resolution of elevation data) for flat areas, and the vertical resolution elevation is always equal to 1 m. ln(a/ tanβ) can be calculated as:

$$\ln(a/\tan\beta) = \ln[\frac{A}{C \times \tan\beta}] \qquad \text{Equation 4-3}$$

The contour length, C, is assumed equal to grid cell length in D8.

D8 works well to simulate the flow of rivers, streams, and flow convergence in valleys (Tarboton, 1997). However, this algorithm oversimplifies the possible flow direction from a grid center by limiting flow to only one grid cell. As a result, it is unable to simulate divergent flows (Holmgren, 1994). These limitations are most often expressed in

the parallel flow paths in either the cardinal or diagonal directions that are produced with this algorithm.

4.1.2. Biflow Direction Algorithm

Biflow direction algorithm, designated as D∞, is based on the methods reported by Tarboton (1997). This algorithm routes flow in the direction of the steepest downwards slope of the eight triangular facets formed in a 3 by 3 grid cells window. Flow is then proportioned into two edges forming that steepest triangle based on the resulting downslope vector. The slope direction and magnitude of eight facets should be calculated. Figure 4-2 illustrates the procedures to determine the steepest downslope vector in the first facet only. In this method, slope is represented by the vector (s_1, s_2) where

$$s_1 = \frac{e_0 - e_1}{d_1} \qquad \text{Equation 4-4}$$

$$s_2 = \frac{e_1 - e_2}{d_2} \qquad \text{Equation 4-5}$$

where e_i and d_i are elevations and distances between cells as showed in Figure 4-3. The slope direction and magnitude can be presented as:

if r is in the range $(0, \tan^{-1}(d_2/d_1))$, then

$$r = \tan^{-1}\left(\frac{s_2}{s_1}\right) \qquad \text{Equation 4-6}$$

$$s = (s_1^2 + s_2^2)^{1/2} \qquad \text{Equation 4-7}$$

If $r < 0$, then $r = 0$, $s = s_1$. If $r > \tan^{-1}(d_2/d_1)$, then

$$r = \tan^{-1}(\frac{d_2}{d_1})$$ Equation 4-8

$$s = \frac{e_0 - e_2}{(d_1^2 - d_2^2)^{1/2}}$$ Equation 4-9

Each facet can be rotated to facet 1 to calculate the slope and angle with e_0 is the center point, e_1 is the point to the side, and e_2 is the diagonal point. The local angle associated with the steepest downward slope is $r' = r$ when s is maximum among the eight facets. This angle should be finally adjusted to reflect an angle counter-clockwise from east to get the flow direction angle (r_g), which can be calculated as:

$$r_g = a_f r' + \frac{a_c \pi}{2}$$ Equation 4-10

where a_f and a_c rely on the facet selected (Table 4-1). To determine the flow direction in a flat area or sink, D∞ uses the same method as D8, which is suggested by Jenson and Domingue (1988).

The contributing area is calculated using a recursive procedure, which can be presented as:

$$A = DX^2 + \sum_i^n (P_i \times A_i)$$ Equation 4-11

where P is the proportion of neighbor that drains to cell based on angle. The contributing area of each cell is taken as its own area plus the area of upslope neighbors that have some fraction draining to the cell. The slope, tan β, is calculated as:

$$\tan \beta = s$$ Equation 4-12

and ln(a/ tan β) can be calculated as:

$$\ln(a/\tan\beta) = \ln(\frac{A}{C\tan\beta}) = \ln(\frac{A}{Cs}) \qquad \text{Equation 4-13}$$

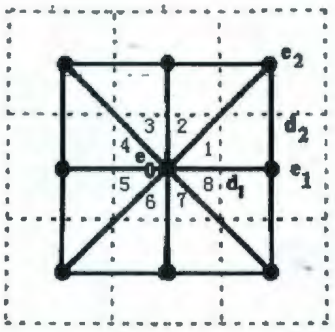

Figure 4-2: Definition of variables for the calculation of slope on facet 1.

Table 4-1: a_f and a_c value to corresponding facets (Tarboton, 1997).

Facet	1	2	3	4	5	6	7	8
a_c	0	1	1	2	2	3	3	5
a_f	1	-1	1	-1	1	-1	1	-1

D∞ describes infinite possible single-direction flow pathways. It allows only a single flow direction but allows area to flow into one or two downslope cells depending on the direction.

4.2. Results and Discussion

This section compares the difference of ln(a/tanβ) spatial distribution produced by D8 and D∞. These comparisons are based on both SRTM elevation data and LiDAR data of the Marmot Creek basin. The ln(a/tanβ) spatial distributions are produced for each DEM by each of these two algorithms. Sinks in the Marmot Creek basin are filled to ensure that the entire drainage area contribute to a field edge. Both algorithms are applied to the same sink-filled DEM. D8 and D∞ are implemented using the RiverTools software.

Figure 4-3 shows color maps of a, tanβ and ln(a/tanβ) computed by D8 and D∞ for the Marmot Creek basin with 90-meter resolution DEM. The values of a measure the amount of the upslope drainage area and local flow convergence or divergence. The values of tanβ measure the local gravitational gradient. The values of ln(a/tanβ) are highest where a is highest and tanβ is lowest (gentle slopes).

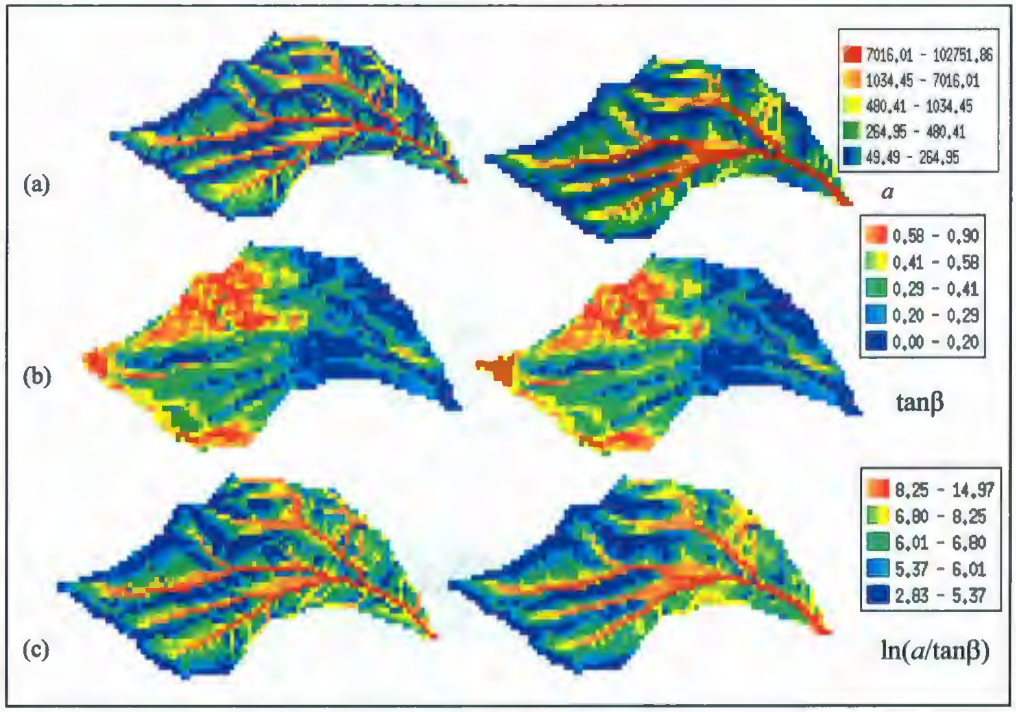

Figure 4-3: (a) values of a, (b) values of tanβ, and (c) values of ln(a/tanβ) computed using D8 (left panels) and D∞ (right panels) algorithms with 90-meter resolution DEM for the Marmot Creek basin.

The spatial distribution of tanβ generated by D8 appears identical to the distribution produced by D∞. The spatial distributions of a and ln(a/tanβ), however, look somewhat different. D8 produces a spatial distribution with a more discrete, rougher pattern, while the distribution produced by D∞ has a smoother pattern. The smoothness, in the pattern

of the spatial distribution generated by D∞, occurs because the upslope area is partitioned into multiple downslope neighboring cells.

The distributions of a, tanβ, and ln(a/tanβ) values can be also described by their mean, variance, and skew values (Table 4-2). Compared to D8, D∞ results in an ln(a/tanβ) distribution with higher mean and variance values, and a lower skewness value. The higher mean ln(a/tanβ) value is associated with a higher mean value of a and tanβ for D∞. Similarly, the lower skewness value of ln(a/tanβ) is associated with lower skewness values of a and tanβ for D∞ compared to D8. The higher mean value of a, resulting from D∞, may occur for the following reasons. D∞ allows for flow convergence (several cells draining into one downslope neighboring cell) and flow divergence (one cell draining into two downslope neighboring cells). D8, in contrast, permits only flow convergence. When flow convergence takes place, A is concentrated in one downslope neighboring cell, thereby increasing a for that particular downslope neighboring cell. When flow divergence occurs from a cell C for that cell is high, and thus it has a low value of a. Therefore, flow convergence increases a values of downslope neighboring cells, whereas flow divergence decreases the local values of a. The algorithm, which includes both convergence and divergence, might be expected to have lower mean values of a compared to one that includes only convergence. These data, however, show that when both convergence and divergence are considered in an algorithm, the upslope contributing area is more dispersed and evenly distributed, and has the net effect of increasing the mean value of a.

Table 4-2: Statistics analysis of a, tanβ, and ln(a/tanβ) distributions computed for the Marmot Creek basin, with 90-meter DEM using D8 and D∞ algorithms.

Algorithm	Variable	Mean	Variance	Skewness
D8	a	2521	112931698	6.71
	tanβ	0.36	0.032	0.45
	ln(a/tanβ)	6.77	3.69	1.45
D∞	a	2706	111750961	6.48
	tanβ	0.37	0.034	0.43
	ln(a/tanβ)	6.95	3.84	1.33

The gray-shaded maps of ln(a/tanβ) provide a visual comparison between algorithms with 1- and 90-meter resolution DEMs (Figure 4-4). The spatial distribution of ln(a/tanβ) generated by D8 looks identical to the distributions produced by D∞ in coarse DEM, but it is obvious that they are different in fine resolution DEM.

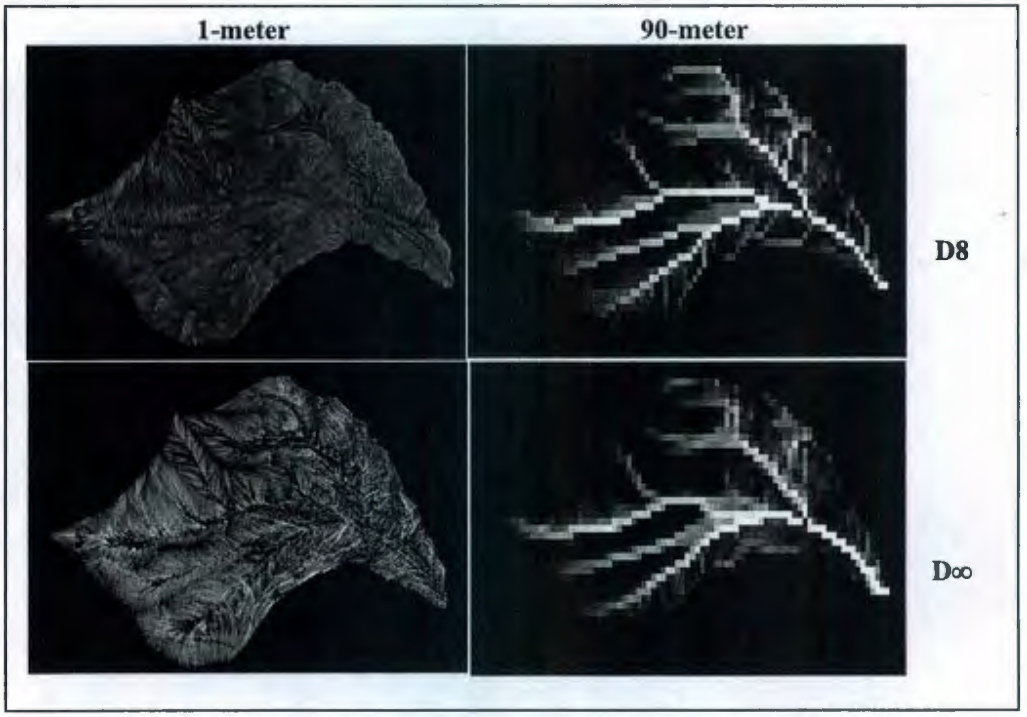

Figure 4-4: The maps of ln(a/tanβ) for 1- and 90-meter resolution DEMs of the Marmot Creek basin calculated by D8 and D∞ algorithms.

From Figure 4-5, one can ascertain that unrealistic drainage patterns (i.e., straight flow paths) resulting from the grid structure are present in all algorithms to some degree, but such phenomenon is more obvious in D8. D8 yields straight and parallel flow paths along hillslopes. These visual comparisons highlight both similarities and differences between algorithms. The spatial distributions of $\ln(a/\tan\beta)$ can also be described by a statistical analysis.

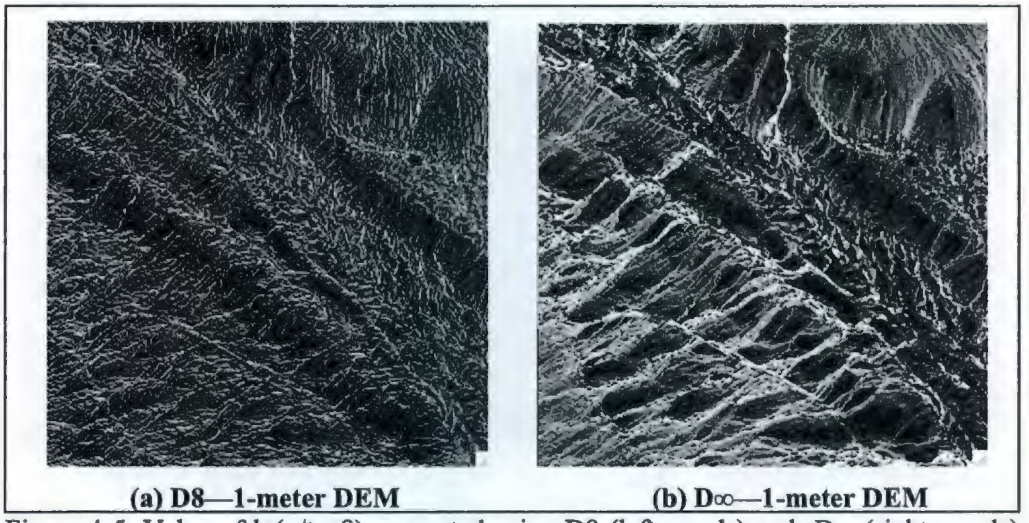

(a) D8—1-meter DEM **(b) D∞—1-meter DEM**

Figure 4-5: Value of $\ln(a/\tan\beta)$ computed using D8 (left panels) and D∞ (right panels) algorithms for 1-meter DEM of the Marmot Creek basin at the outlet section. The location of the center of DEM is 629066.500W, 5646383.500N.

Figure 4-6 illustrates the frequency distributions of $\ln(a/\tan\beta)$ computed by D8 and D∞ with 1- and 90-meter resolution DEMs of the Marmot Creek basin. Both relative frequency and cumulative frequency distributions of $\ln(a/\tan\beta)$ vary little between D8 and D∞ with 90-meter resolution DEM. The frequency distributions of $\ln(a/\tan\beta)$, produced by D8 and D∞, diverge more apparently for the 1-meter resolution DEM. The difference between algorithms is less subtle as grid cell size increases up to 90 m, due to the truncation of the lower tail of the distribution. Truncation occurs when increasing the

grid cell size because the minimum value for A is increased. The smaller grid size DEM has a greater proportion of grid cells with low ln(a/tanβ) values.

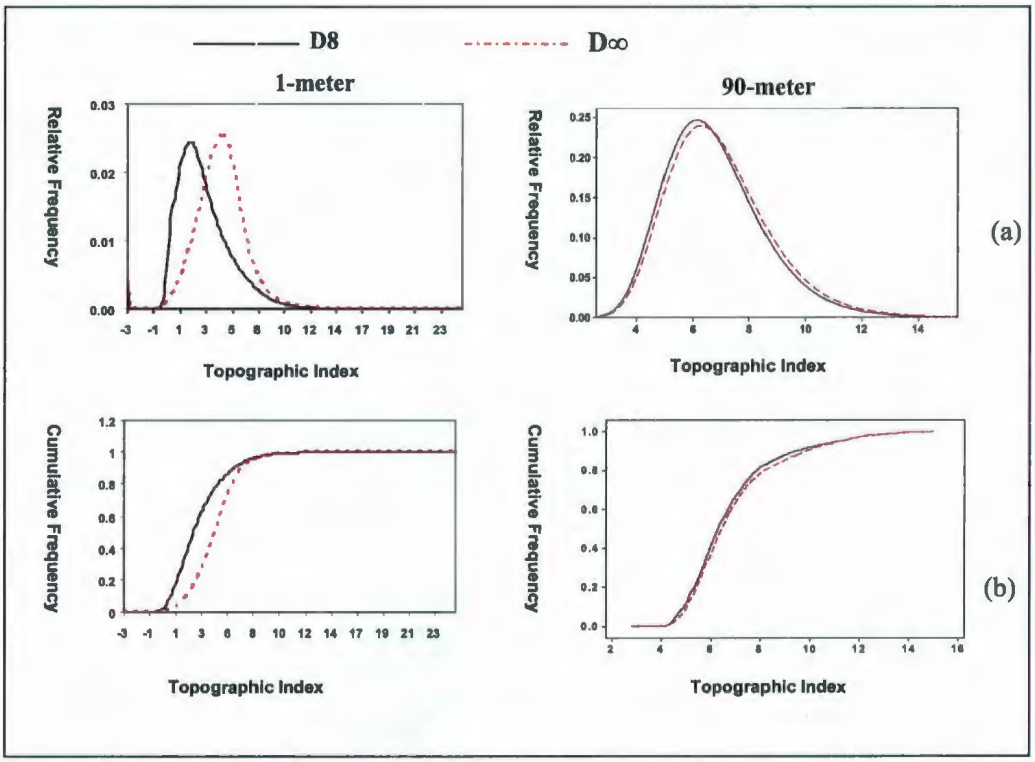

Figure 4-6: (a) Relative frequency distribution of ln(a/tanβ) by each method for 1-, and 90-meter DEMs. (b) Cumulative frequency distribution for ln(a/tanβ) by each method for 1-, and 90-meter DEMs.

Table 4-3 shows that, as grid size increases, the mean value of ln(a/tanβ)goes up, this because the percentage of the total drainage area classified in the lower region expands. At 1 m grid size DEM, less than 2.5% of the area is classified in the lower regions for each algorithm. Therefore, increasing the resolution of DEM will shrink the area of the lower region. This will result in a lower mean value of ln(a/tanβ).

Table 4-3: Statistics analysis of ln(a/tanβ) distributions computed for the Marmot Creek Basin using D8 and D∞ at each resolution DEMs.

Resolution	Algorithm	Variable	Mean
90-meter	D8	ln(a/tanβ)	6.77
	D∞	ln(a/tanβ)	6.95
1-meter	D8	ln(a/tanβ)	3.05
	D∞	ln(a/tanβ)	4.50

The main distinction between D8 and D∞ for estimating ln(a/tanβ) is the way in which the area potentially contributing flow is partitioned off from a center cell to its downslope neighbors. The most commonly used method is D8, which assigns the entire area from one cell to the steepest of its eight neighboring cells. As the flow is routed into only one cell, flow tends to become concentrated to distinct, often artificially straight lines (Seibert, 2007). D∞ uses triangular facets to remove the limitation of only eight possible directions in D8. However, this approach still allows only a single flow direction but enables the area to flow into one or two downslope cells forming the steepest triangle based on the resulting downslope vector.

The visual difference between algorithms based on maps of ln(a/tanβ) is apparent at high resolution DEM, but not pronounced at low resolution DEM. The cumulative frequency distributions of ln(a/tanβ) are not sensitive to the algorithms as grid cell size increases. The relative differences between D8 and D∞ are amplified at higher grid resolutions.

Tarboton (1997) compared the spatial distribution patterns of the upslope drainage area computed with D8 and D∞. He demonstrated that D8 resulted in no spreading, but when flow paths were aligned with the grid axes, cardinally or diagonally, D∞ procedure gave the same results as D8, and both were correct. However, when the topographic slope was

not aligned with one of the grid directions, the procedures differed. D8 followed the topographic slope at the cost of introducing some dispersion. It was also showed that on the basis of the evaluation of test statistics and examination of influence and dependence of maps, D∞ performed better than D8.

4.3. Summary

In this chapter, two common flow routing algorithms, D8 and D∞, are employed to determine the flow direction in the Marmot Creek basin in order to get the frequency distribution of $\ln(a/\tan\beta)$. In fine resolution DEM, the distinction is pronounced between different algorithms. In coarse resolution DEM, the difference is not very obvious. $\ln(a/\tan\beta)$ produced by 1-meter resolution DEM has the lower mean value than that calculated by 90-meter resolution DEM, because the percentage of the total drainage area classifies in the lower region decreases. Chapter 7 will further demonstrate which algorithm is more appropriate to be applied to the Marmot Creek basin through the simulation of TOPMODEL.

Chapter 5

Evaporative Resistance Estimate by CLASS

CLASS, a soil-vegetation-atmosphere transfer scheme (SVAT) for use in large-scale climate and hydrology models, was first developed in 1987 at the Meteorological Service of Canada (Verseghy, 2000). A detailed description of CLASS can be found in Verseghy (1991) and Verseghy *et al.* (1993). Briefly, CLASS provides a one-dimensional parameterization of surface-atmosphere interaction. It treats the land-surface as being comprised of three main elements: vegetation, soil, and snow. Each grid-cell can be divided up into four sub-areas, representing bare soil and vegetated areas with and without snow cover, which are treated separately. Within the vegetation sub-area, four basic canopy categories are recognized: needle-leaf tree-like, broad-leaf tree-like, crop-like, and grass-like. For each of the grid sub-areas, the energy balance is solved iteratively for the canopy and for the underlying (snow or soil) surface. The soil is divided into three layers of 0.10, 0.25, and 3.75 m thickness for the purpose of heat and

moisture transfers. Heat flow between layers is modeled using thermal diffusion theory. Water transfer between layers is modeled using Green-Ampt approach for infiltration, and Darcy theory for drainage (Bartlett *et al.*, 2000). Turbulent fluxes of sensible and latent heat are calculated using gradient turbulent diffusion theory.

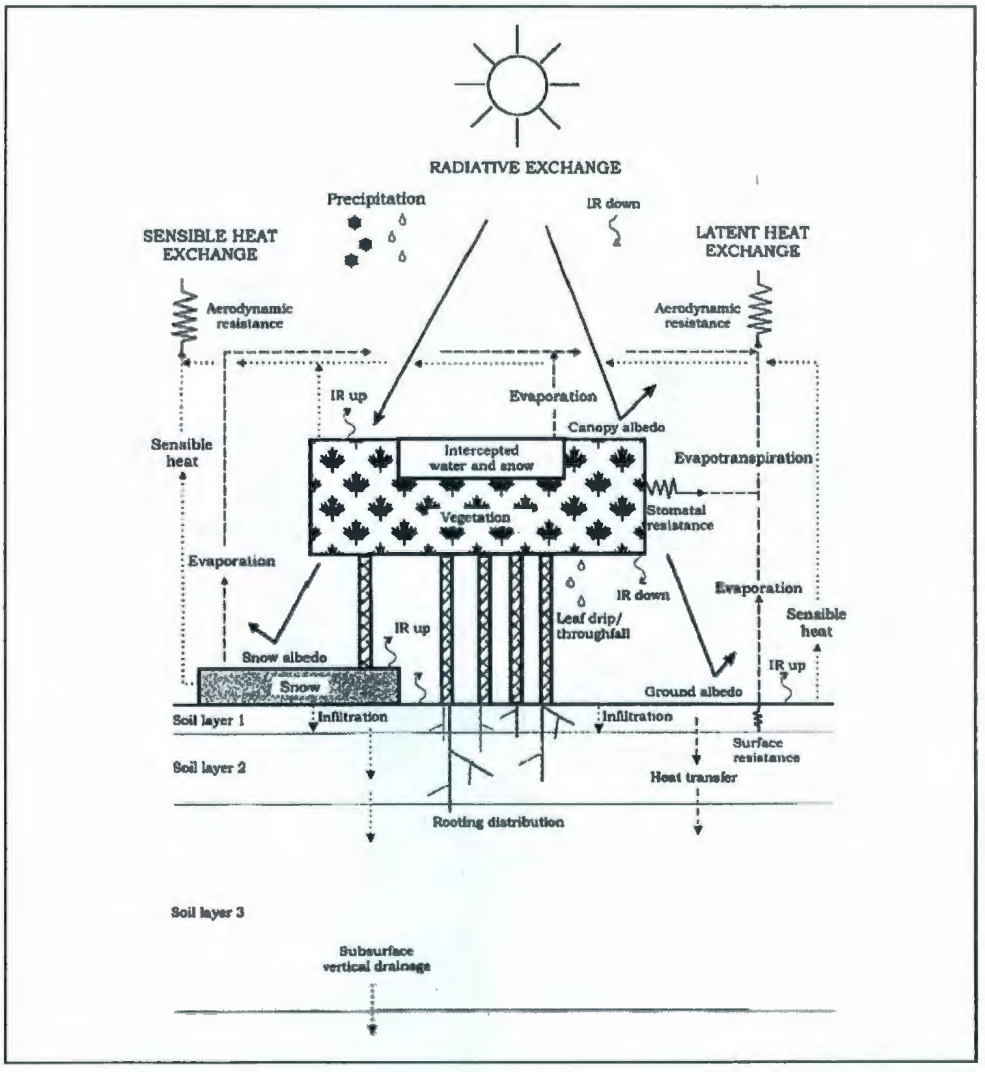

Figure 5-1: Schematic diagram of CLASS (from Verseghy, 2000).

Figure 5-1 shows the schematic diagram of CLASS, which is employed in this dissertation to estimate r_c of the vegetation canopy and r_a. r_c is a function of the density, size and degree of stomata opening. r_a, to water vapor and its accompanying latent heat, depends on the thickness of the boundary layer of air at the surface of the leaf. Water vapor must diffuse through this layer boundary after leaving the stomata. r_a is controlled by leaf size, morphology, and wind speed (Monteith *et al.*, 1990). r_c and r_a operate in series. Their relative magnitude determines which resistance is the dominant regulator of transpiration.

5.1. Model Parameters

The study area has been described in detail in Chapter 3. The Marmot Creek basin (50°57'N, 115°10'W) is located in the Kananaskis Valley. Elevation ranges from 1,585 to 2,804 m above the sea level. The lower reaches, extending to the tree line at 2,286 m, are covered with a dense stand of lodgepole pine and mature spruce fir up to 30.48 m tall. In the alpine area, shrubs and grasses give the way to the bare rocks and talus. The main soil types found in the basin are: Brunisolic Grey Wooded soils, Podzolic soils, Regosolic soils, Alpine Black soils, and local Gleysolic and Organic soils. Table 5-1 summarizes the primary site parameters in CLASS runs. Values must be assigned to the vegetation physiological parameters (fractional coverage, average albedo, roughness length, maximum and minimum leaf area index, standing mass, and rooting depth) and to the soil characteristics (percent sand, clay, and organic matter content).

Table 5-1: Model parameters for CLASS runs.

Parameter	Marmot Creek basin	Comments
Needleleaf fraction of grid cell	1.0	
Broadleaf fraction of grid cell	0.0	
Grass fraction of grid cell	0.0	
Maximum Leaf area index	6.1	
Minimum Leaf area index	5.0	
Canopy height (m)	25.9	Mean height, values from Storr *et al.* (1970)
Zero plane displacement (m)	17.27	2/3 canopy height
Roughness length (m)	1.59	1/10 canopy height
Visible albedo of needleleaf veg.	0.03	Values from Verseghy *et al.* (1993) are adjusted to match shortwave albedo measured above canopy
NIR albedo of needleleaf veg.	0.22	
Sand fraction (soil layers 1-3)	10.93%, 10.67%, 4.44%	Values from Beke (1969)
Clay fraction(soil layers 1-3)	25.6%, 33.1%, 33.5%	
Organic fraction (soil layers 1-3)	9.2%, 2.6%, 1.2%	
Rooting depth (m)	1.0	
Biomass density (kg m^{-2})	5	Value from Chen *et al.* (1997b)

CLASS is always initialized at midnight with the initial canopy temperature set to air temperature. The initial temperature and soil moisture values in the top two of three soil layers are estimated as weighted averages of measured values at the appropriated depths. Since the measured values do not extend very far into the third soil layer, it is not easy to define accurately the characteristics of this layer. The temperature and volumetric soil moisture of the third layer are initialized using the deepest measured values.

Seven meteorological variables required by CLASS are measured in the Hay Meadow and Vista View stations in the Marmot Creek basin. Stations' characteristics have been detailed introduced in chapter 3.

5.2. Stomatal Resistance

5.2.1. Method Description

Five main environmental factors, which are solar radiation, ambient CO_2 concentration, leaf-air vapor-pressure difference, leaf temperature, and leaf water content, would affect r_c under natural conditions. The changes in r_c are in turn reflected in the ambient temperature and humidity modulation due to the connection between the biota and the surrounding air-boundary layer resistance (Niyogi and Raman, 1997). r_c is modeled based on either photosynthesis calculation (Niyogi and Raman, 1997) or by scaling a minimum stomatal resistance (r_{smin}) (Alapaty *et al.*, 1997a). In CLASS, r_c is modeled by scaling r_{smin}. Based on the analysis of Schulze *et al.* (1995), unstressed stomatal resistance ($r_{c,u}$) for a given vegetation category can be calculated as a function of the incoming visible shortwave radiation K↓:

$$r_{c,u} = r_{smin}\kappa e / \ln[(K\downarrow + K\downarrow_{½}/\kappa e)/(K\downarrow \exp(-\kappa e \Lambda) + K\downarrow_{½}/\kappa e)] \qquad \text{Equation 5-1}$$

where r_{smin} is currently 0.05 s mm^{-1} for all vegetation categories, κe is the extinction coefficient for visible radiation (CXTEFF in CLASS), and $K\downarrow_{½}$ is the value of $K\downarrow$ at which $r_{c,u} = 2r_{smin}$.

Suboptimum environmental conditions for transpiration may result in stresses on the plant, which will lead r_c to be greater than its unstressed value. The effects of these stresses are modeled by defining functions of the air temperature (T), the air vapour pressure deficit (Δe), and the soil moisture suction (ψs). Functional relations are plotted in Figure 5-2. These functions are employed to derive $r_{c,l}$ of each vegetation category on the basis of $r_{c,u,l}$:

$$r_{c,i} = f_1(T) f_2(\Delta e) f_3(\psi s)\, r_{c,u,i} \qquad \text{Equation 5-2}$$

The air temperature function, $f(T)$, has a value of 1 for the temperatures between 5°C and 40°C, and has an arbitrary large value of 250 for the temperatures less than -5°C or greater than 50°C. Between these points it varies in a linear function.

$$f_1(T) \begin{cases} = 1.0, & 5°C \le T \le 40°C \\ = 250.0, & T \ge 50°C \text{ or } T \le -5°C \\ = 1.0/[1.0-(5.0- T) \times 0.1] & -5°C < T < 5°C \\ = 1.0/[1.0-(T- 40.0) \times 0.1] & 40°C < T < 50°C \end{cases} \qquad \text{Equation 5-3}$$

For the vapour pressure deficit function, $f(\Delta e)$, two alternate forms are provided respectively:

$$f_2(\Delta e) \begin{cases} = (\Delta e/10.0)^{cv2/cv1} & cv2 > 0 \\ = 1/\exp(-cv1\ \Delta e/10.0) & cv2 \le 0 \end{cases} \qquad \text{Equation 5-4}$$

where *cv1* and *cv2* are parameters depending on the vegetation categories. The soil moisture suction function, $f(\psi s)$, is expressed as:

$$f_3(\psi s) = 1 + (\psi s / c_{\psi 1})^{c\psi 2} \qquad \text{Equation 5-5}$$

where $c\psi 1$ and $c\psi 2$ are parameters depending on the vegetation categories. The aggregated r_c for the canopy over the bare ground sub-area is obtained as a weighted average over the vegetation categories. It is assumed that transpiration is suppressed when snow is present under the canopy. Therefore, r_c for this sub-area is set to a large number.

r_c measurements through porometery or gas-exchange techniques have high precision and accuracy, and hence a justifiable high cost. It is for this purpose that a cost-effective approach is required to give approximate r_c value. To estimate r_c by modeling is one of the practical reasons for the paucity of good and continuous data for the study region. The methodology described in this study is directed towards this objective.

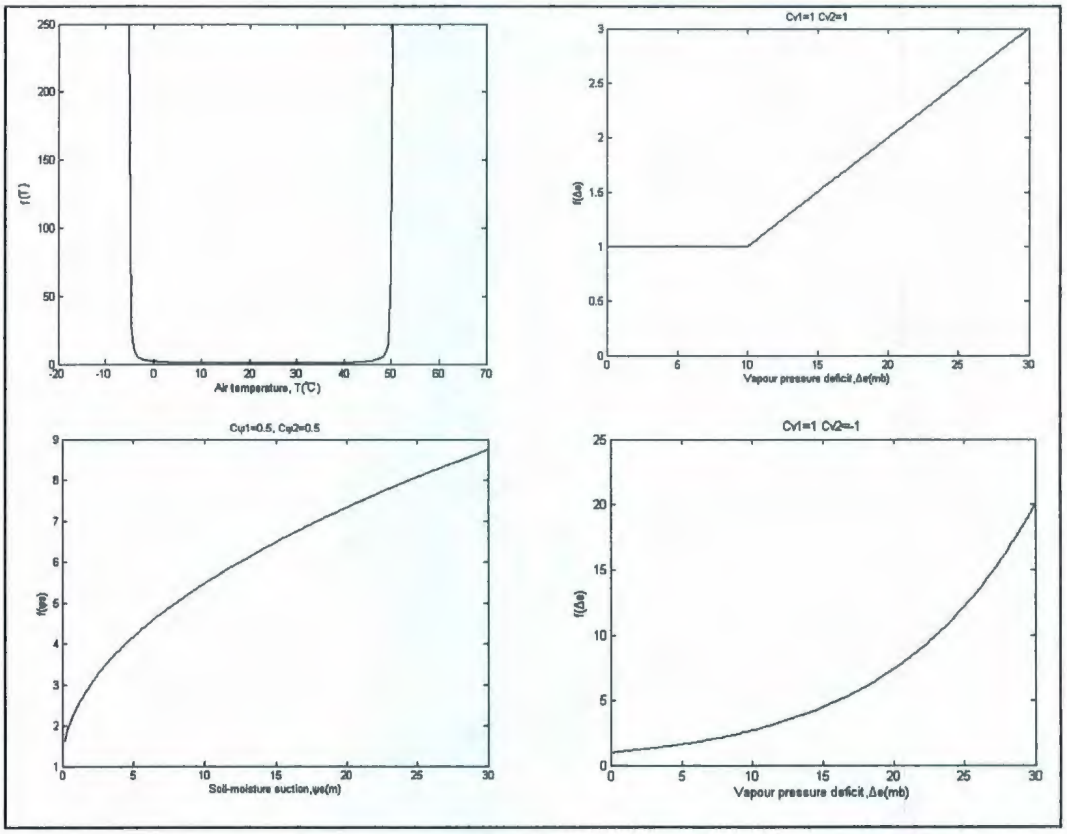

Figure 5-2: Effects of air temperature (T), soil moisture suction (ψs), and vapor pressure deficit (Δe).

5.2.2. Stomatal Resistance Results

Figure 5-3 shows the average seasonal behavior of r_c in the Marmot Creek basin in 2006 and 2007. CLASS would set r_c equal to 5,000 s m^{-1}, when the incoming short wave

radiation is less than 2 W m^{-2}. Therefore, r_c discussed here only concern the period from 9:00 a.m. to 5:30 p.m., when the incoming short wave radiation is greater than 2 W m^{-2}. In general, r_c were low in July-September 2006 and in May-September 2007, but the values of r_c rose quite sharply up to approximately 2000 s m^{-1} in October in 2006 and to 1200 s m^{-1} in 2007. There were three large peaks in the resistance in 2006: mid-September, mid-October, and end-October. On September 13th, a large rainfall exceeding the average occurred in the Marmot Creek basin with a mean daily temperature of 15 °C. In the same day, the average r_c increased sharply, up to 1000 s m^{-1}. This may indicate that the moisture stress caused the increase in r_c. On September 14th, r_c suddenly dropped to 0 s m^{-1}, with the temperature below 0°C, and the precipitation reached 0.1m day^{-1}. CLASS assumes that precipitation at air temperatures lower than 0 °C occurs as snow. The fractional coverage of snow is assumed to reach unity when the snow depth reaches 0.1 m. That is the reason why r_c of snow-covered vegetation was 0 s m^{-1} during that period, and this situation was sustained until the end of snow melting. A small amount of incoming radiation might result in the peaks in October both in 2006 and in 2007.

The modeled daytime r_c values averaged 239 s m^{-1} in 2006 and 267 s m^{-1} in 2007. Bartlett *et al.* (2003) evaluated r_c values at three boreal forest stands located near Thompson, Manitoba by CLASS. The modeled r_c values from these three sites fell in a similar range, with day time values averaging 250-400 s m^{-1}. Shuttleworth (1989) showed diurnal patterns of r_c from various temperature and tropical forests. Peak values in the long-term average data ranged from 66.7-125 s m^{-1}. He proposed 100 s m^{-1}as a suitable daytime average. Granier *et al.* (2000) presented plots of the relationship between r_c and vapor pressure deficit for 15 forests, including tropical, temperate, mountain, and a southern

boreal jack pine stand in central Saskatchewan. As inferred from the plots, r_c was highest (approaching 100 s m^{-1}) at the southern boreal jack pine stand, and the others ranged to 33.3 s m^{-1}, with an average of 50 s m^{-1}. Lafleur (1992) found r_c values in a spruce–tamarack forest near Churchill, Manitoba, ranging from 277 to 1136.4 s m^{-1}. As noted that r_c values in this study are similar as than those found at the Manitoba forest sites.

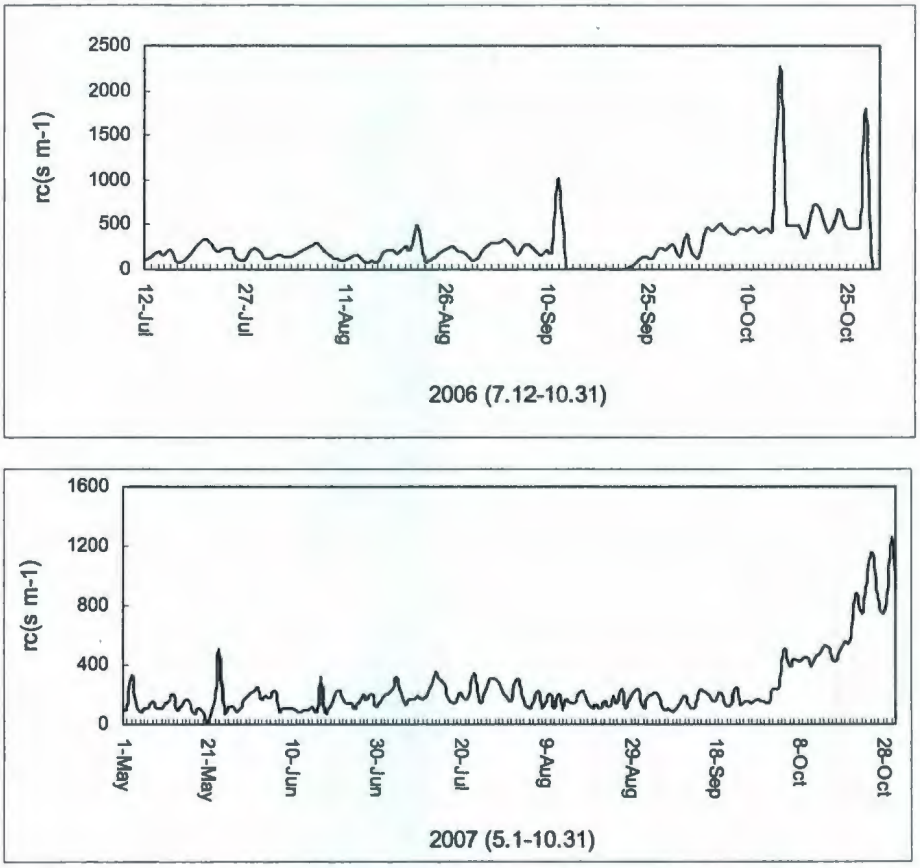

Figure 5-3: r_c throughout the growing season for day time in 2006 and 2007.

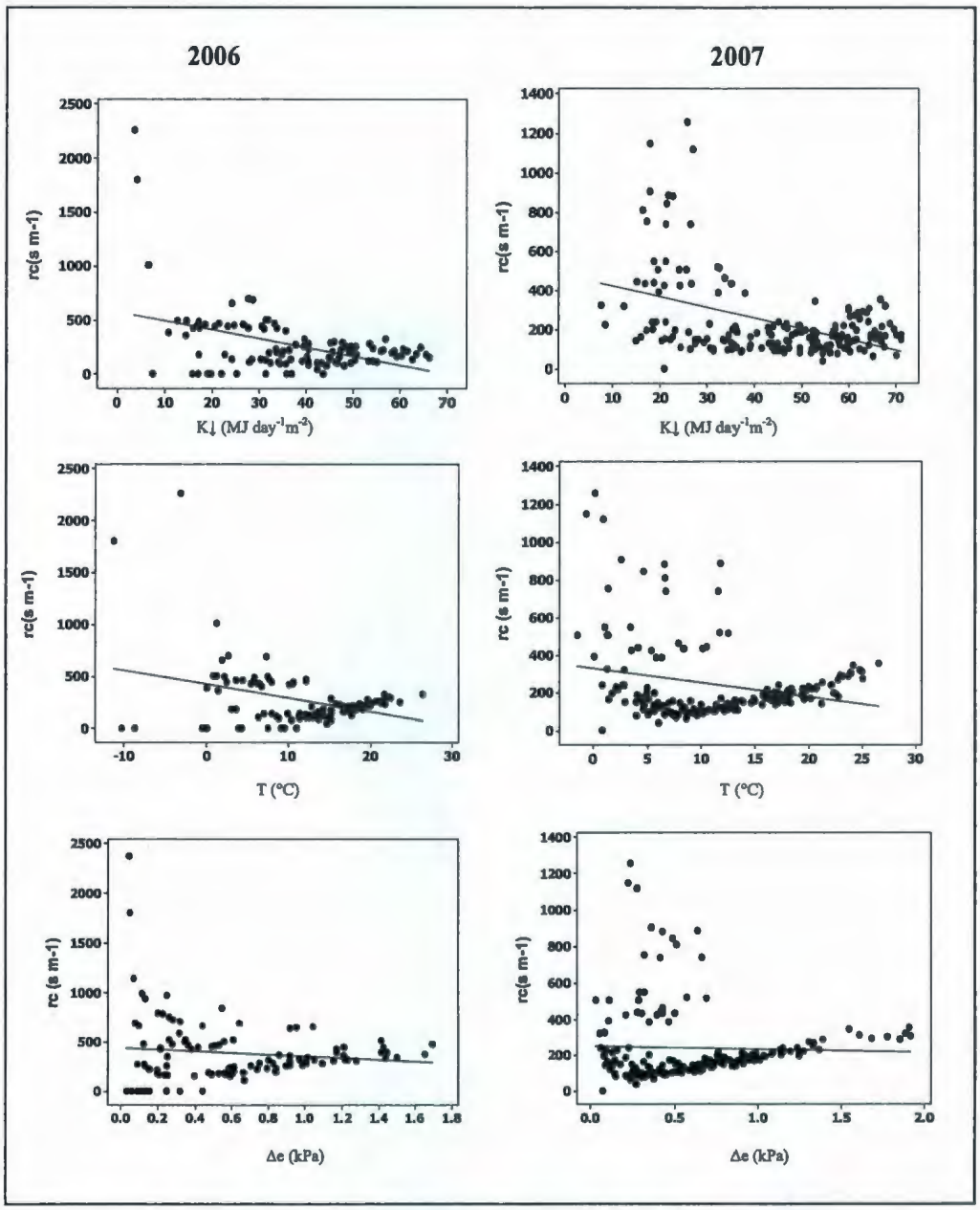

Figure 5-4: The relationship between r_c and K↓, T, and Δe in 2006 and 2007.

The focus will now centre on the relationships between resistance and environmental parameters, with the goal of estimating r_c independent of measurements. Figure 5-4 shows a plot of r_c against incoming solar short wave radiation (K↓), temperature (T), and

vapor pressure deficit (Δe). It can be concluded that along with the increase of solar radiation from 0 to 70 W m^{-2}, r_c has a decline trend. It seems that temperature has the similar effects. But many studies (Lindroth, 1985; Dolman and can den Burg, 1988; Granier *et al.*, 2000) indicate that a temperature function is not found to be significant at any of the sites. This occurs because temperature is positively correlated with both the vapor pressure deficit and the incoming solar short wave radiation. The influence of the vapor pressure deficit on r_c is not very pronounced in this study. This may be due to the interaction effects of other environmental parameters. However, ascend trends are still related to r_c as the vapor pressure deficit increases.

This investigation has shown that r_c does not respond in a simple manner to changing environmental conditions. Variability of the resistance, even over a short period, indicates the need for a more detailed understanding of stomatal behavior in field environments. Short period variations of r_c will occur as stomata respond to fluctuations in soil-water content. The variations will be imposed on long-term trends caused by seasonal changes in soil water, changes in the leaf area, and changes in leaf age. r_c will also be different for different species (Szeicz, 1969).

5.3. Aerodynamic Resistance

5.3.1. Method Description

Parameterizations of r_a to heat and water transfer have significant impact on the accuracy of estimated surface fluxes. CLASS calculates r_a from the surface drag coefficient (C_D) and the wind speed (v_a) above the canopy as

$$r_a = \frac{1}{C_D v_a} \qquad \text{Equation 5-6}$$

The drag coefficient for heat and water vapour fluxes, $C_{D,E}$, can be obtained by

$$C_{D,E} = \left[\frac{k}{\ln(\frac{z_m - z_d}{z_{0,E}})}\right]\left[\frac{k}{\ln(\frac{z_m - z_d}{z_{0,M}})}\right]\Phi_E \Phi_M \qquad \text{Equation 5-7}$$

The drag coefficient for the momentum, $C_{D,M}$, is

$$C_{D,E} = \left[\frac{k}{\ln(\frac{z_m - z_d}{z_{0,M}})}\right]^2 \Phi_M{}^2 \qquad \text{Equation 5-8}$$

where z_m (m) is the reference height, which is assigned a constant value of 50 m; z_d (m) is the zero-plane displacement, $z_d = 0.70 z_{veg}$, where z_{veg} is canopy height; k=0.04 is von Karman's constant; $z_{0,M}$ (m) is the roughness length for momentum transfer, $z_{0,M} = 0.10 z_{veg}$. Following results presented by Garratt and Hicks (1973) and others, $z_{0,E}$ (m) can be obtained from $z_{0,M}$ for the four major vegetation types and for bare soil:

$z_{0,E} = z_{0,M}/2.0$	(trees)	Equation 5-9(a)
$z_{0,E} = z_{0,M}/7.0$	(crops)	Equation 5-9(b)
$z_{0,E} = z_{0,M}/12.0$	(grass)	Equation 5-9(c)
$z_{0,E} = z_{0,M}/3.0$	(bare soil)	Equation 5-9(d)

Φ_M is a stability correction factor dependent on $z_{0,M}$. (McFarlane *et al.*, 1992). Φ_E is the stability corrective factor calculated using $z_{0,E}$.

Above canopies, in an acceptably wide range of stability, the profiles of temperature, vapor pressure, and wind are usually similar. When this condition is satisfied, transfer coefficients for momentum, in some extent, can be used to calculate fluxes of heat and water vapor (Monteith, 1965). This study employs two approaches to estimate r_a over the Marmot Creek basin. The aerodynamic resistance for the latent heat flux simulated by CLASS (r_{ah}) is compared with the aerodynamic resistance obtained from the flux of momentum (r_{ah0}), which is introduced by Monteith (1965) described by

$$r_{ah0} = \frac{\left[\ln\left(\frac{z_m - z_d}{z_0}\right)\right]^2}{k^2 v_a} \qquad \text{Equation 5-10}$$

Equation 5-10 is valid only under neutral conditions, when the diffusivities of water vapor and heat are identical to the diffusivity of momentum. If it is assumed that the same transfer processes are involved for water vapor and momentum, $\Phi_M = \Phi_E = 1$ and $z_{0,E} = z_{0,M}$, Equations 5-6 and 5-10 are expressions of the same resistance. The objective of this study is to investigate how difference between r_{ah} and r_{ah0}.

5.3.2. Aerodynamic Resistance Results

The simulations are conducted during the period from July 12th to October 31st, 2006 and from May 1st to October 31st, 2007. The seasonal variations of aerodynamic resistance during daytime (9:00 a.m. to 5:30 p.m.) are analyzed. Figure 5-5 shows the comparisons of seasonal trends in the average reciprocal of aerodynamic resistance ($1/r_a$), which can be defined as aerodynamic conductance, from the two methods over the needleleaf forest surface in the Marmot Creek basin. Although the values of $1/r_{ah}$ and $1/r_{ah0}$ are not consistently the same, it seems that they follow the same trend.

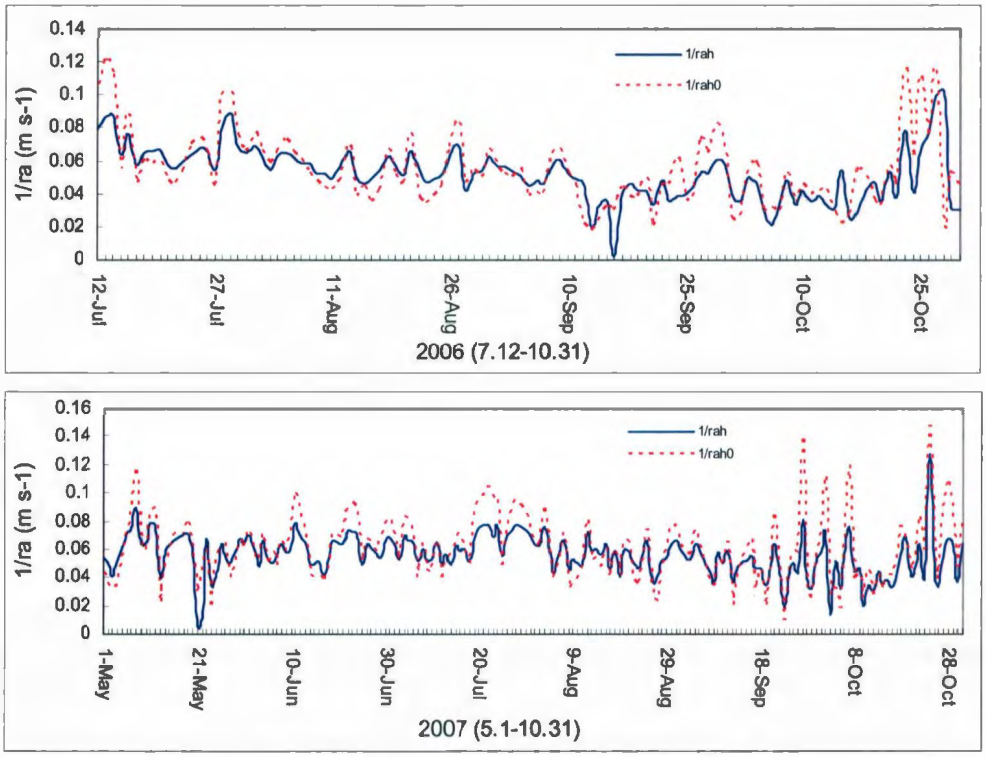

Figure 5-5: Seasonal variation of $1/r_a$ calculated using Monteith method ($1/r_{ah0}$) and CLASS ($1/r_{ah}$) in 2006 and 2007.

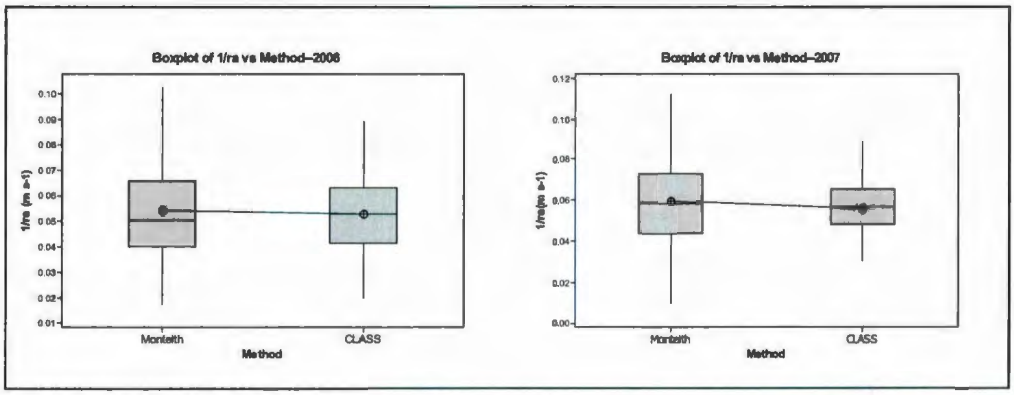

Figure 5-6: Boxplot of $1/r_a$ calculated by CLASS and Monteith method in 2006 and in 2007.

The daytime $1/r_{ah}$, modeled by CLASS, had the average value of 0.053 m s^{-1} in 2006 and 0.056 m s^{-1} in 2007, which were 0.0017 m s^{-1} and 0.004 m s^{-1} lower than those modeled by Monteith (1965) method, respectively. In the boxplot of Figure 5-6, it can also be found that $1/r_{ah0}$ is overestimated compared to $1/r_{ah}$ throughout the entire observation period. The discrepancies between $1/r_{ah}$ and $1/r_{ah0}$ are probably attributable to the different turbulent eddies responsible for the transport of water vapor and momentum. Under neutral conditions, the diffusivity of water vapor is identical to the diffusivity of momentum, because the same turbulent eddies are responsible for the transport of both quantities. However, under unstable conditions, the vertical movement of heat is enhanced beyond that of wind. Therefore, there can be a significant vertical transport of water vapor but little transport of momentum. These conditions typically occur when wind speed is low and the surface is strongly heated by the sun, inducing strong convection. Conversely, when the lapse rate near the ground is stable, turbulence is suppressed by buoyancy effects. This situation is typical when warm air lies over a cold surface, such as packed snow. Henceforth, it can be deduced that under unstable conditions, $r_{ah} < r_{ah0}$, $1/r_{ah} > 1/r_{ah0}$; under stable conditions, $r_{ah} > r_{ah0}$, $1/r_{ah} < 1/r_{ah0}$; under neutral condition, $r_{ah} = r_{ah0}$, $1/r_{ah} = 1/r_{ah0}$.

In actuality, r_{ah0} agrees fairly closely to r_{ah}, even though Equation 5-10 is valid only when the diffusivities of water vapor and momentum are equal.

Many models have been developed to estimate r_a under stable or unstable conditions base on Motheith's model (1965), like Xie Xianqun's model (1988), Monteith-Hatfield model (Monteith, 1973; Hatfield, 1983), Choudhury-2 model (Choudhury *et al.*, 1986, 1988). As these models involved much more parameters than Motheith's model (1965), some

parameters are not easy to obtain from measurement, for this reason, despite its invalidity under stable and unstable condition, Monteith's model is still common practice to be used to estimate r_a in the Penman-Monteith equation.

5.4. Summary

Plant evapotranspiration is a physical process in which part of the net radiation energy is converted into latent heat. Determination of resistance, the reciprocal of conductance, is a key topic in the simulation of evapotranspiration. In this study, CLASS estimats r_c as a function of solar radiation, temperature, vapor pressure, as well as soil water content. The response of stomata to light began to increase when solar radiation decrease. r_c showes little response to vapor pressure deficit when vapor pressure deficit greater than 1.0 kPa. The maximum r_c in the Marmot Creek basin in this study can reach 2000 m s^{-1}, however, the minimum r_c is only 0 m s^{-1}. In this study, r_a is calculated by CLASS which is compared to the value determined through the Monteith method under neutral condition. The results of these two methods are fairly close. As the real data of r_c and r_a are not available to be measured in the meteorological stations in the Marmot Creek basin, the results of this part will be directly applied to estimate PET in the next chapter.

Chapter 6

Potential Evapotranspiration

One objective of this chapter is to use the Penman-Monteith model to quantify PET of the Marmot Creek basin. PET is the maximum rate of evapotranspiration from a vegetated catchment under the condition of unlimited moisture supply and without advection or heat storage effects (Thomas, 2000). The Penman-Monteith model is the most physically realistic method for which sufficient station data are available to analyze PET on a broad scale. Estimated PET will be applied to TOPMODEL in this study to simulate the stream flow in the Marmot Creek basin. An accurate estimation of PET is very useful for appropriate stream flow simulation by TOPMODEL. The impacts of r_a and r_c on PET will be discussed in this chapter.

6.1. Method Description

The Penman-Monteith equation is a one-dimensional model of the evapotranspiration process, treating the vegetation canopy as a single uniform cover. The Penman-Monteith equation can be written as:

$$PET = \frac{\Delta \cdot (K + L) + \rho_a \cdot c_a \cdot C_{at} \cdot e_a^* \cdot (1 - W_a)}{\rho_w \cdot \lambda_v \cdot [\Delta + \gamma \cdot (1 + C_{at} / C_{can})]} \quad \text{Equation 6-1}$$

where Δ is the slope of the relation between saturation vapor pressure and temperature, which can be expressed as:

$$\Delta = \frac{2508.3}{(T+237.3)^2} \cdot \exp\left(\frac{17.3 \cdot T}{T+237.3}\right) \quad \text{Equation 6-2}$$

where Δ is in kPa K^{-1} and T is in °C; $K+L$ is the net radiation, in MJ $m^{-2}day^{-1}$; ρ_a is the density of air, which is approximately equal to 1.220 kg m^{-3} at sea level; c_a is the heat capacity of air, and it is equal to 1.00×10^{-3} MJ $kg^{-1}K^{-1}$; *Cat* (m s^{-1}) is the atmospheric conductance for water vapor, which is the inverse of r_a calculated in the previous chapter; e_a^* is the saturation vapor pressure, and its value can be calculated as:

$$e_a^* = 0.611 \cdot \exp\left(\frac{17.3 \cdot T}{T+237.3}\right) \quad \text{Equation 6-3}$$

where e_a^* is in kPa and T is in °C. *Wa* is the relative humidity, and it is the ratio of its actual vapor pressure, e_a, to its saturation vapor pressure:

$$W_a \equiv \frac{e_a}{e_a^*} \quad \text{Equation 6-4}$$

ρ_w is the mass density of the water, and it is approximately equal to 1.0×10^3 kg m^{-3}.

λ_v is the latent heat of vaporization, and it decreases as the temperature of the evaporating surface increases. This relation is given approximated by

$$\lambda_v = 2.50 - 2.36\times10^{-3} \cdot T \quad \text{Equation 6-5}$$

where λ_v is in MJ kg^{-1} and T is in °C.

γ is the psychrometric constant, and it can be calculated as

$$\gamma \equiv \frac{c_a \cdot p}{0.622 \cdot \lambda_v} \qquad \text{Equation 6-6}$$

where p is the pressure in kPa. Pressure is a function of elevation, and varies slightly over time at a given location.

C_{can} is the canopy conductance, which is the reciprocal of canopy resistance. It can be estimated as:

$$C_{can} = f_s \cdot LAI \cdot C_{leaf} \qquad \text{Equation 6-7}$$

where f_s is a shelter factor accounting for the fact that some leaves are sheltered from the sun and wind and thus transpire at lower rates. Values of f_s range from 0.5 to 1, and decrease with the increase of leaf area index (LAI) (Dingman, 2002). A value of f_s =0.5 is probably a good estimate for a completely vegetated area (Dingman, 2002). The average estimated value of LAI is 6.0 for the conifer forest (Dingman, 2002). C_{leaf} is the somatal conductance, which is the inverse of r_c calculated by CLASS in chapter 5. PET describes the maximum possible evapotranspiration under specific climatic situations with unlimited water reserves in the soil. Thus, r_c has the function of the soil moisture suction ($f(\psi s)$) equal to 1 when it is employed to estimate PET, which means leaf water content does not control r_c in this condition. The canopy resistance is a bulk measure of the stomatal resistance of the leaf as a whole. This resistance is in reality no uniquely controlled by the individual leaf stomatal resistance.

The meteorological data, including temperature, net solar radiation, and actual vapor pressure, required by the Penman-Monteith model are obtained from Vista View and Hay

Meadow stations in the Marmot Creek basin. The properties of these stations are summarized in Chapter 3. Periods of meteorological record for these two stations are not long enough for an analysis of year-to-year variation of PET, only July 12th to October 31st, 2006, and May 1st to October 31st, 2007 are concerned in this study. Statistical analysis, including the determination of means, minimum, maximum, analysis of variance, and Sign tests, are performed using the Minitab statistical package, Version 14 to analyze the results.

6.2. Modeling Results

6.2.1. Seasonal Variation of Potential Evapotranspiration

Figure 6-1 shows the seasonal change of PET over the Marmot Creek basin for the periods of July-October 2006 and May-October 2007 with r_a obtained through CLASS (PET_c).The mean daily PET_c was estimated to be 9.521 mm day^{-1} in 2006 and 10.520 mm day^{-1} in 2007. Therefore, the average actual water amount evaporated from lakes, evaporated from soils, and transpired by the vegetation was expected to be less than 9.521 mm day^{-1} in 2006 and 10.520 mm day^{-1} in 2007. The lowest PET_c (0.0941 mm day^{-1}) occurred on October 16th, 2006, was mainly caused by the lower incoming solar radiation. The highest PET_c (17.161 mm day^{-1}) was found on May 31st, 2007. Intense PET_c, over 14 mm day^{-1}, occurs in July, which is the driest period of the year. October has the lowest value of PET_c, which is equal to half the peak value in July, due to the least solar radiation being received by the surface at that time.

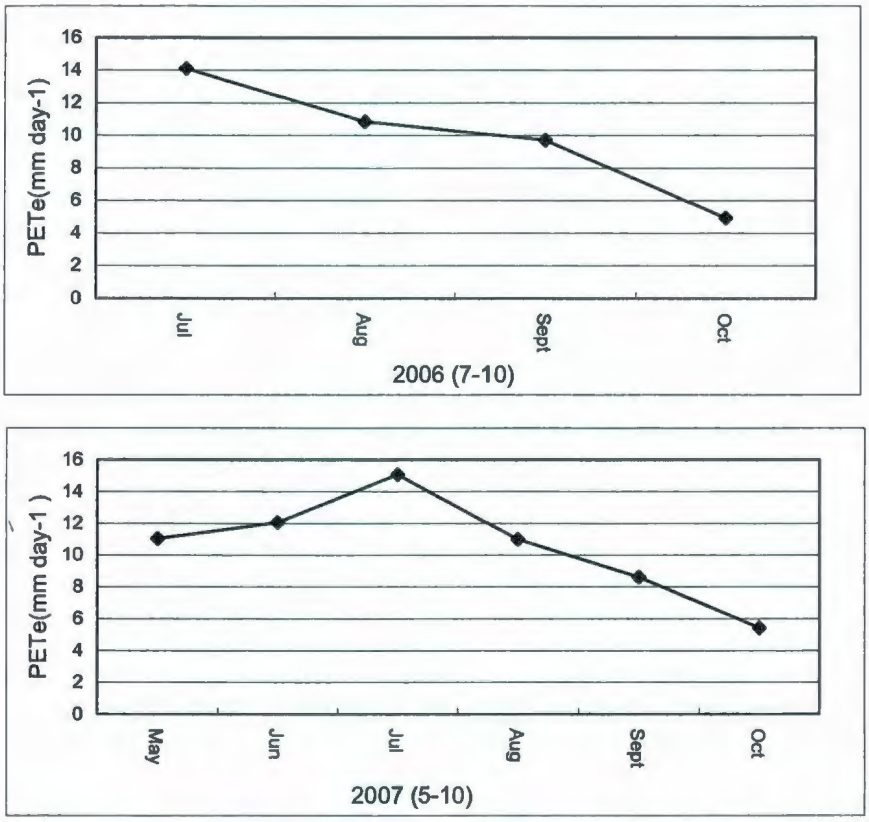

Figure 6-1: Estimated mean monthly PET with r_a produced by CLASS in 2006 and 2007 over the Marmot Creek basin.

During hourly sampling, Figure 6-2 shows the same trends as seasonal sampling for PET_e in 2006 and 2007. The peaks of these four sampling hours all occurred in July, and the minimum value of PET_e could always be found in October. Mean monthly PET_e values did not significantly increase at 12:00 and 14:00 compared to 10:00 and 16:00 in 2006 and 2007 (p-value>0.05). In 2006, at 16:00, PET_e was on average (7.33 mm day^{-1}) only 2.09 mm day^{-1}lower than at 10:00 (9.31 mm day^{-1}). PET_e was much lower at 16:00 compared to 12:00 (12.56 mm day^{-1}) and 14:00 (12.53 mm day^{-1}). During the first two months of sampling in 2007, May and June, mean monthly PET_e at 10:00 (10.62 mm day

$^{-1}$) was lower compared to 12:00 (13.49 mm day^{-1}), 14:00 (13.39 mm day^{-1}), and 16:00 (11.30 mm day^{-1}) .

Chen *et al.* (2006) assessed PET by the Penman-Monteith equation for 101 stations on the Tibetan Plateau and surrounding areas with the time series of 1961-2000. They found that annual PET rates peaked at more than 0.7 m in the 1970s and remained below 0.6 m in the 1960s and 1990s. The authors explained that changes in wind speed and to a lesser degree relative humidity were found to be the most important meteorological variables affecting PET trends on the Tibetan Plateau, while changes in sunshine duration played an insignificant role. Stable daytime temperatures on the Tibetan Plateau had limited the importance of temperature trends for changes of PET rates. Wang and Georgakakos (2007) adopted the Penman-Monteith equation to estimate PET in the 3300 km^2 Panama Canal watershed for the historical period 1985-2002. The results showed that the mean annual PET over the Panama Canal watershed was estimated to be less than 0.94 m on average. They found that the dry season tended to produce significantly more evaporation than the rainy season. They also found that the reduction of the received solar radiation at the surface was the main reason for the decrease of annual PET.

Of note is that PET values in this study are bigger than those found at most sites, as this study does not assess PET in the winter seasons. It seems that for the different sites, the dominant meteorological factors controlling PET are different.

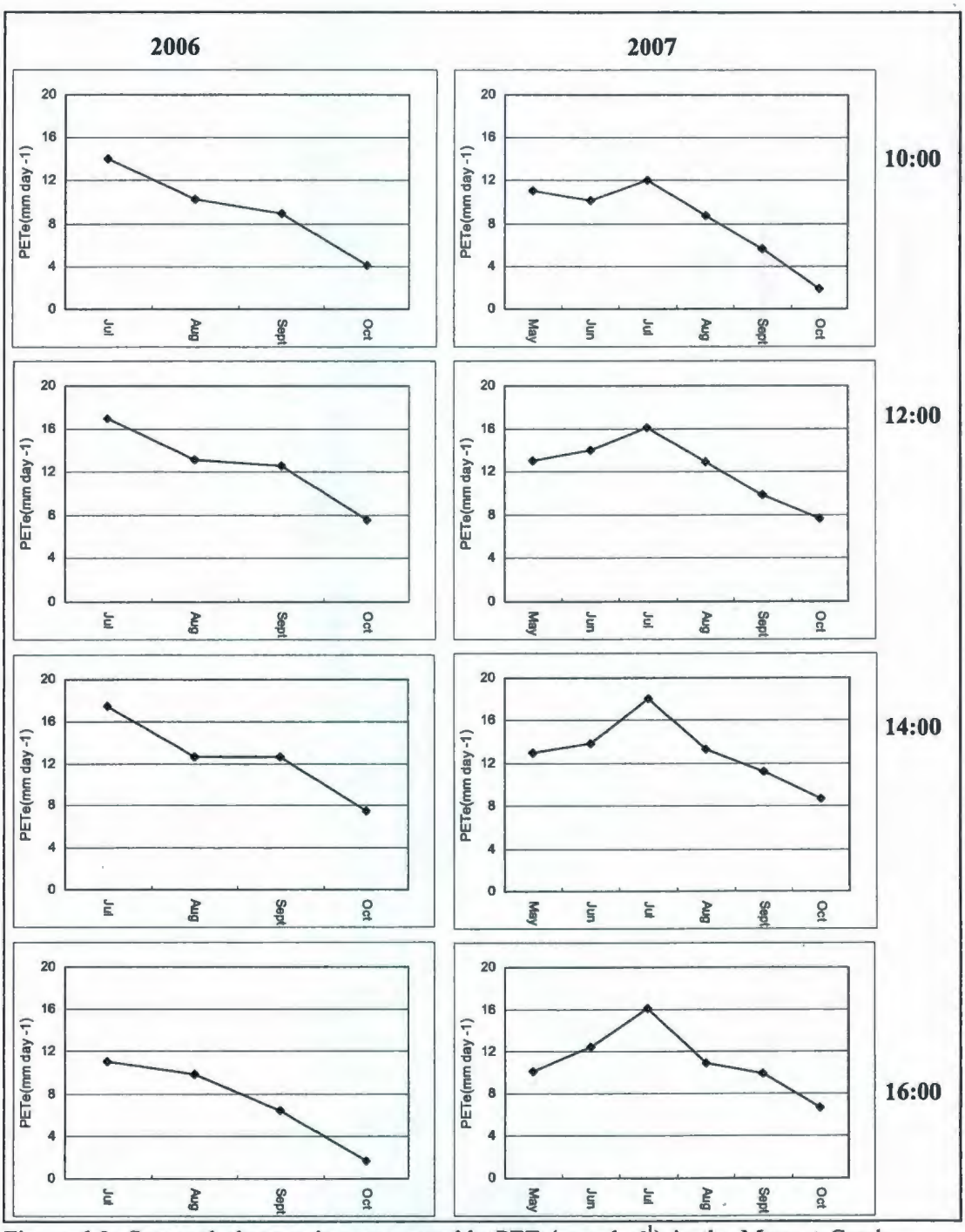

Figure 6-2: Seasonal changes in mean monthly PET (mm day^{-1}) in the Marmot Creek basin estimated at 10:00, 12:00, 14:00 and 16:00.

6.2.2. Aerodynamic Resistance Effects on Potential Evapotranspiration

Evapotranspiration is governed mainly by two processes: one is the rate of heat input necessary to change liquid water into vapor, and the other is the ease with which the vapor leaves the evapotranspiration surface. The Penman-Monteith combination method for estimating evapotranspiration, therefore, includes both a radiation term and a resistance term.

In order to assess the validity of the estimation of PET_n with r_{ah0} computed by Monteith method under neutral conditions, PET_n will be compared with PET_e with which r_{ah} is obtained from CLASS.

PET, estimated with different aerodynamic resistances, appeared identical in both 2006 and 2007, as seen in Figure 6-3. The difference between these two sets of PET can also be described by statistic analysis. The results, summarized in Table 6-1, indicate that compared with PET_e, PET_n had a larger mean value and smaller variance in both 2006 and 2007, but the differences were not very obvious. In order to get a more exact conclusion, the Sign test is used to examine whether these two sets of PET are significantly different or not both in 2006 and 2007. Table 6-2 summarizes the results of the test.

Table 6-1: Statistics analysis of PET calculated with different r_a in 2006 and 2007.

Year	Variable	Mean	Variance	Minimum	Median	Maximum
2006	PETe	9.521	20.460	0.0941	10.227	17.111
	PETn	9.602	20.213	0.141	9.788	17.815
2007	PETe	10.520	21.356	0.808	11.253	17.161
	PETn	10.617	20.886	0.905	11.285	17.216

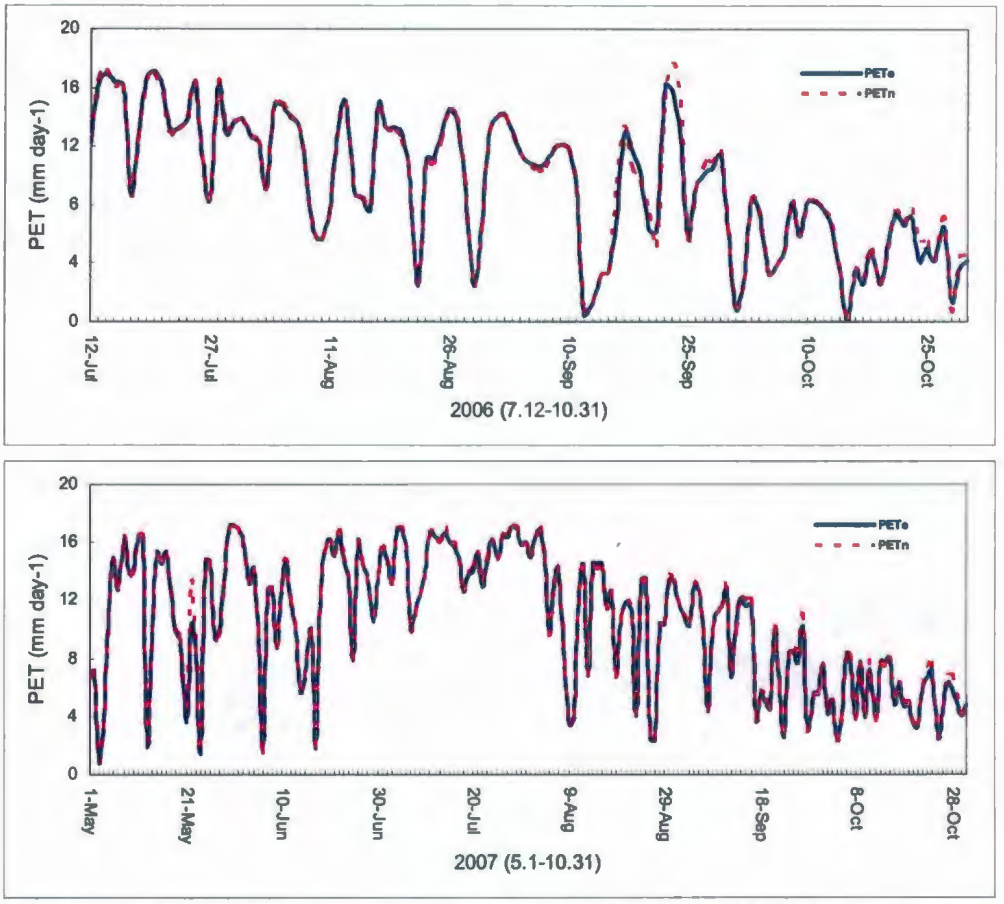

Figure 6-3: Estimated PET with r_a calculated by Moneith method and CLASS in 2006 and 2007.

The Sign test is based on the hypothesis that PET_e and PET_n are not equal. In 2006, its p-value is equal to 0.7042 greater than 0.05, which suggests that the overall values of PET_e and PET_n are not significantly different at the 95% confidence level. But in 2007, its p-value is less than 0.05, so the difference between PET_e and PET_n in 2007 is significant. The discrepancy between these two data sets is -0.07167, which indicates that PET_e tends to be larger than PET_n in 2007.

Table 6-2: The results of the Sign test for the difference of PET with different r_a in 2006 and 2007.

Sign test of median = 0.00000 versus not = 0.00000							
	N	**Below**	**Equal**	**Above**	**P**	**Median**	**Sign Test[a]**
2006	111	58	0	53	0.7042	-0.03833	T
2007	184	117	0	67	0.0003	-0.07167	F

a: T=true hypothesis, F=false hypothesis

Comparisons of PET_e and PET_n for some selected days are plotted in Figure 6-4. The best agreement between PET_e and PET_n was observed on DOY 221 (Figure 6-4b). On this day, the p-value of the Sign test was equal to 0.845, so the difference between these two PET data sets was not significant. The p-values of the other three days comparisons were all less than 0.05. The greatest disagreements were found on a cold, rainy day, DOY 256 (Figure 6-4c). On DOY 256, PET_n tended to overestimate PET_e during the daytime and night time. The same behavior could be found on DOY 196 morning and DOY 291 midday.

Bailey and Davies (1981) studied the effect of uncertainty in r_a on evaporation estimates from the Penman-Monteith model. The result showed that evaporation estimates from a soybean crop were insensitive to r_a. This insensitivity was attributed to a strong link between evaporation and the vapor pressure deficit of the air and bulk stomatal resistance. In their study, the sensitivity of r_a to errors in surface roughness and zero-plane displacement was considered. However, large errors in these had little effect on calculated evaporation. Bailey and Davies (1980) demonstrated that errors incurred by ignoring atmospheric stability were small in estimating both r_a and evaporation. They suggested that evaporation could be adequately from single-level measurements of

windspeed. The insensitivity of evaporation estimated by the Penman-Monteith method to r_a had also been shown previously for Douglas fir forest by Tan and Black (1976). In most previous work, r_{ah0} has been used instead of r_{ah} in estimating evapotranspiration.

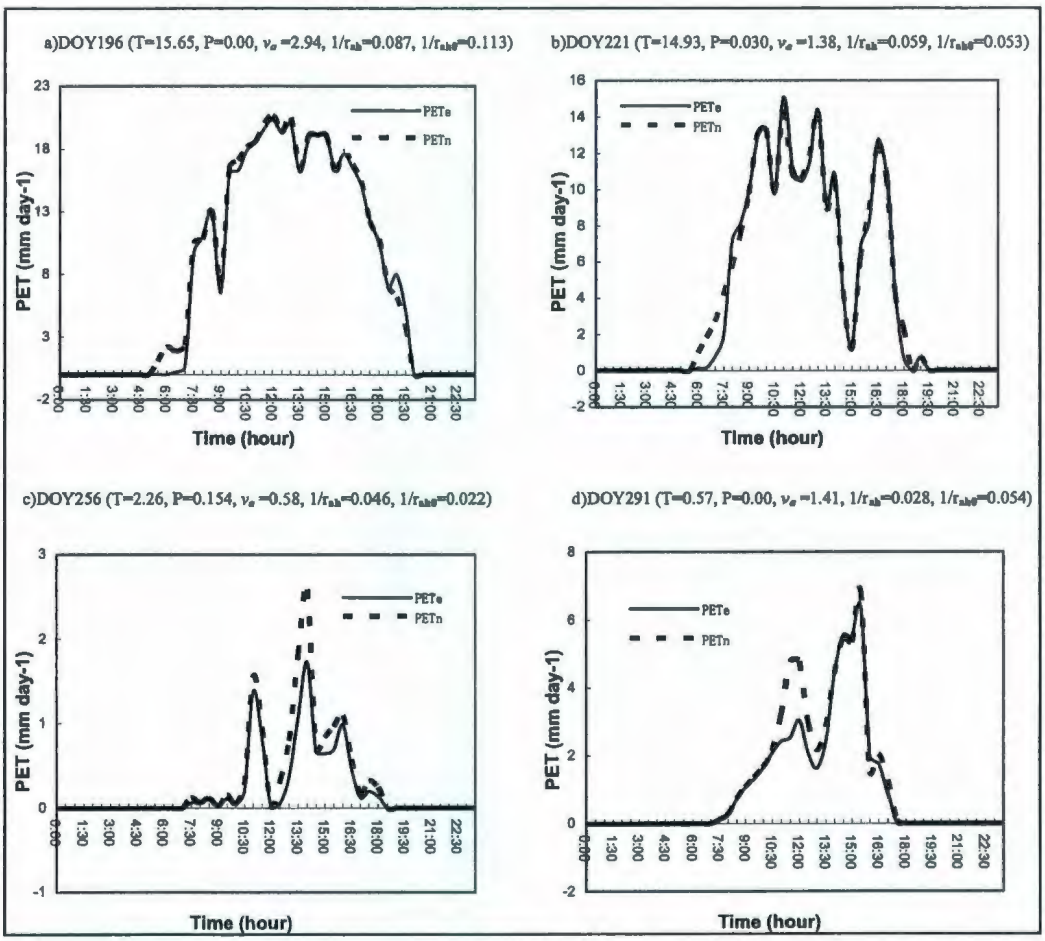

Figure 6-4: Hourly values of PET obtained by the Penman-Monteith equation with r_a coming from the Monteith method and CLASS, where T (°C) is the temperature, P (m day^{-1}) is the precipitation, and v_a (m s^{-1}) is the wind speed.

In this study, PET_e and PET_n were not significantly different in 2006. Even in 2007, the discrepancies were sufficiently small that even if they were neglected (r_{ah0} used in place of r_{ah}); PET can still be calculated to accuracy within 5% for most days.

6.2.3. Stomatal Resistance Effect on Potential Evapotranspiration

The evapotranspiration rate of a plant is controlled by the variable-aperture stomates on one or both sides of the plant's surface. The loss of water through the stomates provides the water potential gradient driving the movement of water and solutes within the plant and in the soil. The objective of this section is to evaluate the response of the Penman-Monteith equation to different stomatal resistances. The behavior of the Penman-Monteith formula for different r_c conditions is investigated for a range of vapor pressure deficits ($\Delta e=e_{sat}(Ta)-e_a$). The Δe range is used to evaluate the effects of dry, intermediate, and moist air cases. $1/r_c$ values vary within the range 0.008 -- ∞ m s^{-1}. Figure 6-5 shows the results for the moisture (Δe=0.30 kPa) case, the intermediate moisture (Δe=0.86 kPa) case, and the dry (Δe=1.91 kPa) case, under different $1/r_a$ conditions. PET_e is plotted against the time in DOY121, 131, and 196, in 2007.

In the case of small moisture deficit, the average value of PET_e varies from 5.344 mm $day^{-1}$to 2.647 mm day^{-1} with $1/r_c$ decreasing from infinite to 0.008 m s^{-1}. PET_e under the dry (14.78 mm day^{-1} on average) and intermediate moisture (12.61 mm day^{-1} on average) cases are significantly increased (p-value<0.05) compared to that under the moisture condition (4.30 mm day^{-1} on average). This may be attributed to the fact that the stomates close partially in order to reduce the outflow of water from the plant through evapotranspiration when the plant is under moisture stress.

The differences between PET_e with $1/r_c=\infty$ and $1/r_c$ =0.25m s^{-1} under these three weather conditions are not obvious. This means that when r_c decreases to a certain level, PET will release the control of the stomata operation, and PET will not change or this change will be sufficiently small. It is important to emphasize that the stomata of most plant species

close in the dark, therefore, at night, r_c would be high and PET is nearly equal to 0, but in this study, as r_c remains constant during the entire day, PET equal to 0 is attributed to the negative net radiation.

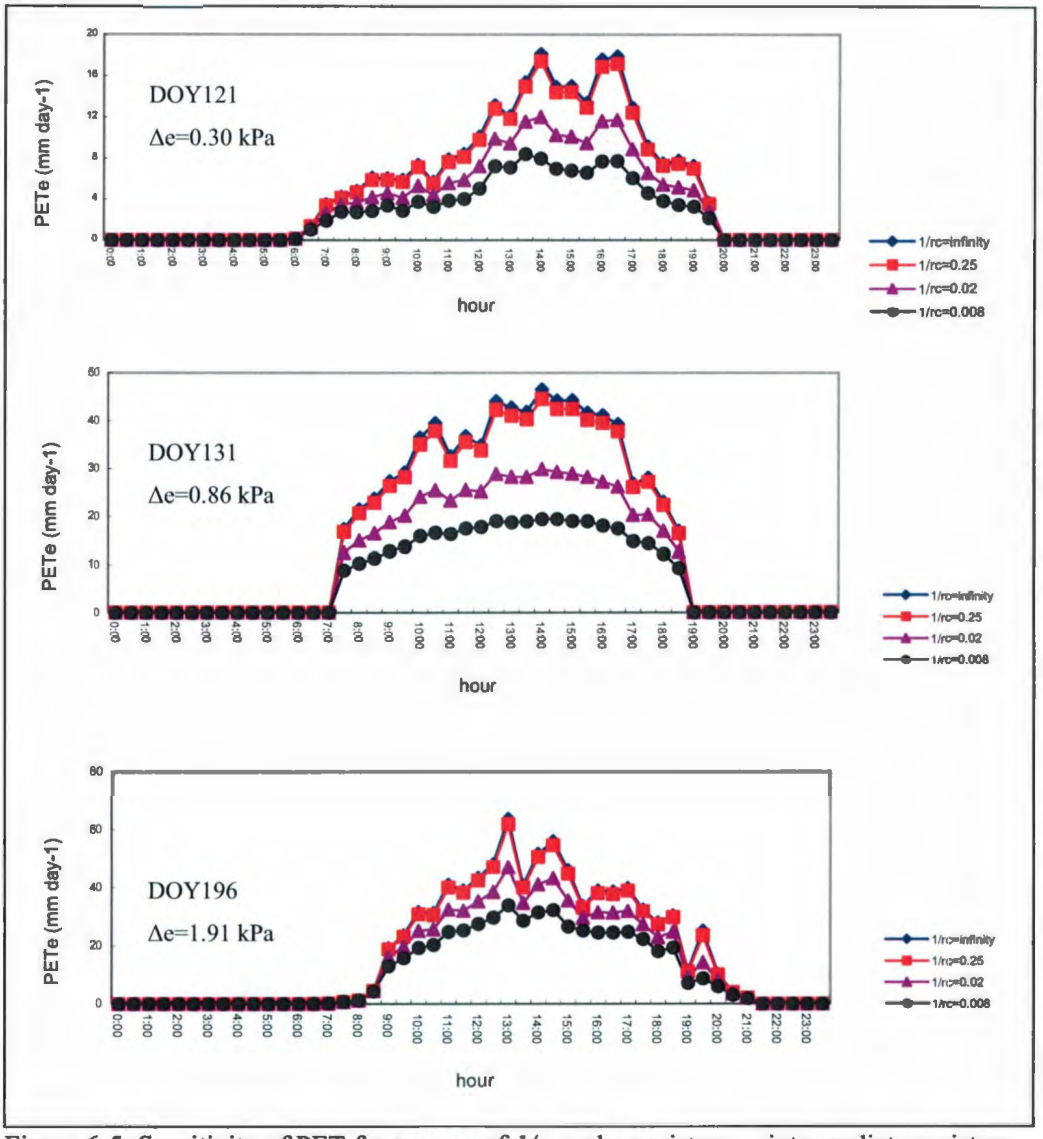

Figure 6-5: Sensitivity of PET for a range of $1/r_c$ under moisture, intermediate moisture, and dry condition in DOY 121, 131, 196, 2007.

6.2.4. Interaction Effects of Stomatal Resistance and Aerodynamic Resistance on Potential Evapotranspiration

Because of the potential for partial uncoupling of transpiration from control by stomata, an analysis of variation in r_c alone may not be a reliable indicator of variations in PET. The extent to which stomatal movements control evapotranspiration is highly correlated with r_a surrounding each leaf and the entire canopy. Meinzer *et al.* (1997) presented that stomatal control of transpiration was strong only when $1/r_a$ was high in relation to $1/r_c$. Regardless of its absolute value, if the magnitude of $1/r_a$ was similar to or less than that of $1/r_c$, transpiration from the leaves would promote local humidification of the air surrounding the leaves, uncoupling the vapor pressure at the leaf surface.

Interaction effects of r_c and r_a on PET will be explored in the following section. The behaviors of the Penman-Monteith formula for different stability conditions are discussed for a range of Δe and r_c conditions.

Figure 6-6 shows the results for the small moisture deficit case under different $1/r_c$ conditions. PET_e and PET_n are plotted versus net radiation ($K+L$). When $1/r_c=\infty$ (Figure 6-6a), PET_e and PET_n are equal at K+L≈150 W m^{-2}, which is under neutral condition. As K+L increases beyond 150 W m^{-2}, PET_e is greater than PET_n. Equation 6-1 shows that PET will increase as $1/r_a$ increases, when $1/r_a$ is comparable in magnitude to $1/r_c$ or much smaller. Therefore, when K+L beyond 150 W m^{-2}, $r_{ah}<r_{ah0}$, the surface layer becomes more and more unstable. The opposite behavior occurs as K+L decreases from 150 W m^{-2}, and produces an increasingly stable surface layer. The cases of large and intermediate moisture deficit have the same behavior as the small moisture deficit condition (Figure 6-7a and Figure 6-8a). The surface layer remains stable when PET_e <PET_n.

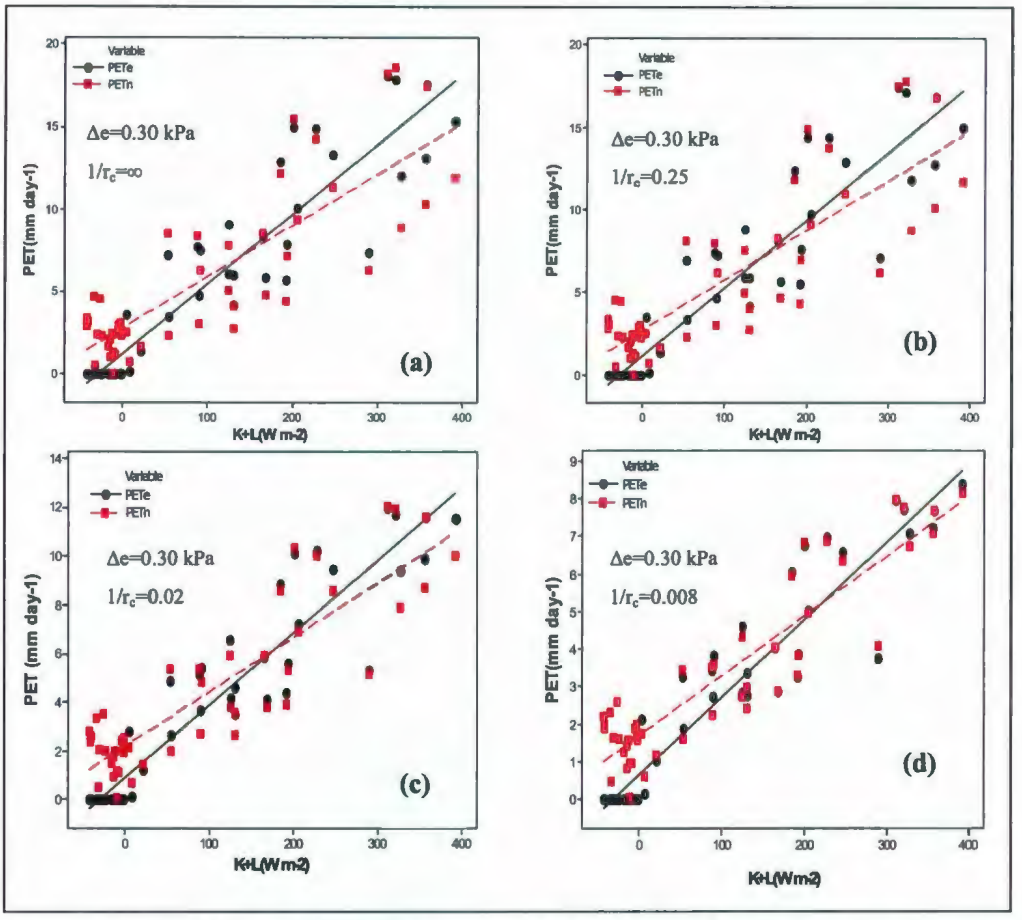

Figure 6-6: Sensitivity of PET for a range of $1/r_c$ under varying K+L surface layer for moist air case in DOY121, 2007.

Figures 6-6b-d show results for cases in which $1/r_c$ is not infinite. In each of these cases, for very small $K+L$, the surface layer is stable. The neutral condition occurs when PET_e and PET_n curves first cross as $K+L$ increases from the minimum value. Further increases in $K+L$ give $PET_e > PET_n$. For the cases of intermediate (Figure 6-7a-d) and large (Figure 6-8a-d) moisture deficits, the differences between PET_e and PET_n tend to be smaller in magnitude, as most of the time the surface layer is in a stable situation. For the case of the small moisture deficit, the magnitude of $K+L$ for the surface layer to reach the neutral condition increases as $1/r_c$ decreases from infinite to 0.008 m s^{-1}.

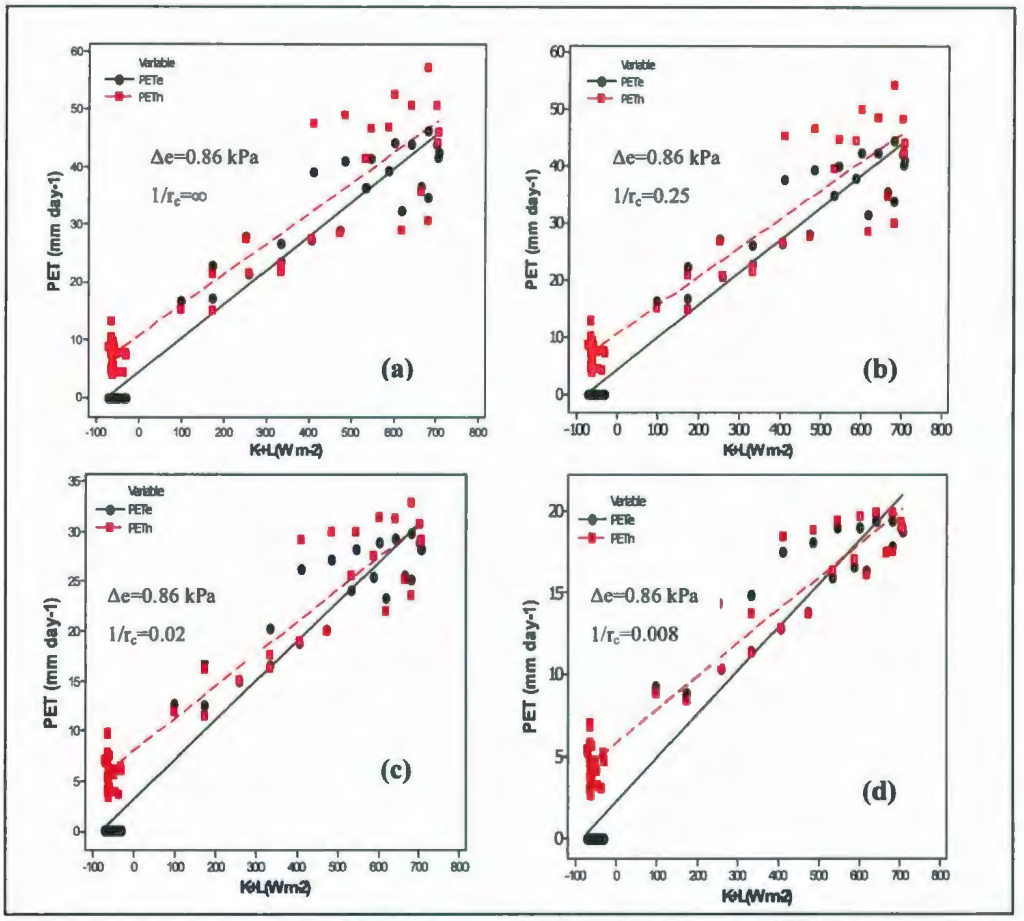

Figure 6-7: Same as Figure 6-6 but for intermediate moist air case in DOY 131, 2007.

Under intermediate moisture conditions, the surface layer retains stability until $1/r_c$=0.02 m s^{-1}, and $K+L$ is approximately equal to 700W m^{-2}. The same behavior can be found under the dry air surface layer. Over most of the range of $1/r_c$, Δe and $K+L$, the absolute differences between PET_e and PET_n remain small, in part due to r_c constraints on PET.

Grace *et al.* (1980) pointed out that the balance between the values of aerodynamic and stomatal resistance could determine the model for the control of transpiration. If r_a was comparable to or larger than r_c, PET would increase as r_a decreased. However, under

extremely unstable conditions, $1/r_a >> 1/r_c$, the surface evapotranspiration was limited by r_c, changes in r_a would have little effect on PET rate.

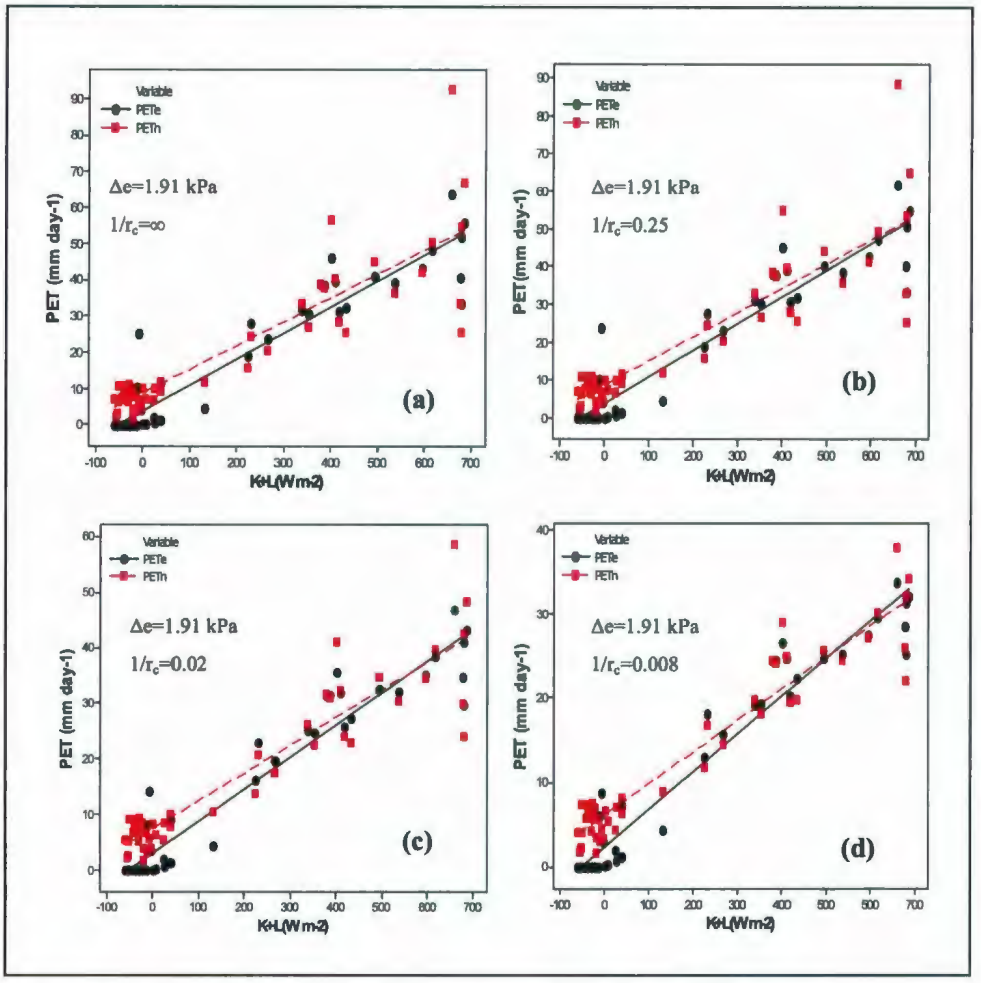

Figure 6-8: Same as Figure 6-6 but for dry air case in DOY 196, 2007.

6.3. Summary

The Panmen-Monteith combination method is widely used to estimate evapotranspiration. The original Penman-Monteith method assumes that the surface layer is neutrally stratified. In this study, both neutral and un-neutral surface layers are considered. The

peak of PET over the Marmot Creek basin occurs in July, which can be attributed to the dry weather conditions. October has the lowest PET rate, which is equal to half the peak value in July, due to the fact that less solar radiation is received by the surface.

r_a does not show significant effects on PET. The balance between the values of r_a and r_c can determine which resistance has the main control of evapotranspiration. Under extremely unstable conditions, with r_a less than r_c, the surface evapotranspiration is limited by r_c, and PET does not increase as r_a decreases.

In spite of the limitations of the Penman-Monteith approach, it definitely has had numerous successful applications in the field of hydrology to estimate PET. PET estimated from this study, will be applied to the TOPMODEL simulation in the next chapter.

Chapter 7

Hydrological Modeling by TOPMODEL

TOPMODEL, a physically-based model, has the concept that the variable source area in a basin is the dominant runoff-generating mechanism in the rainfall-runoff process. The variable-source-area concept emphasizes that runoff occurs where infiltration rates are greater than precipitation rates. It implies that the flow occurs due to overland flow generated when the soil is fully saturated to the surface and subsurface flow returns to the surface in the saturated areas. Overland flow for a given time step in TOPMODEL is calculated from the areal extent of the saturated land-surface areas and the precipitation intensity. Subsurface flow is computed as a function of the maximum subsurface-flow rate (determined by topographic and soils characteristics) and the watershed average depth to the water table. The watershed average depth to the water table is computed by water balance; that is, by tracking input (precipitation) and output (overland flow, subsurface flow, and evapotranspiration) (Wolock, 1993).

The predominant factors, determining the formation of runoff in TOPMODEL, are represented by the topography of the basin and a negative exponential law linking the

transmissivity of the soil with the vertical distance from the ground level (Franchini *et al.*, 1996). Topography, the three-dimensional configuration of gravitational effects on drainage, plays an important role in hydrologic modeling. $\ln(a/\tan\beta)$ in frequency distributions are used in TOPMODEL simulation to estimate the average moisture deficit for the catchment. Large values of $\ln(a/\tan\beta)$ indicate the locations within a watershed most likely to be saturated and produce overland flow. These locations are topographically convergent and have gentle slopes and low transmissivity. They drain a significant upslope area of the watershed and have limited capacity to conduct water from the drained area in a downslope direction.

In this study, the Genetic Algorithm (GA) is combined with TOPMODEL to calibrate the parameters by comparing the results of repeated simulation with the observations of streamflow in order to get the best fit runoff hydrograph. The simulations in TOPMODEL ultimately determine the runoff at the catchment outlet and the soil moisture deficit at each location within the Marmot Creek basin. TOPMODEL version 95 is applied to do the simulations using a single catchment model which assumes that the soil profile is homogeneous through the catchment. It implies a spatially constant soil transmissivity value.

7.1. TOPMODEL

TOPMODEL simulates the movement of water through a watershed from the time that it enters the watershed as precipitation to the time that it exits the watershed as streamflow. Figure 7-1 shows the main paths that water follows during this sequence. There are several components of TOPMODEL that describe different aspects of watershed

hydrology. These components in the following sections explain streamflow generation, evapotranspiration generation, soil profile, and other important characteristics of TOPMODEL.

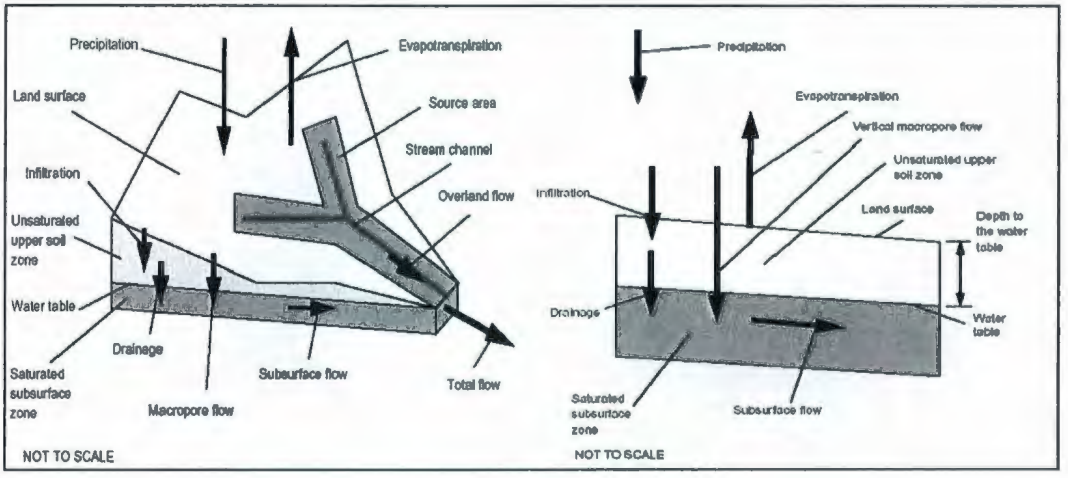

Figure 7-1: Water fluxes in TOPMODEL (Wolock, 1993).

7.1.1. Streamflow Generation

The streamflow equations, adopted in TOPMODEL, are derived base on Darcy's law, the continuity equation, and the assumption that the saturated hydraulic conductivity decreases exponentially as depth below the land surface increases (Wolock, 1995). Streamflow is the sum of subsurface flow and overland flow from saturated contributing areas:

$$q_{total} = q_{subsurface} + q_{overland} \qquad \text{Equation 7-1}$$

where q_{total} (m h^{-1}) is the total streamflow per unit area, $q_{overland}$ (m h^{-1}) is the saturation overland flow per unit area, and $q_{subsurface}$ (m h^{-1}) is the subsurface flow per unit area.

Surface flow is generated when precipitation falls on a saturated area and from return flow, so:

$$q_{overland} = q_{direct} + q_{return}$$ Equation 7-2

where q_{direct} (m h^{-1}) is direct precipitation on saturated areas, and q_{return} (m h^{-1}) is the return flow. Equations 7-1 and 7-2 can be combined to give:

$$q_{total} = q_{direct} + q_{return} + q_{subsurface}$$ Equation 7-3

The starting points for deriving expression to compute q_{direct}, q_{return} and $q_{subsurface}$ are the continuity equation at some location i in the watershed and Darcy's Law. Assuming steady-state conditions with a spatially uniform recharge rate (R) to the water table, continuity gives:

Inflow to location i = Outflow from location i,or

$$A_i R = T_i \tan \beta_i C_i$$ Equation 7-4

where A_i (m^2) is the upslope surface area from i that drains past the location, T_i (m^2 h^{-1}) is the transmissivity of the saturated thickness at i, and C_i (m) is the contour width at i traversed by subsurface flow at the location.

The transmissivity of the saturated thickness at i is equal to the soil depth multiplied by the soil hydraulic conductivity. It is assumed that saturated hydraulic conductivity [$K_{(z)}$] of the soil decreases with soil depth exponentially, a situation often observed as:

$$K_{(z)} = K_0 e^{-fz}$$ Equation 7-5

where K_0 (m h^{-1}) is the hydraulic conductivity at the soil surface, and f (m^{-1}) is a parameter that governs the rate of decrease of K with depth. Determine the transmissivity

of a saturated zone of a given thickness Equation 7-5 is integrated from z (the depth to the water table) to D (the total soil depth) to obtain T_i as:

$$T_i = \frac{K_0}{f}(e^{-fz} - e^{-fD}) \qquad \text{Equation 7-6}$$

The term e^{-fD} is generally much smaller than the term e^{-fz}, so Equation 7-6 can be simplified:

$$T_i = \frac{K_0}{f} e^{-fz} \qquad \text{Equation 7-7}$$

TOPMODEL does water-balance accounting by keeping track of the saturation deficit (s). s (m) is the amount of water that one would have to add to the soil at a given point to bring the water table to the surface. To implement computations in term of s, z is replaced by s/ø, where ø (fraction) is the porosity of the soil. Substituting for z in Equation 7-7 gives:

$$T_i = \frac{K_0}{f} e^{-f\frac{s}{\phi}} \qquad \text{Equation 7-8}$$

To make thighs "neater", $f/ø$ is replaced with $1/m$, and Equation 7-8 is substituted into Equation 7-4 to get:

$$A_i R = (\frac{K_0}{f} e^{-\frac{s}{m}} \tan\beta)_i C_i \qquad \text{Equation 7-9}$$

Dividing by C_i, letting $a_i = A_i/C_i$, $T_0 = K_0/f$, and solving for s:

$$s = m\ln(\frac{R}{T_0}) - m\ln(\frac{a}{\tan\beta}) \qquad \text{Equation 7-10}$$

To solve for the catchment-average saturation deficit ($\bar{s}$), Equation 7-10 is integrated over the entire watershed area to obtain $\bar{s}$, here R and T_0 are assumed to keep constant over the catchment:

$$\bar{s} = -m \ln(\frac{R}{T_0}) - m\lambda \qquad \text{Equation 7-11}$$

where λ is the mean ln(a/tanβ) for the catchment. Combining Equation 7-10 and 7-11 gives:

$$s_i = \bar{s} + m[\lambda - \ln(\frac{a}{\tan\beta})_x] \qquad \text{Equation 7-12}$$

Equation 7-12 states that s at any location i is determined by $\bar{s}$, and the difference between λ and the value of ln(a/tanβ) at location i. Equation 7-12 is used to determine q_{direct} and q_{return}. Any location i in the watershed where $s_i \leq 0$ is saturated, and has the potential to produce saturation overland flow. Any location where $s_i<0$ produces return flow.

The value of q_{direct} is computed by summing the products of the saturated areas, a_i, multiplied by the precipitation intensity, p, and dividing by the watershed area, A, as:

$$q_{direct} = \frac{\sum_A a_i p}{A}, \; s_i \leq 0 \qquad \text{Equation 7-13}$$

The value of q_{return} is computed by summing the products of the saturated areas multiplied by the absolute value of the negatively valued saturation deficits, as:

$$q_{return} = \frac{\sum_A a_i |s_i|}{A}, \; s_i < 0 \qquad \text{Equation 7-14}$$

Therefore, the overland flow can be described as:

$$q_{overland} = \frac{\sum_A a_i p}{A} + \frac{\sum_A a_i |s_i|}{A} = \frac{\sum_A a_i p + \sum_A a_i |s_i|}{A} \qquad \text{Equation 7-15}$$

Subsurface flow, $q_{subsurface}$, is computed by combining Darcy's Law for saturated subsurface flux, and integrating it over the catchment area and dividing the result by the catchment area yields:

$$q_{subsurface} = T_0 e^{-\lambda} e^{-\frac{\bar{s}}{m}} \qquad \text{Equation 7-16}$$

Now, the total streamflow including the subsurface and overland flow can be presented as:

$$q_{total} = \frac{\sum_A a_i p + \sum_A a_i |s_i|}{A} + T_0 e^{-\lambda} e^{-\frac{\bar{s}}{m}} \qquad \text{Equation 7-17}$$

7.1.2. Soil Profile in TOPMODEL

TOPMODEL operates local root zone, saturated and unsaturated zone stores within each ln(a/tanβ) increment, as shown in Figure 7-2. Evapotranspiration is taken from the root zone storage (SRZ). However, when SRZ exceeds the field capacity of the soil, the excess moisture will contribute to the unsaturated zone moisture storage (SUZ). When s_i >0, the soil is partly unsaturated, unsaturated zone calculations are made for each ln(a/tanβ) increment. The calculations use two storage elements, SUZ and SRZ, representing storages above and below some field capacity value at which vertical drainage starts to become significant. Storage subject to drainage is represented by SUZ (i) for the *ith* increment of ln(a/tanβ). When SUZ>0, the vertical flow through the unsaturated zone in TOPMODEL, q_{vi}, can be calculated as:

$$q_{vi} = \frac{SUZ}{s_i t_d}$$ Equation 7-18

where t_d (h m^{-1}) represents an average residence time per unit of saturation deficit. The total recharge rate, Q_v (m h^{-1}), to the saturated zone from the unsaturated zone over the entire watershed can be represented as:

$$Q_v = \sum_{i=1}^{n} q_{vi} A_i$$ Equation 7-19

where n is the total number of index values. Once Q_v enters the saturated zone to reduce $\bar{s}$, a water balance calculation for $\bar{s}$ produces a new end-of-time step value that is used to calculated new values of s_i at the start of the next time step.

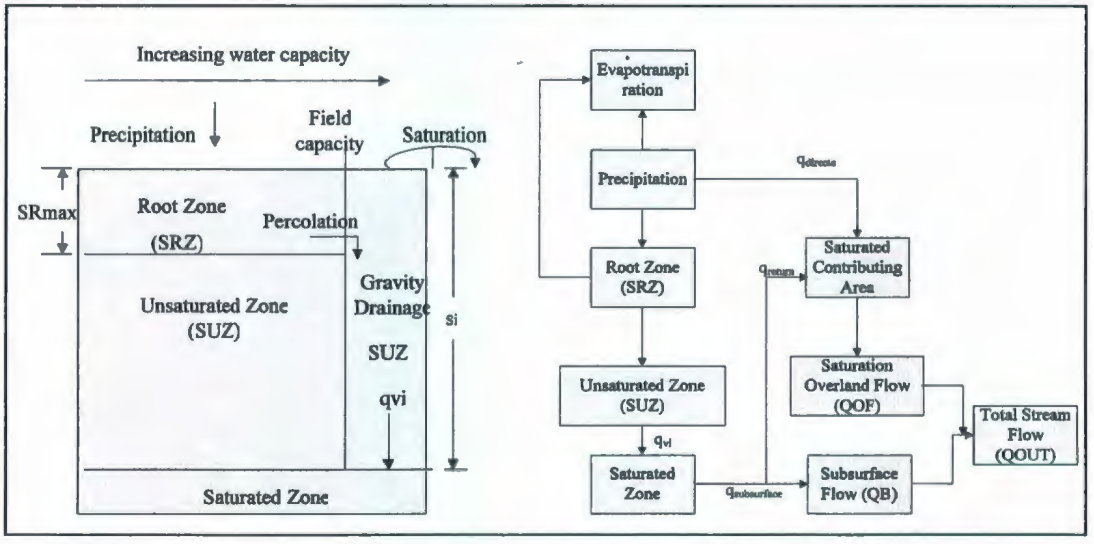

Figure 7-2: Schematic diagram of local soil water stores in TOPMODEL.

7.1.3. Evapotranspiration Generation

Evapotranspiration (ET) draws water from the root zone moisture store. The maximum value of storage in this compartment is SRmax. ET is a function of both PET and actual amount of water that is available. ET can be presented as:

$$ET = PET \times \left(1 - \frac{SRZ}{SR\max}\right)$$ Equation 7-20

PET_e is employed to be as an input file to the TOPMODEL simulation. Normally, no water reaches the unsaturated zone store unless ET is satisfied from the root zone store.

7.1.4. Topographic Index Generation

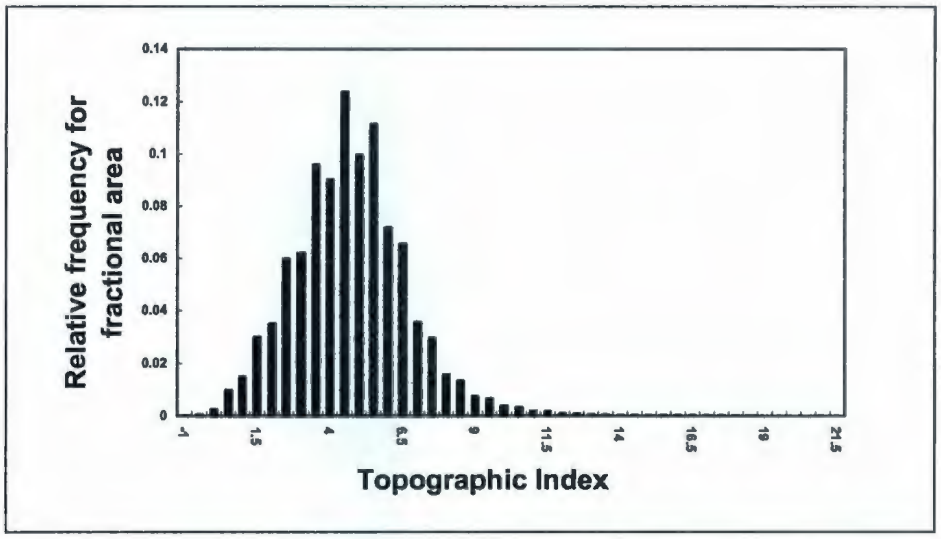

Figure 7-3: Frequency distribution of ln(a/tanβ) in the Marmot Creek basin.

In TOPMODEL, one simplifying assumption is that all locations in the watershed with the same value of ln(a/tanβ) are hydrologically similar in their response. This assumption allows the aggregation of the ln(a/tanβ) distribution from a spatially explicit description of the watershed into one of intervals in ln(a/tanβ).The model equations do not change, but the calculations are performed using ln(a/tanβ) values of frequency-distribution interval midpoints instead of the individual spatially distributed values. By knowing the relative frequency, that is, the proportion of watershed area corresponding to each interval midpoint, total watershed values for the model variables can be calculated.

In Chapter 4, spatial distributions of $\ln(a/\tan\beta)$ are calculated by D8 and D∞ with 1- and 90-meter resolution DEMs. In this study, the frequency distribution of $\ln(a/\tan\beta)$ produced by D8 working in 1-meter resolution DEM, to do primal model simulation (Figure 7-3).

7.1.5. Channel Routing

In TOPMODEL, Clark's method (1945), which is regarded as a time-area routing method, is adopted to route water flows through the channel system to stream outlet. In this method, the travel time in the catchment is divided into equal intervals. At each time interval, it is assumed that the area within the catchment boundaries and the specific distance increment will contribute to the flow at the catchment outlet. The partial flow, at the catchment outlet from each sub-area, is equal to the product of the rainfall excess produced times the area of the contributing portion of the catchment. Summing the partial flows of all contributing areas at each time step gives the total flow at the catchment outlet for each time step in the hydrograph (Krauth, 1999).

7.2. TOPMODEL Operation

7.2.1. Model Parameters

This version of TOPMODEL contains seven parameters which are listed in Table 7-1 with descriptions and their corresponding ranges. These parameters are the surface transmissivity, T_0, the transmissivity decay parameter, SZM, the time delay per unit depth of deficit, t_D, the channel and routing velocities, CHV and RV, the maximum allowable root zone storage, SRmax, and the initial moisture deficit in the root zone, SR_0.

Table 7-1: Model parameters involved in TOPMODEL.

Parameter	Name in theory	Description	Range
SZM[m]	m	Transmissivity decay parameter	0.005-0.06
T0 [m^2h^{-1}]	$\ln(T_0)$	Effective lateral saturated transmissivity	0.1-8
TD [$m\ h^{-1}$]	t_d	Unsaturated zone time delay	0.1-500
CHV [$m\ h^{-1}$]	CHV	Channel velocity	100-10000
RV [$m^{-2}\ h^{-1}$]	RV	Routing velocity	100-10000
SRMAX [m]	SRmax	Maximum allowable root zone storage	0.005-0.3
SR0[m]	SR0	Initial root zone deficit	0.0-0.3

7.2.2. Model Variables

A list of names and definitions of the corresponding variables involved in TOPMODEL Fortran source code are given in Table 7-2.

Table 7-2: Corresponding variable names in TOPMODEL Fortran code and in this thesis.

Name in theory	Variable	Description
$\bar{s}$ (m)	SBAR	Average moisture deficit
λ	TL	Average topographic index value
$\ln(a/\tan\beta)$	ST	Local topographic index value
s (m)	SD	Local moisture deficit
A (m^2)	AC	Fractional area of catchment
P ($m\ h^{-1}$)	P	Precipitation
$q_{overland}$ ($m\ h^{-1}$)	QOF	Total flow from saturation excess
$q_{subsurface}$ ($m\ h^{-1}$)	QB	Flow from unsaturated zone
q_{total} ($m\ h^{-1}$)	QOUT	Total flow at current time step
q_{vl} ($m\ h^{-1}$)	UZ	Vertical flux through the unsaturated zone
Q_v ($m\ h^{-1}$)	QUZ	Recharge rate to the saturated zone
ET ($m\ h^{-1}$)	EA	Evapotranspiration
PET ($m\ h^{-1}$)	EP	Potential evapotranspiration
SRZ (m)	SRZ	Moisture deficit in the root zone
SUZ (m)	SUZ	Moisture storage in unsaturated zone

7.2.3. Model Assumption

This version of TOPMODEL is underpinned by three assumptions (Beven, 1995): i) Dynamics of the saturated zone can be approximated by successive steady-state representations; ii) Hydraulic gradient of the saturated zone can be approximated by the local surface topographic slope, tanβ; groundwater table and saturated flow are parallel to the local surface slope; iii) Distribution of downslope transmissivity with depth is an exponential function of storage deficit or depth to the water table

7.2.4. Model Input-Output file

Three input files are required to implement TOPMODEL, namely, an input file which contains rainfall, PET, and observed streamflow data; a catchment data file which contains the frequency distribution of $\ln(a/\tan\beta)$ and its corresponding area fraction and distance-area data; and a run file which contains run and file information. The output file just contains the simulated streamflow data, and soil moisture deficit. The input and output files required in TOPMODEL are summarized in Table 7-3.

Table 7-3: TOPMODEL input and output files.

Input:	Time series of:	Precipitation
		PET
		Observed streamflow (for calibration)
	Frequency distributions of :	$\ln(a/\tan\beta)$
	Distance-Area data	
Output	Time series of:	Total streamflow
	Temporal and spatial distributions of:	Soil moisture deficit

7.2.5. Model Calibration---Genetic Algorithm

Before a hydrologic model can be executed, it is necessary to determine numerical values for each of the parameters. Calibration is a process of adjusting the parameter values to improve the agreement between the simulated and observed data. In this thesis, GA is combined with TOPMODEL to perform the identification of the optimal parameter set.

As one of the effective and powerful evolutionary algorithms, GA was originally proposed by John Holland (Holland, 1975) to represent a fairly abstract model of biological evolution. It has been successfully applied to various scientific and engineering problems, especially, to the very complex functions optimization (Goldberg, 1989). Based on the stochastic search, GA provides the highly approximate solutions, which could be further employed by a mathematical optimizing method (e.g. Newton method). The workflow of GA is shown in Figure 7-4.

In general, as shown in Figure 7-4, for a certain problem to optimize, GA first randomly initializes a set of search solutions within the search space, called population. Each random solution in population is called an individual. Second, GA selects several individuals as parents and evolves those parents, using genetic operator, to produce offspring. At the end, based on the fitness of offspring, GA selects the survival offspring to replace the parents and generate new population. This iteration is called as one generation. After a certain number of generations, the suitable individuals (solutions), who optimize the function, will survive. Based on the fitness of function evaluation, the best individual is selected as the optimal solution.

In TOPMODEL, seven parameters are calibrated for the streamflow simulation. GA is employed in this research to optimize these parameters. In order to combine GA with

TOPMODEL, these seven parameters are initialized in the program and represented by a real number vector with length seven, as an individual. Each item, in the individual vector, presents one parameter of TOPMODEL. The search space of designed GA is shown in Table 7-4.

The uniform mutation and arithmetic crossover are applied as the genetic operators. Each pair of parents has 0.5 probabilities to be mated using uniform mutation and 0.5 probabilities to be mated using arithmetic crossover. In the uniform mutation, another vector, with length seven are generated. The contents of the vector are uniform random values in the range of 10% of each search space. Adding this new vector to the vector of parent produces offspring. In the arithmetic crossover, offspring are produced by linear combination of two parents' vector. All individuals in the population are selected as parents to mate. After sorting the fitness of the new individuals together with the fitness of the old individuals, the best 100 (population size) individuals are chosen as the new population (Eshelman, 1990).

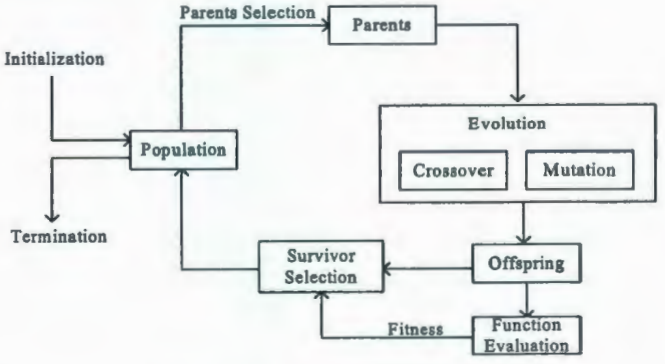

Figure 7-4: Flowchart of GA.

Table 7-4: The search space for the calibrated parameters in GA.

Vector Location	Presented Parameter	Search Space
1	SZM	0.005-0.06
2	T0	0.1-8
3	SR0	0.0-0.3
4	SRMAX	0.005-0.3
5	CHV	100-10000
6	TD	0.1-500
7	RV	100-10000

The fitness evaluation function (objective function) is designed as the sum of absolute difference between simulated streamflow and observed streamflow for every time step, which can be written as:

$$Fitness = \sum_{i=1}^{n} \left| QOBS_i - QSIM_i \right| \qquad \text{Equation 7-21}$$

The program is terminated either the number of generation reaches 500 or the fitness evaluation function return the simulated streamflow completely the same as the observed streamflow. The original structure of TOPMODEL, and the model combined with GA are shown in Figure 7-5 and Figure 7-6.

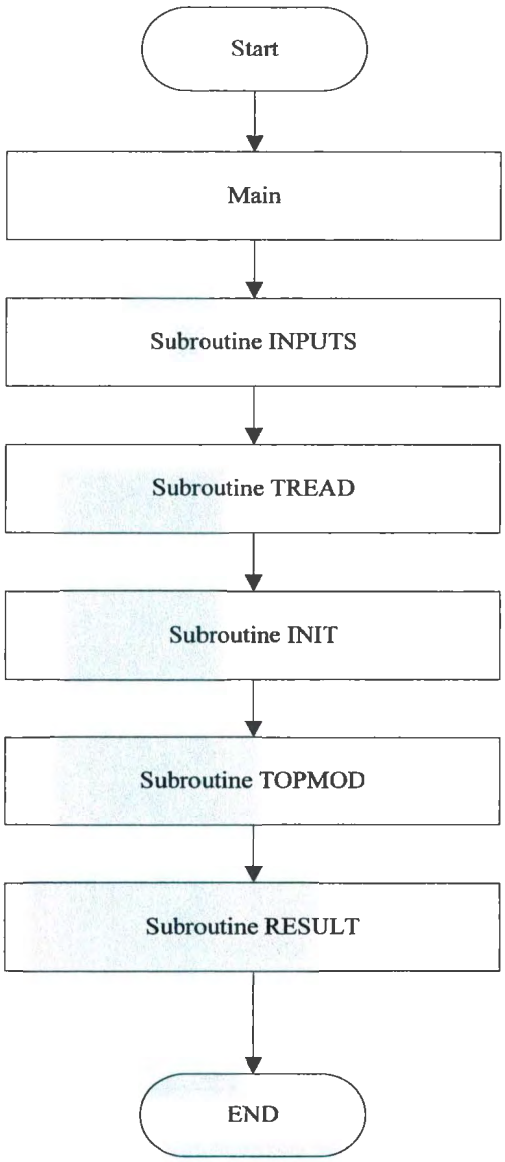

Figure 7-5: Flow chart for the original TOPMODEL without GA.

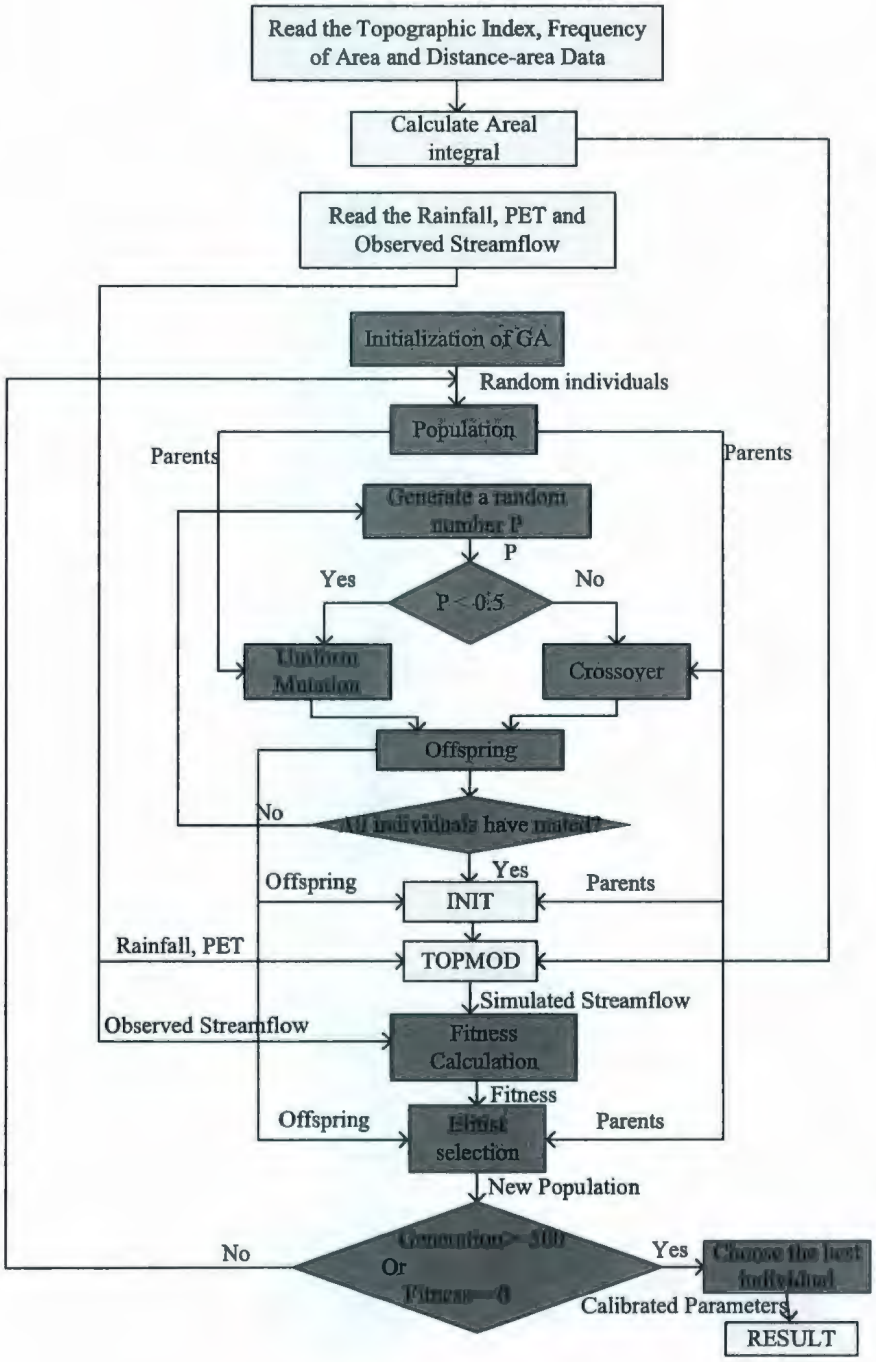

Figure 7-6: Flow chart for TOPMODEL with GA.

7.2.6. Model structure

This version of TOPMODEL allows single sub-catchment calculations with single rainfall and PET input to the whole catchment. The FORTRAN code for TOPMODEL is structured in a modular format.

Subroutine INPUTS in the original TOPMODEL is used to read in rainfall, PET, and observed streamflow with the number of time steps, NSTEP. Subroutine TREAD in the original TOPMODEL is utilized to read in $\ln(a/\tan\beta)$ and its corresponding frequency area in order to calculate λ. The second function in TREAD is to read the distance-area data from the catchment file. The functions did in subroutine INPUTS and TREAD are implemented in the main routine in revised TOPMOEL which is combined with GA. These two subroutines did not exist in our model.

Both original and revised TOPMODEL contain subroutines INIT and TOPMOD. The first function of the subroutine INIT is to read in the parameter values from GA and to calculate the subsurface flow when soil is fully saturated, SZQ parameter is introduced. The second function of the subroutine INIT is to convert the distance-area form to a time-area histogram ordinates, and to calculate the cumulative fractional areas and incremental fractional areas accompany the travel time increment. The cumulative fractional areas are the percentage of the catchment that contributes to the flow at the catchment out for each time travel increment. The incremental fractional areas are the average areas between two consecutive divisions of area. The third function of subroutine INIT is to initialize the stores for each $\ln(a/\tan\beta)$ increment. The unsaturated zone moisture storage, SUZ, is initially set equal to 0 m. The root zone moisture deficit, SRZ, is set equal to SR0. The average moisture deficit, $\bar{s}$, is calculated using Equation 7-11. The last function of INIT

is to reinitialize the simulated streamflow and to calculate the moisture balance in the catchment at the beginning of the storm event. For each time increment, the simulated streamflow value is initialized as the sum of initial streamflow at the catchment outlet and the streamflow at the current time step.

The subroutine TOPMOD computes evapotranspiration, soil moisture balance, changes in the saturation deficit, overland flow, subsurface flow and the channel routing. The calculations of evapotransration, soil moisture balance, changes in the saturation deficit and overland flow are made for areal subdivisions based on $\ln(a/\tan\beta)$ subdivisions, NAC. The calculations of subsurface flow, total stream flow and average soil moisture deficit are made under the loop controlled by the time step, NSTEP. Figure 7-7 shows the process begin by starting a loop on the time steps for the observed hydrograph and precipitation values. The local moisture deficit in the unsaturated zone, SD, is calculated by the Equation 7-12 for each $\ln(a/\tan\beta)$. If SD less than zero, it will set to be zero. The root zone moisture deficit, SRZ, is determined by the initial root zone moisture deficit, SR0, and the precipitation. If SRZ is less than zero, the root zone is saturated. The excess of SRZ is transferred to the unsaturated zone and becomes the moisture storage in the unsaturated zone, and then SRZ will set equal to zero. SRZ also has relation with the evapotranspiration. If evapotranspiration is present at the current time step, the moisture loss from the root zone through evapotranspiration would be added to SRZ. When SUZ greater than SD, the amount of moisture in the unsaturated zone is excess what is required to satisfy the local moisture deficit there. The depth of saturation excess, EX, is

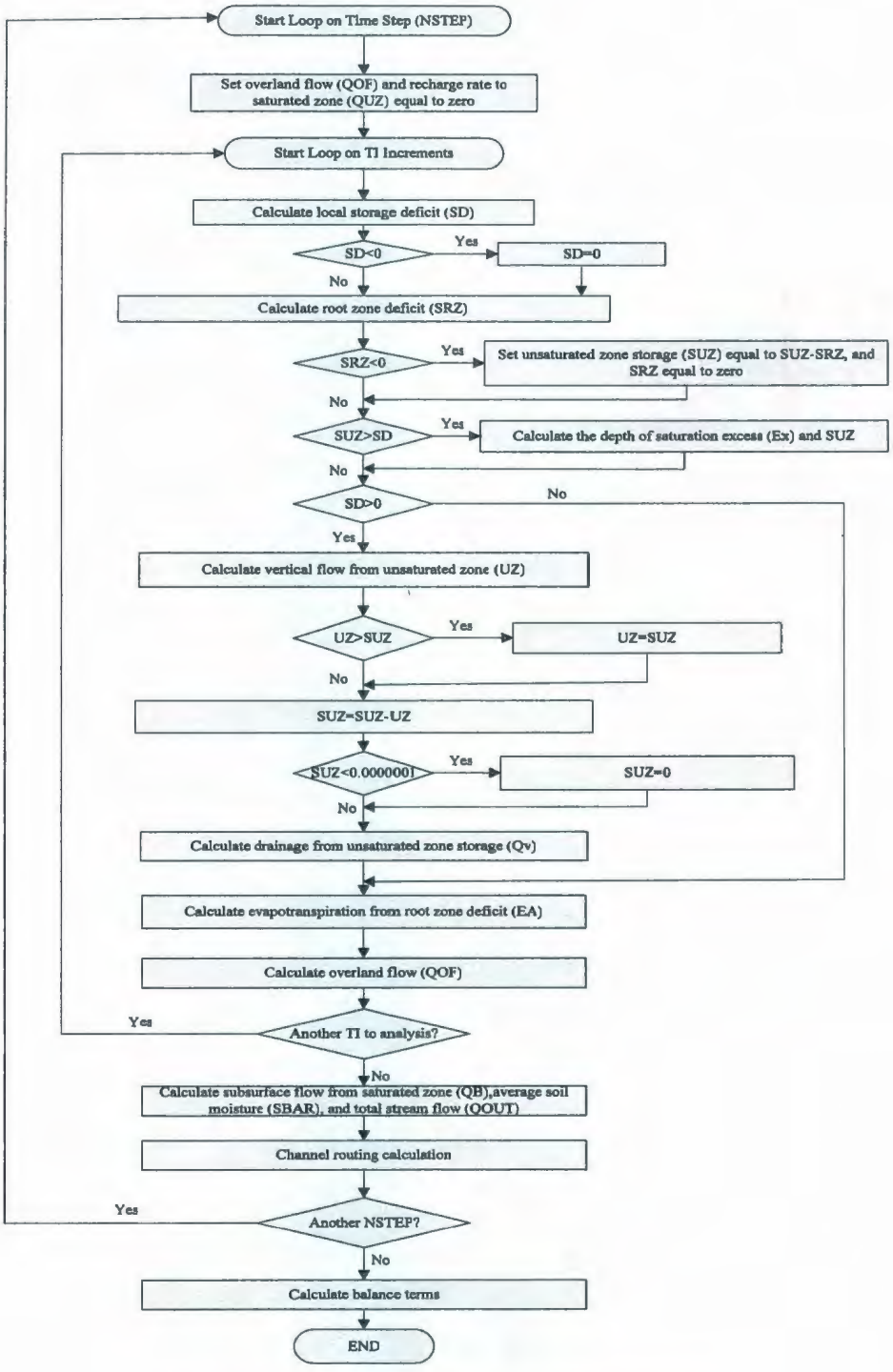

Figure 7-7: Flow chart for the TOPMOD subroutine.

equal to the difference between SUZ and SD. In this situation, EX would become overland flow, QOF. The total recharge rate, Qv, from unsaturated zone to saturated zone occurs when SD greater than zero. Under this condition, SUZ should minus the amount of moisture which has gone through to the saturated zone. The subsurface flow, QB, and total flow, QOUT are calculated at the end of the current time step using Equation 7-16 and 7-17.

The subroutine RESULT is utilized to read out the stream flow and moisture stores which are simulated above.

7.2.7. Model Evaluation

The efficiency of the model is evaluated by the coefficient of efficiency (EFF), which was proposed by Nash and Sutcliffe (1970). EFF can be calculated as:

$$EFF = 1 - \frac{\sum (QOBS_i - QSIM_i)^2}{\sum (QOBS_i - QOBS_m)^2} \qquad \text{Equation 7-22}$$

where $QOBS_i$ is the observed streamflow, $QSIM_i$ is the simulated streamflow, and $QOBS_m$ is the mean of the observed streamflow.

7.3. Results and Discussions

The calibration period of 20th August to 31st October in 2007, which was free of snow, is chosen to include only low flows. Figure 7-8 shows the hydrological record for the period chosen. The total amounts of observed rainfall (P), PET and discharge (Q) for this period were 0.827 m, 0.209 m and 0.0472 m respectively. During the validation period from August 10th to September 10th, 2006, total rainfall was equal to 0.375 m.

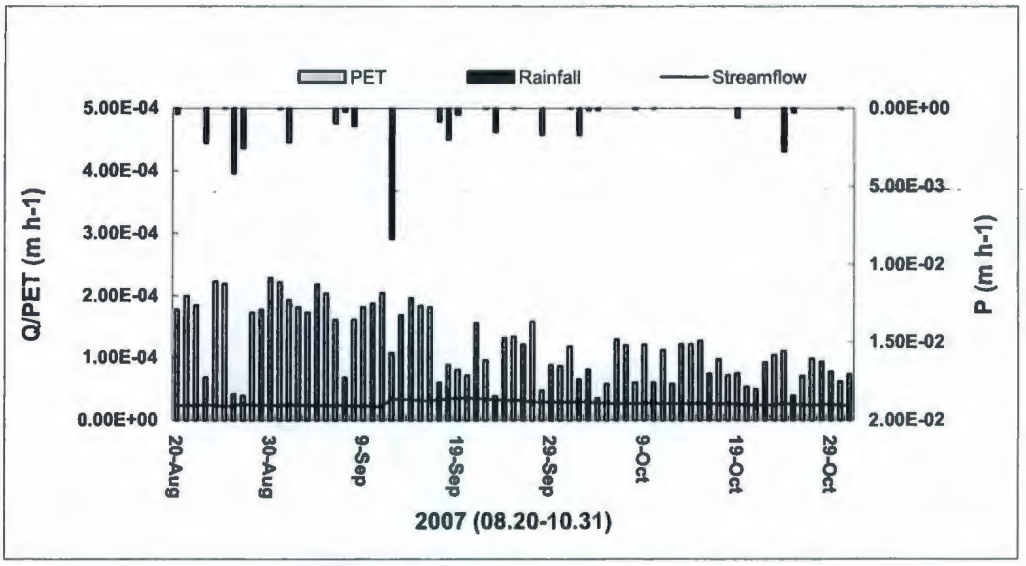

Figure 7-8: P, PET and Q of the Marmot Creek basin used as the calibration period in the model run.

In the case of conceptual rainfall-runoff models, periods of 72 days may be too short for a reliable assessment of parameters. Sorooshian *et al.* (1983) suggested that a period of at least one year was necessary for calibrated conceptual models in order to activate all model components during calibration. However, Iorgulescu and Jordan (1994) argued that the available information on the catchment studied could guarantee an adequate estimation of parameters, when using a model with some physical basis, even if calibration periods remained relatively short. As the stream flow in the Marmot Creek basin is not measured from November to April, the only available simulation periods are from May to October. However, nearly 70% of the streamflow results from the melting of snow from spring to midsummer, that period should exclude. Therefore, the period from 20th August- 31st October 2007 is the best time can be chosen.

7.3.1. Calibration Results

Following the calibration procedures, the best parameter sets for the Marmot Creek basin during the calibration period are shown in Table 7-5. All parameter values are within the estimated range.

Table 7-5: Calibrated parameters of TOPMODEL for the Marmot Creek basin during the period of 20th August-31st October 2007.

Parameters	SZM (m)	T0 (m^2h^{-1})	SR0 (m)	SRMAX (m)	CHV ($m\ h^{-1}$)	RV ($m^{-2}h^{-1}$)	Td ($m\ h^{-1}$)
Marmot Creek	0.0464	0.294	0.00150	0.00587	371.528	449.808	382.240

The results of runoff simulation are given in Figure 7-9. EFF is equal to 0.611. The runoff simulation in this snow free period is reasonably good as this version of TOPMODEL does not contain the snow component. Simulated runoff, after the high rainfall at the middle of September, is underestimated, perhaps because of the rough estimate of PET. As PET plays a major role in the watershed water balance, it is feared that imperfect estimates could either impede the calibration of watershed model parameters or modify their optimal values, and have a detrimental influence on model simulation. The simulated runoff following the extremely dry October is fairly matched with the observed data. The simulated streamflow in 2007 remains at low levels during the entire simulation period and no sharp peaks occur. The data presented in Table 7-6 shows that the total simulated runoff is only 0.0009 m higher than the measured runoff. Simulated runoff and evapotranspiration represent 5.82% and 25.74% of the measured precipitation, respectively. This may be caused by the uncertainties involved in the input data in the areal estimates of precipitation because of the mountainous character of the catchment. It is probable that the measured precipitation is overestimated to some extent,

which resultes in the difference of 68.44% in the water balance. In the Marmot Creek basin 60% of the catchment is needle-leaf forest, therefore, most of the precipitation would be intercepted by the trees. Only a small amount of the water would arrive on the ground to generate the streamflow.

Table 7-6: Main water balance components-model inputs and outputs for simulation.

Measured Runoff(m)	Simulated runoff (m)	Subsurface flow(m)	Evapotranspiration (m)	Input precipitation (mm)
0.0472	0.0481	0.0408	0.21293	0.827

The contribution of the subsurface flow to the total simulated flow in the period of 20th August to 31st October 2007 was 84.9%. The soils in the Marmot Creek basin are porous and, when not frozen, allow most of the precipitation to enter the soil. Wallis (1978) and Sklash (1978) showed that most of the streamflow in the Marmot Creek basin was derived from the groundwater. Numerical simulation conducted by Freeze (1972) indicated that subsurface storm-flow (including return flow) could be significant only under specific soil and topographic conditions. Iorgulescu and Jordan (1994) suggested that the dominant runoff-generating mechanisms computed by TOPMODEL were different in each catchment. These differences correspond to the knowledge of the basin reaction.

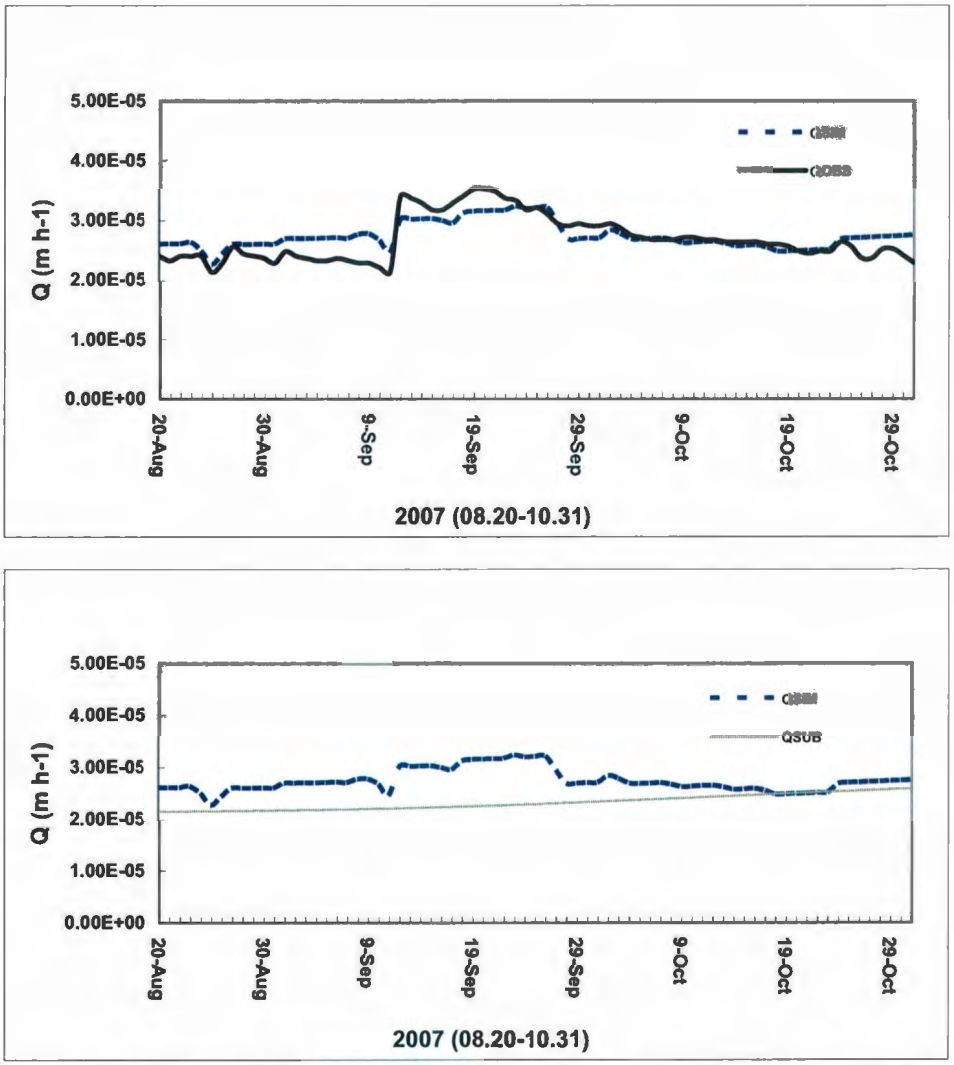

Figure 7-9: Results of daily model calibration from August to October 2007 for the Marmot Creek basin. QSIM is the simulated runoff, QOBS is the observed runoff, QSUB is the subsurface flow simulated by TOPMODEL.

7.3.2. Validation Results

During the validation simulation with the period of 10th August-10th September 2006, the parameters are kept constant to test the model potential in short term runoff simulations.

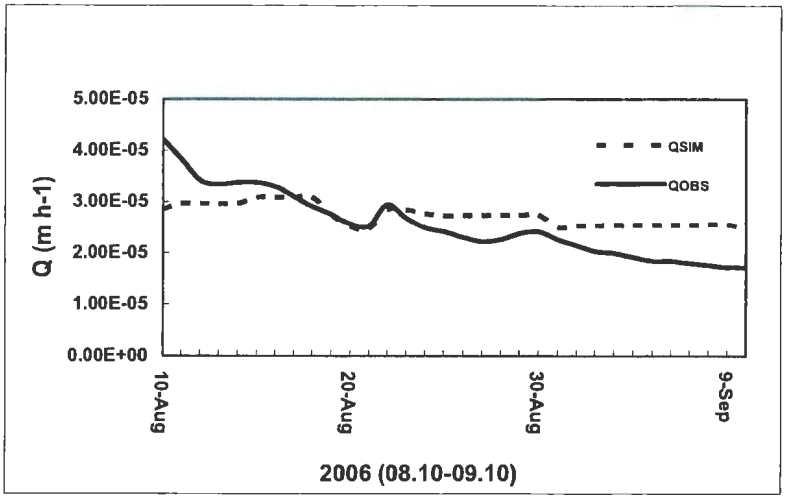

Figure 7-10: Results of daily model validation from August to September 2006 for the Marmot Creek basin. QSIM is the simulated runoff, QOBS is the observed runoff.

From Figure 7-10, it is obvious that the simulation in such a case do not fit the observed data equally well over the entire period of simulation, and EFF decreases to only 0.332 for the Marmot Creek basin. The total simulated streamflow (0.0196 m) is 0.00137 m less than the observed streamflow (0.0210 m). The underestimation of runoff may be caused by the rough estimation of PET. This underestimation may also be due to the fact that the soil variability is ignored. Soil properties vary with space, but they are assumed to be homogenous in this model.

7.3.3. Effects of Flow Directions and Grid Size on Runoff Generation

In this section, parameter sets are recalibrated using $\ln(a/\tan\beta)$ values determined by D8 with 1- and 90-meter resolution DEMs. The same parameters are applied again to D∞ in order to determine the effect of flow direction and grid size on streamflow generation. The results of model efficiencies and percentages of subsurface flow are shown in Table 7-7.

Table 7-7: Optimal parameter sets and results of daily streamflow simulation in the Marmot Creek basin.

	Flow	SZM (m)	T0 (m^2h^{-1})	SR0 (m)	SRMAX (m)	CHV ($m\ h^{-1}$)	RV ($m^{-2}h^{-1}$)	Td (mh^{-1})	EFF	QSUB (%)
1	D8	0.046	0.29	0.0015	0.0059	371.53	449.81	382.24	0.611	84.91
	D∞	0.046	0.29	0.0015	0.0059	371.53	449.81	382.24	0.583	86.4
90	D8	0.060	1.18	0.00006	0.0060	1725.00	114.84	261.85	0.656	52.55
	D∞	0.060	1.18	0.00006	0.0060	1725.00	114.84	261.85	0.565	53.96

The difference between the percentages of subsurface flow, using D8 and D∞ in the same resolution DEM, suggests that the streamflow generation mechanism is influenced by the flow direction. When the parameters are fixed, model efficiencies using D8 are marginally better than those using D∞. However, no matter which flow direction algorithm is used, the model efficiencies are not significantly improved.

After parameter re-calibration in the 90-meter resolution DEM, the model efficiency using D8 is improved from 0.611 to 0.656, and the percentage of subsurface flow decreases from 84.91% to 52.55%. The parameter SZM increases from 0.0464 m to 0.0597 m. The parameter T0 increases from 0.294 m^2h^{-1} to 1.188 m^2h^{-1}. Wolock *et al.* (1995) indicated that it was difficult to determine what values were reasonable or realistic for parameter SZM in TOPMODEL, because they were extremely variable over space and difficult to meaningfully quantify. The soil lateral transmissivity in this study increases as the grid size of DEM increases. Similar results can be found in Wolock *et al.* (1995) and Franchini *et al.* (1996). Wolock *et al.* (1995) demonstrated that hydraulic conductivity increased as the grid size increased in the Sleepers River watershed. Franchini *et al.* (1996) explored the effects of grid sizes on runoff generation in the Real Collobrier water in France. They concluded that the hydraulic conductivity parameter

values also increased with an increase in grid size. They pointed out that the ln(a/tanβ) distribution was greatly affected by the size of the DEM resolution, and this dependence was reflected in the hydraulic conductivity parameter. The values of parameter SRMAX were close to each other with different grid sizes. Iorgulescu and Jordan (1994) explained that SRMAX was not sufficiently activated during the simulation periods when actual evapotranspiration was considered close to PET.

For the 1- and 90-meter resolution DEMs, the mean ln(a/tanβ) produced by D8 is greater than the ln(a/tanβ) value resulting from D∞ (see Table 7-7). Low resolution DEM has a larger mean ln(a/tanβ) value than the high resolution DEM. Wolock *et al.* (1995) pointed out that an increase in the mean ln(a/tanβ) value caused a decrease in the subsurface flow. Our study is consistent with this standpoint. The percentage of subsurface flow resulted from D8 is a little lower than that produced by D∞ for the same grid size DEM. The percentage of subsurface flow using small grid size DEM is much lower than that percentage using large grid size DEM for the same flow routing algorithm.

Even if the model efficiencies of the different DEM resolutions are nearly the same using optimal parameters, an appropriate resolution DEM still needs to be considered for the model simulation. Zhang and Montgomery (1994) studied the effects of DEM resolutions on two small steep watersheds (0.3 km^2 in Oregon and 1.2 km^2 in California). The authors concluded that it was unreasonable to use a 30-meter or 90-meter resolution DEM to model hillslope or streamflow generation processes in moderate to steep gradient topography without some calibration of the process model. Quinn *et al.* (1995) found that low resolution DEMs were unrepresentative of detailed catchment form, and high resolution DEMs would cause a huge increase in data and need more processing time.

Bruneau *et al.* (1995) suggested that a resolution higher than 50 m was appropriate to simulate the streamflow generation using TOPMODEL in a 12 km^2 watershed.

Marmot Creek basin is small mountain drainage; thus, the 1-meter resolution DEM is better than the 90-meter resolution DEM to simulate the steep topographic characteristics. However, the data sets are too huge to handle for a 1-meter grid size. The 90-meter resolution DEM is adopted to study the relationship between $\ln(a/\tan\beta)$ and s in the next section.

7.3.4. The Relationship between Topographic Index and Local Soil Moisture Deficit

The strong influence of surface topography on the characteristics of water flow in a drainage basin is a well known phenomenon. Topography can affect the location of zones of surface saturation and the distribution of soil water. A number of terrain indices have been developed for predicting the spatial distribution of soil water content under the assumption of steady state flow (Beven and Kirkby, 1979; O'Loughlin 1986). $\ln(a/\tan\beta)$, as one such terrain index, has been widely applied in hydrology. $\ln(a/\tan\beta)$represents the key hydrological processes controlling the spatial distribution of soil moisture in a simplified but realistic way. In this section, the relationship between $\ln(a/\tan\beta)$ and s is investigated over the Marmot Creek basin.

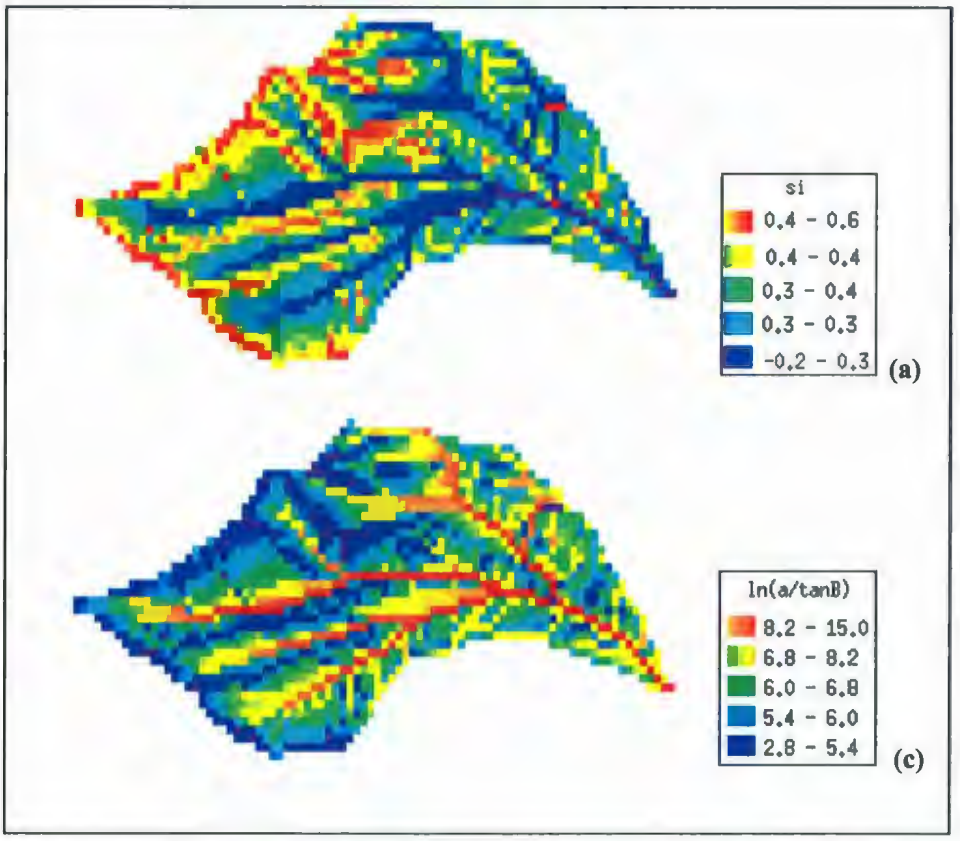

Figure 7-11: (a) is spatial distribution of s in the Marmot Creek basin, on 28th August, 2007, and (b) is the map of the spatial distribution of $\ln(a/\tan\beta)$.

Figure 7-11 shows the results of local soil deficit, s, on August 28th in 2007 using D8 with 90-meter resolution DEM to determine $\ln(a/\tan\beta)$. The daily simulated streamflow (5.795×10^{-4} m) on that day was only 4×10^{-7} m greater than the observed value (5.791×10^{-4} m). The result is obviously that the river network has the lowest soil moisture deficit. Any location in the watershed where $s\leq0$ is saturated and has the potential to produce saturation overland flow. Any location where $s<0$ produces return flow. When $s>0$, the soil is unsaturated.

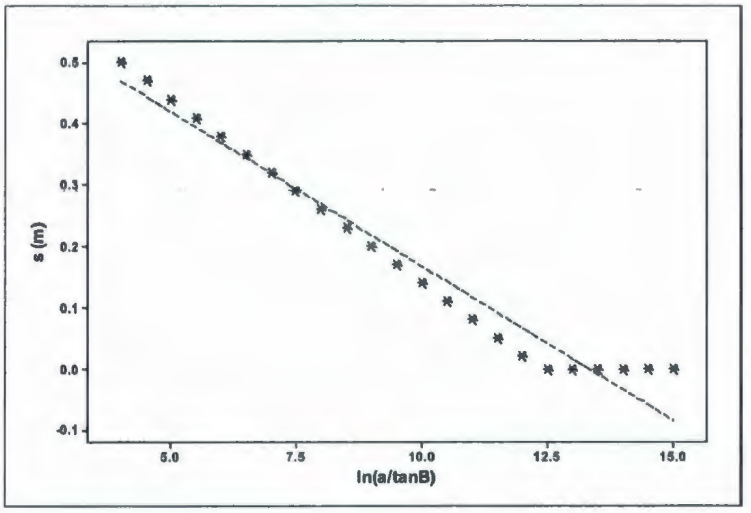

Figure 7-12: The linear relationship between s and ln(a/tanβ) in the Marmot Creek basin on 28th August, 2007.

In this study, the local s is estimated depending on the scaling parameter SZM, λ, $\bar{s}$ over the whole watershed, and local ln(a/tanβ) value. s, therefore, has a linear relationship with ln(a/tanβ). s will increase when the ln(a/tanβ) decreases (Figure 7-12). Large values of ln(a/tanβ) indicate the locations within a watershed most likely to be saturated and produce overland flow. These locations are topographically convergent and have gentle slopes and low transmissivity (Wolock, 1993).

Many previous studies have demonstrated that ln(a/tanβ) can explain less than half of the spatial variability in soil moisture. Moore *et al.* (1988) showed that ln(a/tanβ) explained 26 to 33% of the spatial variation in the soil moisture in a 0.075 km^2 watershed in New South Wales, Australia. Thompson (1996) presented that the relationship between depth to water table and ln(a/tanβ) was poor (explained variance of 26%) in lower-slope convergent zones in a 0.04 km^2 catchment in British Columbia, Canada. For a modeling perspective, the ready availability of digital terrain models still leads to ln(a/tanβ) being

one of the most common predictors used to estimate spatial moisture patterns, even in situations where $\ln(a/\tan\beta)$ may not represent the key controlling processes (Grayson and Western, 2001).

7.4. Summary

The application of TOPMODEL in the Marmot Creek basin situated in the Kananaskis Valley of Alberta shows that the model can be helpful in the study of runoff processes. The short term runoff simulation is reasonably successful, although particular runoff events are not always simulated satisfactorily. Reasonably good runoff prediction is achieved despite the relatively simple structure of the model. If the model could be combined with a sophisticated snow subroutine, this model could perhaps be used to simulate streamflow even in the winter season, but additional parameters would have to be included.

In this chapter, the effects of flow direction and DEM resolutions on the streamflow simulation are examined. When the parameters are fixed, model efficiencies with $\ln(a/\tan\beta)$ produced by D8 are better than those with $\ln(a/\tan\beta)$ determined by D∞. After the parameters are re-optimized, model efficiencies are virtually identical for the different flow directions and different grid sizes. The hydraulic conductivity increases as the grid size increases. This is due to compensation for the effects of changing DEM resolution on the $\ln(a/\tan\beta)$ distribution. A 1-meter resolution DEM is considered appropriate for hydrologic modeling in the Marmot Creek basin.There is a linear relationship between s and the $\ln(a/\tan\beta)$ distribution in the Marmot Creek basin. However, this relationship does not support most of previous works in this area.

Chapter 8

Exploration of the Relationship of Land Cover to the Topographic Index

Vegetation plays a crucial role in the land-atmosphere interactions through water transport in the form of evapotranspiration, carbon transport in the form of photosynthesis and respiration, temperature regulation, and so on. Determining the factors that affect the vegetation dynamics is an complex problem. The average spatial variability of vegetation depends on a variety of factors such as topographic attributes (elevation, slope, aspect, etc.), gradients of temperature, precipitation, radiation, land use, and land cover (Matsushita *et al.*, 2007).

The ability to measure land cover from satellites on a regional basis has come at a time when spatially distributed models of hydrologic processes are increasingly prominent in the literature (Kirkby 1971; O'Loughline, 1986). These hydrologic models rely heavily on topographic indices, such as drainage area, slope and hillslope curvature, when

making predictions. Given the close relationship between land cover and hydrologic process, there may also be linkages between the topographic indices and land cover.

In this chapter, the relation of $\ln(a/\tan\beta)$ with the land covers is examined in the Marmot Creek basin. A one-way analysis of variance (ANOVA) is employed for each class of land cover to determine if $\ln(a/\tan\beta)$ varied significantly over the classes. This study wants to determine if each class of land cover that can be described by what is known of $\ln(a/\tan\beta)$ of the site. Correlations or regressions between $\ln(a/\tan\beta)$ values and land cover classes cannot be calculated since it is not possible to associate sensible numerical values with many of the land cover classifications. Instead, ANOVA provides a means to determine whether or not the $\ln(a/\tan\beta)$ distributions change from one class of a land cover to another.

8.1. Land Cover Classification

8.1.1. Vegetation cover from remote sensing

Satellite-based remote sensing is the only practical way of monitoring vegetation pulses at the spatial scale. In this study, 4-meter resolution IKONOS images of the Marmot Creek basin are acquired for October 18th, 2003. The Geo Ortho IKONOS data (obtained from GeoEye Inc.) comprises four bans in the visible and near-infrared parts of the spectrum. The acquisition timing and general characteristics of the IKONOS data are summarized in Table 8-1.

Table 8-1: IKONOS performance characteristics and corresponding acquisitions

Specification	Value
IKONOS product type	Geo Ortho Kit
Spatial resolution	4 m
Panchromatic band	450-900 nm
Blue band	445-516 nm
Green band	506-595 nm
Red band	632-698 nm
NIR band	757-853 nm
Radiometric resolution	11bit
Orbit height	681 km
Acquisition dates (GMT)	2003-10-18 19:12
Cloud cover	0
Solar azimuth/ satellite azimuth	176.009°/179.94°
Solar zenith	29.36°
Sensor tilt angle	reverse
Data projection	WGS84

8.1.2. IKONOS Image Processing

Figure 8-1 illustrates the flowchart of multi-spectral IKONOS image preparation and processing procedures involved in this study. The steps include image orthorectification, atmospheric correction, vegetation index calculation, and land cover classification. All works are undertaken using ENVI Version 4.3 image processing software.

Aerial photos and satellite images may not show features in their correct locations due to displacements caused by the tilt of the sensor and terrain relief. Orthorectification transforms the central projection of the photograph into an orthogonal view of the ground, thereby removing the distorting effects of tilt and terrain relief. In this study, the Rational Polynomial Coefficients (RPC) sensor model is used to orthorectify data from the

IKONOS sensors. The RPC orthorectification process combines several sets of input data to place each pixel in the correct ground location.

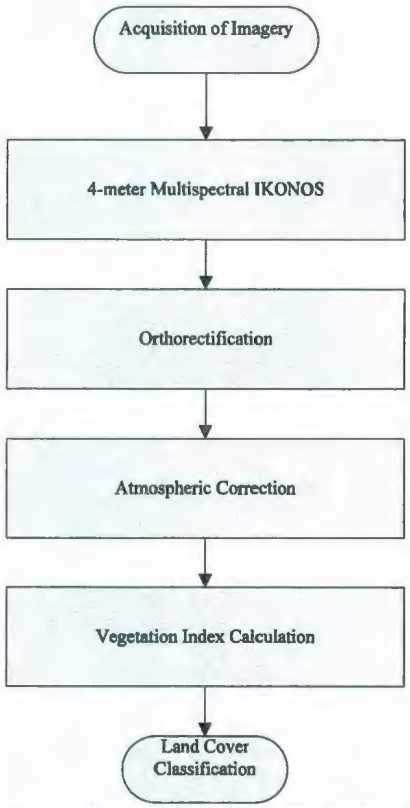

Figure 8-1: Processing workflow for the IKONOS imagery.

The objective of atmospheric correction is to retrieve the surface reflectance (that characterizes the surface properties) from remotely sensed imagery by removing the atmospheric effects. Atmospheric correction has been shown to significantly improve the accuracy of image classification. The primary atmospheric correction is achieved by Dark Subtract Utility in ENVI image process software. The images, before and after the corrections, are shown in Figure 8-2.

Figure 8-2: Images transformation for the October 18, 2003 image for the Marmot Creek basin. The left side of the images is the corrected image; while the right side of the images is the original 4-meter resolution red spectrum (a), and near-infrared image (b). Data is obtained from GeoEye Inc.

8.1.3. Vegetation Index

The vegetation index (VI), defined as the arithmetic combination of two or more bands related to the spectral characteristics of vegetation, has been widely used for the phonologic monitoring, vegetation classification, and biophysical derivation of radiometric and structural vegetation parameters (Huete and Justice, 1999). Among existing VIs, the Normalized Difference Vegetation Index (NDVI) is the most often used and is an operational, global-based vegetation index. It is partly due to its "ratio" properties, which enable the NDVI to cancel out a large proportion of the noise caused by

changing sun angles, topography, clouds or shadow, and atmospheric conditions (Huete and Justice, 1999). NDVI was defined by Rouse *et al.* (1974) as follow:

$$NDVI = \frac{\rho_{nir} - \rho_{red}}{\rho_{nir} + \rho_{red}} \qquad \text{Equation 8-1}$$

where ρ_{nir} and ρ_{red} represent reflectance at the red and near-infrared (NIR) wavelengths, respectively. Values of NDVI range from -1.0 to 1.0, where the negative values indicate non-vegetated surfaces such as water, ice, snow, clouds, etc., and the positive values indicate increasing density of green, healthy vegetation.

NDVI is created by ENVI image processing software for the IKONOS images to assist in classification of land cover across the Marmot Creek basin. This index is useful in separating vegetation communities due to the different spectral responses displayed by different land covers and vegetation communities.

8.1.4. Land Cover Classification

A Decision Tree classification approach is employed in this study to classify the land cover. The Decision Tree classifier performs multistage classifications by using a series of binary decisions to place pixels into classes. Each decision divides the pixels in a set of images into two classes based on an expression. Each new class can be divided into two more classes based on another expression. As many decision nodes as required can be defined. The results of the decisions are classes. Data from many different sources and files can be used together to make a single decision tree classifier. The decision trees can be "pruned" and edited interactively. The trees can be saved and applied to other data sets.

Figure 8-3 shows the decision tree in ENVI. In this study, the land cover is classified into four classes basing on the different NDVI ranges, which is summarized in Table 8-2.

Table 8-2: Land covers classes and their corresponding NDVI values.

Land Cover Classes	**NDVI Rang**
Snow or Water	NDVI<0.1
Bare Ground	0.1≤ NDVI < 0.2
Grass	0.2≤ NDVI<0.3
Tree	0.3≤ NDVI <0.8

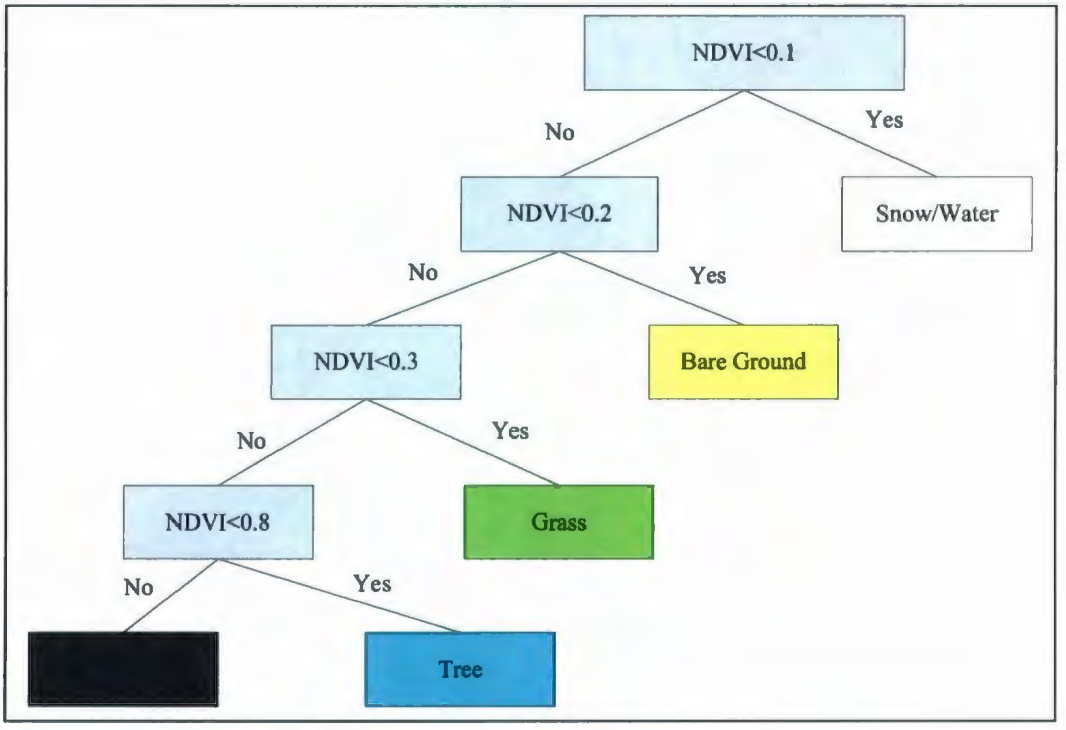

Figure 8-3: Decision tree for the land cover classification in this study.

8.2. Statistical Analysis Method

Since all of the land cover classes are qualitative rather than numerical, a non-ordinal technique (analysis of variance) is applied in this study. The initial techniques of the

analysis of variance were developed by the statistician and geneticist Fisher R.A. in the 1920s and 1930s, and are sometimes known as Fisher's ANOVA or Fisher's analysis of variance, due to the use of Fisher's F-distribution as part of the test of statistical significance. A one-way ANOVA is performed in this study for each land cover class to determine if $\ln(a/\tan\beta)$ values vary significantly over the classes. ANOVA provides a means to determine whether or not the $\ln(a/\tan\beta)$ distributions change from one class of land cover to another. Once a class that is associated with variation in the $\ln(a/\tan\beta)$ distribution has been identified, further attempts can be made to quantify the relationship. Various transforms of the data are applied to arrive at normal distributions of $\ln(a/\tan\beta)$ across all the land cover classes. The statistical analyses are performed using MINITAB Version 14.

8.3. Results and Discussions

8.3.1. Calculation of NDVI

For the purpose of this study, NDVI is created to assist in land cover classification. NDVI is a simple numerical indicator that can be used to analyze remote sensing measurements, and assess whether the target being observed contains different vegetations. Figure 8-4 shows the distribution map of NDVI across the Marmot Creek basin.

The white colour in the image shows that there was a snow cover on October 18th, 2003 in the Marmot Creek basin with an NDVI value of less than 0. The range of NDVI in this study area varies from -0.67 to 0.77, and the mean value of NDVI is 0.29. As can be seen in Figure 8-5, the frequency distribution curve of NDVI moves to higher values when NDVI values are in the range of 0.46-0.57. This indicates that forest occupies most of the

area in the Marmot Creek basin. Because the image is too large to be illustrated in 3-D scatter plots, 1056 samples from the image are randomly selected to demonstrate the variations of NDVI in terms of the different elevations and ln(a/tanβ) values (Figure 8-6). It should be noted that NDVI values vary from -0.2 to 0.5 with the changes in elevation and ln(a/tanβ).

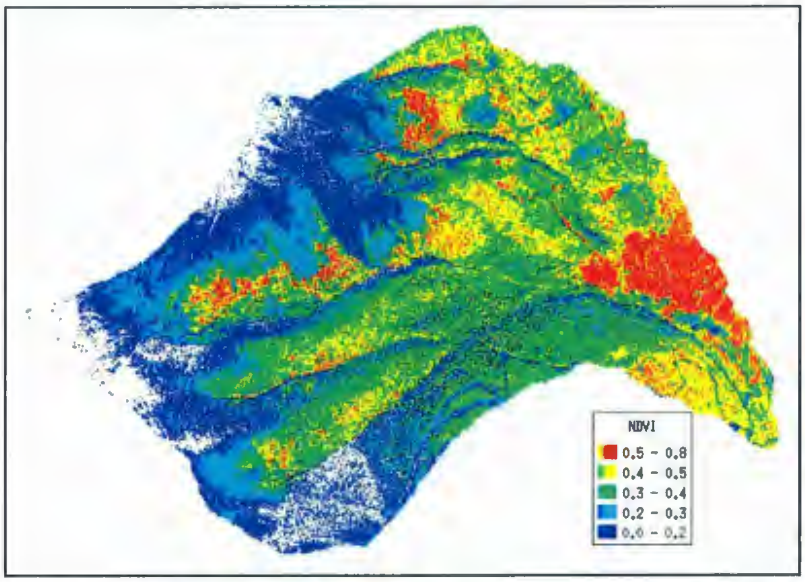

Figure 8-4: The spatial distribution of NDVI in the Marmot Creek basin.

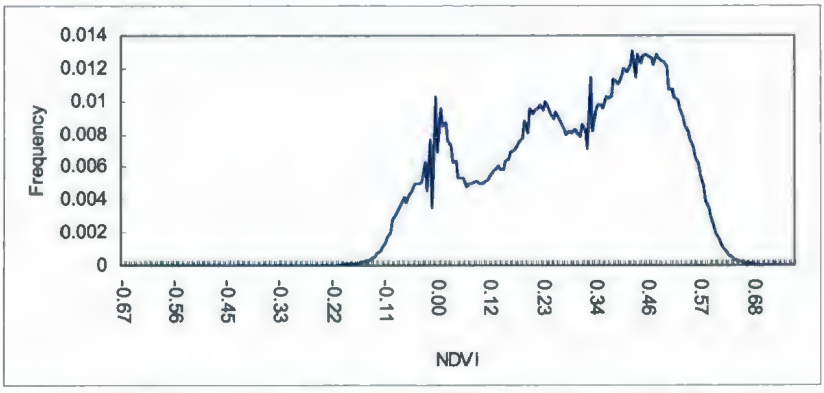

Figure 8-5: Frequency distribution of NDVI in the Marmot Creek basin.

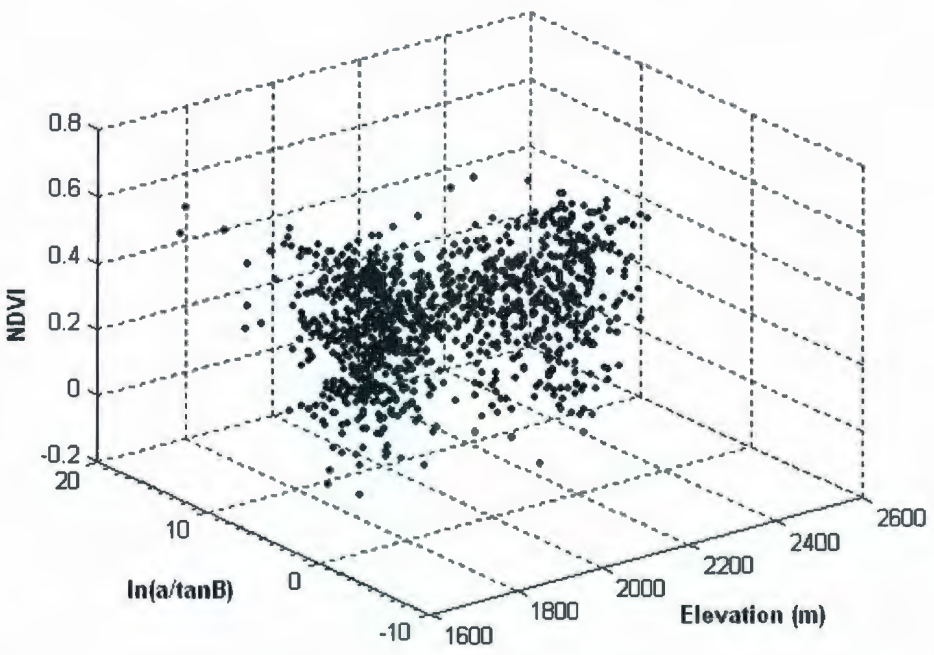

Figure 8-6: 3-D Scatter plots of NDVI of the randomly selected 1056 samples from the image.

The calculation of NDVI values turns out to be sensitive to a number of perturbing factors including atmospheric effects, clouds, soil effects, anisotropic effects, and spectral effects. The topographic effect is another very important factor, especially when the index is used in areas of rough terrain. For these reasons, NDVI should be used with great caution. In any quantitative application that necessitates a given level of accuracy, all the perturbing factors that could result in errors or uncertainties of that order of magnitude should be explicitly taken into account. This may require extensive processing based on ancillary data and other sources of information.

8.3.2. Results of the Land Cover Classification

In this research, the Decision Tree Classifier is applied to the IKONOS images for the land cover classification. Figure 8-7 shows the spatial distribution of the land cover across the Marmot Creek basin.

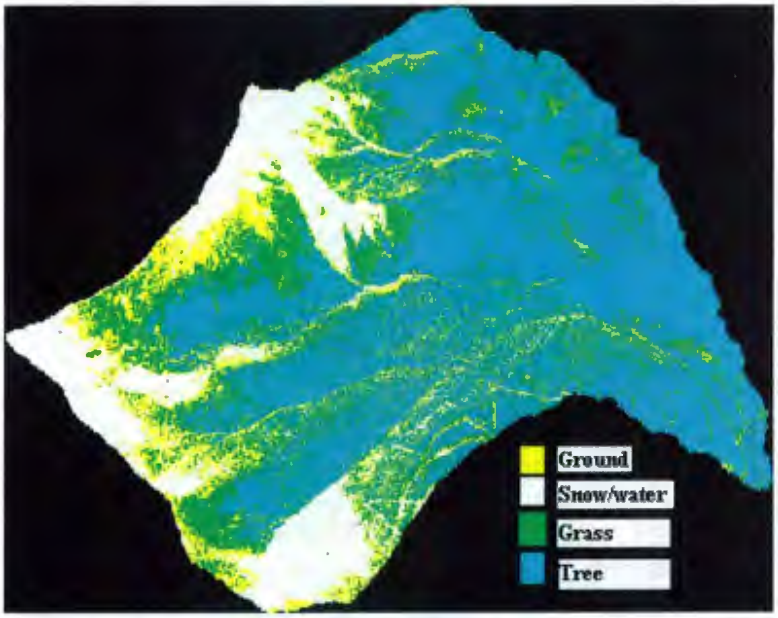

Figure 8-7: Spatial distribution of the land cover classes over the Marmot Creek basin.

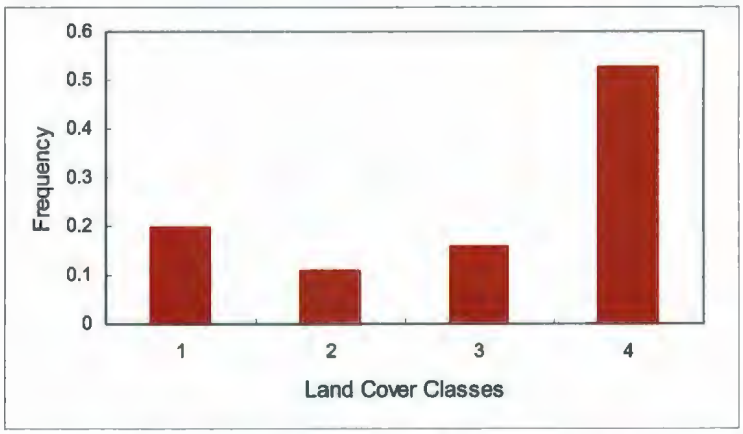

Figure 8-8: Frequency distribution of the different land covers in the Marmot Creek basin.

The land cover is classified into four groups in the Marmot Creek basin which are snow or water, bare ground, grass, and trees. From Figure 8-8, it can be found that forest has the highest frequency distribution, which equals approximately 53%. This result is also clearly displayed in Figure 8-7.

Kirby (1976) studied the vegetation distribution in the Marmot Creek basin. He showed that forest covered approximately 60% of the basin area from the basin outlet to the tree line. The remaining 40% of the area lies above the tree line and consists of alpine meadow (80%) and rock and Krummholz (20%).

In this study, 11.21% of the basin area is bare ground, 16.12% is grass, and 52.70% is forest. The discrepancy between these two studies may be attributed to the 19.97% of snow covered in the Marmot Creek basin on October 18th, 2003.

8.3.3. Exploration the variation of ln(a/tanβ) over the Land Cover Classes

Vegetation cover and ln(a/tanβ) data at 4 m grid cell resolution are derived for the Marmot Creek basin to investigate the relation between ln(a/tanβ) and different land covers. Figure 8-9 illustrates the spatial distributions of ln(a/tanβ). The correlation between ln(a/tanβ) and the different land covers is not pronounced if the judgment is only based on Figure 8-7 and 8-9. The variation of the land cover classes in terms of the different elevations and ln(a/tanβ) is illustrated in 3-D scatter plots (Figure 8-10). The distributions of bare ground (Class 2), grass (Class 3), and trees (Class 4) show no variation in elevations in the range of 2000-2600 m.

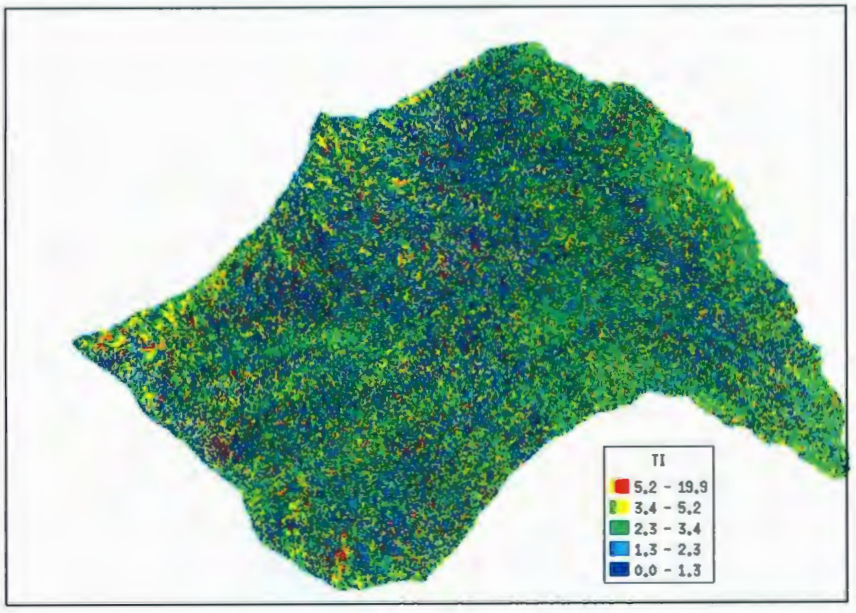

Figure 8-9: Spatial distribution of ln(a/tanβ) in the Marmot Creek basin.

From Figure 8-10(b), it seems that the trees have higher corresponding ln(a/tanβ) values than the other three land covers. However, there is no large discrepancy of the ln(a/tanβ) distribution between bare ground, grass or snow covers. In order to assess a further demonstration, a one-way ANOVA is adopted in this study. Because the 4-meter resolution images are too large to be analyzed in MINITAB, 288 samples are randomly selected from the original data.

As a first step in examining the differences in ln(a/tanβ) in relation to land cover class, the means and standard deviations of each ln(a/tanβ) for each class are calculated. The values are given in Table 8-3. ANOVA is performed on the means of ln(a/tanβ) for each group.

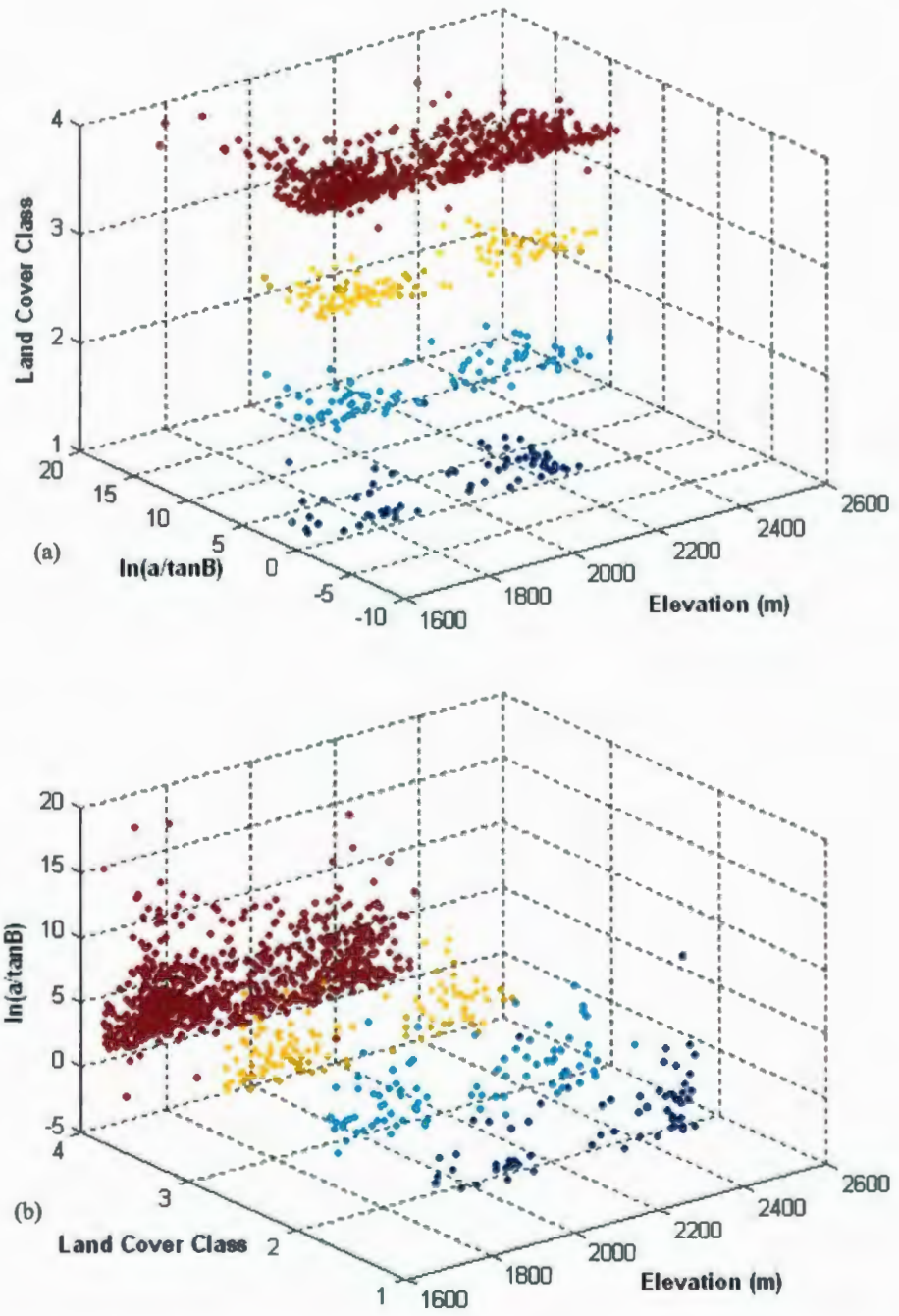

Figure 8-10: 3-D Scatter plots of land cover classes and ln(a/tanβ) of the randomly selected 1056 samples from the image.

Table 8-3: Statistical describing of ln(a/tanβ) over different land covers.

Variable	CLASS	Mean	StDev	Minimum	Median	Maximum
ln(a/tanβ)	**Snow or Water (1)**	3.308	2.287	0.547	2.222	8.687
ln(a/tanβ)	**Bare Ground (2)**	3.373	2.098	0.605	2.771	8.143
ln(a/tanβ)	**Grass (3)**	2.759	1.561	0.807	2.234	6.844
ln(a/tanβ)	**Tree (4)**	3.175	2.195	0.411	2.658	17.788

The results of ANOVA are presented graphically in Figures 8-11 and 8-12. F is the ratio of ln(a/tanβ) variance between classes. A small value of F indicates an insignificant change in the ln(a/tanβ) distribution from land cover class to land cover class. The p-value is equal to 0.75, which is greater than 0.05. This suggests that the variation of ln(a/tanβ) is not significant over the different land covers. Tukey's method (1953), a single-step multiple comparison procedure, is simultaneously used in conjunction with ANOVA to find which means are significantly different from one another. The test compares the means of every treatment to the means of every other treatment, and identifies where the difference between two means is greater than the standard error would be expected to allow. In this study, all the intervals include zero, which means the differences of ln(a/tanβ) between classes are statistically insignificant.

Pickup and Chewings (1996) studied the correlations between DEM-derived topographic indices and remotely-sensed vegetation cover in a mountain and piedmont area of arid central Australia. The authors pointed out that there was no obvious trend to be seen in the correlations between cover class and ln(a/tanβ).These two relations were also inconsistent, with both positive and negative values appearing for the same ln(a/tanβ) in different classes. This was probably because soil transmissivity was not included in this simple index due to a lack of data.

```
Source       DF     SS      MS     F     P
ln(a/tanβ)    3    0.518   0.173  0.40  0.750
Error       282  120.351  0.427
Total       285  120.869
S = 0.6533   R-Sq = 0.43%   R-Sq(adj) = 0.00%

                Individual 95% CIs For Mean Based on Pooled StDev
Level   N    Mean   StDev ---------+---------+---------+---------+
1      15  0.9507  0.7687 (----------------*----------------)
2      34  1.0237  0.6494         (----------*----------)
3      42  0.8592  0.5737   (----------*----------)
4     195  0.9457  0.6606          (---*----)
                           ---------+---------+---------+---------+
                                  0.80      1.00      1.20      1.40
Pooled StDev = 0.6533
Tukey 95% Simultaneous Confidence Intervals
All Pairwise Comparisons among Levels of ln(a/tanβ)
Individual confidence level = 98.92%

ln(a/tanβ)= 1 subtracted from:
ln(a/tanβ)  Lower   Center  Upper   +---------+---------+---------+---------
2           -0.4468  0.0730 0.5927        (----------------*----------------)
3           -0.5959 -0.0915 0.4129    (----------------*----------------)
4           -0.4543 -0.0050 0.4443        (-------------*-------------)
                                    +---------+---------+---------+---------
                                   -0.60     -0.30      0.00      0.30
ln(a/tanβ) = 2 subtracted from:
ln(a/tanβ)  Lower   Center  Upper   +---------+---------+---------+---------
3           -0.5513 -0.1644 0.2224     (-----------*-----------)
4           -0.3896 -0.0780 0.2336         (---------*---------)
                                    +---------+---------+---------+---------
                                   -0.60     -0.30      0.00      0.30
ln(a/tanβ) = 3 subtracted from:
ln(a/tanβ)  Lower   Center  Upper   +---------+---------+---------+---------
4           -0.1988 0.0864  0.3717           (--------*--------)
                                    +---------+---------+---------+---------
                                   -0.60     -0.30      0.00      0.30
```

Figure 8-11: One-way ANOVA test for ln(a/tanβ) versus classes.

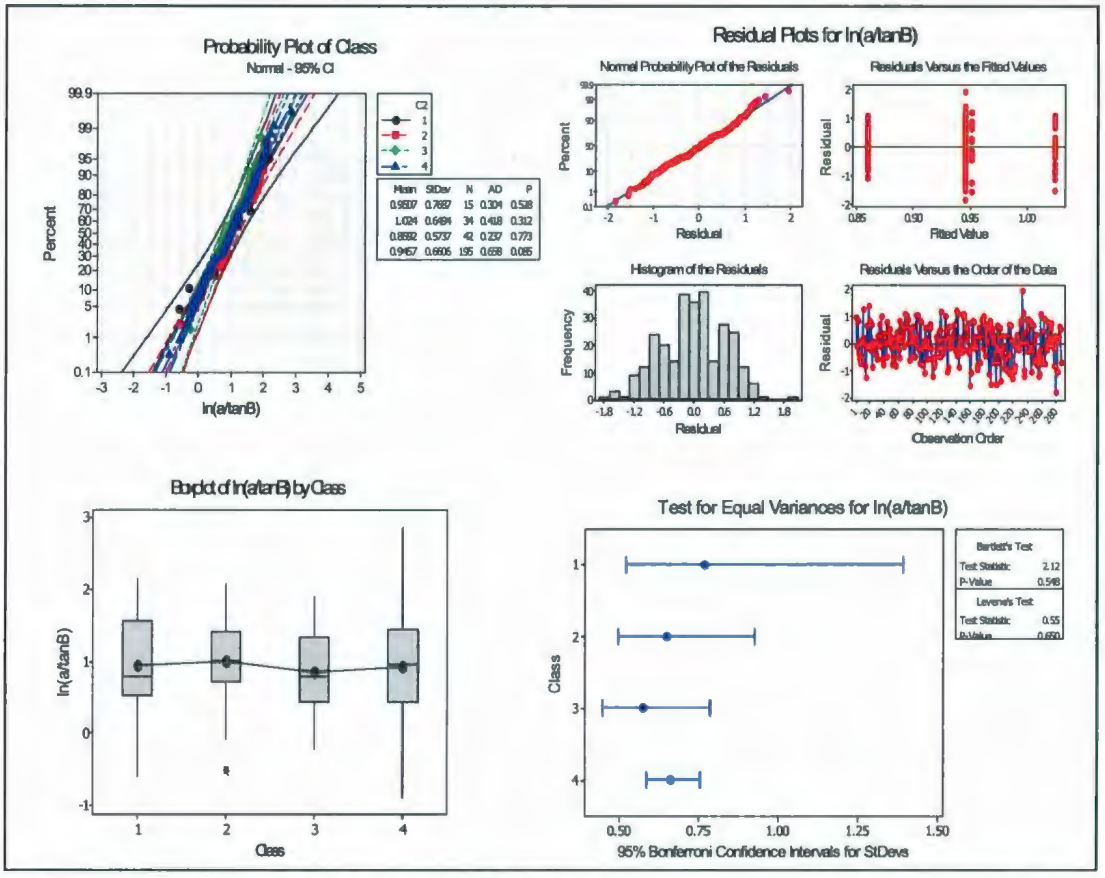

Figure 8-12: Normal distribution, residual plot, box plot, and constant variance test for ln(a/tanβ) versus land cover classes.

This study uses ANOVA to explore the relationship between ln(a/tanβ) and the land cover classes. The tests show that no obvious connection can be found between these two factors.

8.4. Summary

The objective of this chapter is to explore the relationship between ln(a/tanβ) and the different land cover classes. IKONOS satellite images on October 18th 2003 are used to

do land cover classification using Decision Tree classifier. From the land cover classification, it can be found that in the Marmot Creek basin, 11.21% of the area is bare ground, 16.12% area is the grass, and 52.70% area is the forest. The results of the one-way ANOVA show no obvious relationship between $\ln(a/\tan\beta)$ and the land cover classes can be determined.

Chapter 9

Conclusions and Recommendations

9.1. Conclusions

The purposes of this study are to examine the theory behind TOPMODEL, and to find the relation between $\ln(a/\tan\beta)$ and land cover classes. TOPMODEL combined with the GA is tested under steep topography in needle-leaf forested Marmot Creek basin in Alberta. Periods are chosen for the model calibration (from August to October 2007) and model validation (from August to September 2006). Snow free seasons are chosen to examine this model, because this version of TOPMODEL does not contain the snow component. PET, as one of the three input metrological data sets into TOPMODEL, is estimated by the Penman-Monteith function with r_a and r_c simulated by CLASS. r_a is also estimated by Monteith method (1965) in order to investigate its effects on PET. For the purpose of determining spatial variability on streamflow simulation, two resolution DEMs data, 1- and 90-meter, and two flow direction algorithms, D8 and D∞, are employed in this research. 4-meter resolution IKONOS satellite images are used to do land cover

classification across the Marmot Creek basin basing on NDVI values. The covers are divided into four classes, which are snow or water, bare ground, grass, and tree.

Based on the results and discussion described in former chapters, it can be concluded into five aspects.

i) Model performance

The model efficiencies of the calibration and validation periods are 0.611 and 0.332 for TOPMODEL simulations. Several reasons will cause the relative low efficiency model performance, like overestimating rainfall, errors in estimation of PET, ignoring the soil variability, and without the consideration of snow component which is a very important source of the streamflow in the Marmot Creek basin.

ii) PET Estimation

The estimated PET produced by Panmen-Monteith method is not sensitive to changing r_a in the Marmot Creek basin. r_c is the main controller for the transpiration compared with r_a.

iii) Effects of spatial variability

The mean value of $\ln(a/\tan\beta)$ increases as the grid size increasing. When using D∞, the mean values of $\ln(a/\tan\beta)$ are always greater than those calculated by D8. Although different grid sizes and flow direction algorithms generated various $\ln(a/\tan\beta)$ distributions, the simulated streamflow results are virtually identical when the parameters are optimized. Both 1- and 90-meter resolution DEMs are not very appreciated for the small steep watershed simulation.

iv) Streamflow generation mechanism

The dominant stream generation mechanism is the subsurface flow in the Marmot Creek basin. Subsurface flow accounts for 84.9% of the total simulated streamflow during the calibration periods.

v) $\ln(a/\tan\beta)$ effects on soil moisture and land cover classes

$\ln(a/\tan\beta)$ has a linear relationship with s. The local s will decrease along with the increment of the local $\ln(a/\tan\beta)$. Therefore, the locations with the relative high $\ln(a/\tan\beta)$ values will saturate first. There is no obvious relationship between $\ln(a/\tan\beta)$ and land cover classes. Elevation may have the dominant effect on the land cover distribution.

9.2. Recommendations

Four recommendations are proposed to improve this study in the future:

i) Field measurement of parameters

It is recommended that a physical range for each parameter be established from field measurements, especially for the saturated hydraulic conductivity. The spatial variability of parameters affects the results of streamflow simulation.

ii) Rainfall data in the model simulation

Rainfall, as the major input data for TOPMODEL, should be measured at more stations among the forest in the Marmot Creek basin. The rainfall data sets used in this simulation are obtained from the Hey Meadow metrological station which is covered with grass. Therefore, the rainfall is overestimated in this simulation without the consideration of interruption of the trees.

iii) PET estimation

PET is used to estimate the actual evapotranspiration in TOPMODEL simulation. The Penman-Monteith method is limitied to precisely calculate PET, a further study in PET estimation is recommended.

iv) DEM resolution and flow direction algorithms

Both D8 and D∞ are single flow direction algorithms. This limitation becomes increasingly important on convex slopes. More suitable flow direction algorithms are suggested to determine the flow direction of the streamflow. As 1-meter resolution DEM has huge data to process and 90-meter resolution DEM does not work well to the hydrologic simulation in hillslope watershed, a more appropriate resolution DEM is recommend.

v) Improved TOPMODEL

In the Marmot Creek basin most of the streamflow results from the melting of snow. Snow as the most important component in this watershed is ignored in TOPMODEL simulation. Although the calibration period is snow free, the streamflow is still significantly affected by the snow. This will result in the poor prediction. TOPMODEL combined with a sophisticated snow subroutine is highly recommended to improve our simulation in the future.

References

Alapaty K., Pleim J., Raman S., Niyogi D., and Byun D., 1997, Simulation of atmospheric boundary layer processes using localand nonlocal-closure schemes, J. Appl. Meteor., 36: 214-233.

Andrew W.W., Rodger B.G., Gu¨nter Blo¨sch, Garry R.W., and Thomas A.M., 1999, Oberseved spatial organization of soil moisture and its relation to terrain indices, Water Resources Research, 35(3):797-810.

Avissar R., 1993, Observation of leaf stomatal conductance at the canopy scale: an atmospheric modeling perspective, Boundary-Layer meteorology 64:127-148.

Bailey W.G., and Davies J.A., 1981, The effect of Uncertainty in Aerodynamic Resistance on Evaporation Estimates from the Combination Model, Boundary-Layer Meteorology, 20:187-199.

Band L.E., Mackay D.S., and Creed I.F., 1996, Ecosystem Processes at the Watershed Sale: Sensitivity to Potential Climate Change, Limnol. Oceanogr, 41(5):928-938.

Bartlett P.A., McCAUGHEY J.H., Lafleur P.M., and Versegy L.A., 2003, Modelling Evapotranspiration at Three Boreal Forest Stands Using the CLASS: Tests of

Parameterizations for Canopy Conductance and Soil Evaporation, International Journal of Climatology, 23:427-451.

Beke G.J., 1969, Soils of three experimental watersheds in Alberta and their hydrologic significance, Ph. D. thesis, Univ. of Alberta, Dep. Soil Sci., Edmonton.

Beven K.J., and Kirkby M.J., 1979, A physically based, variable contributing area model of basin hydrology, Hydrological Science Bulletin, 24(1):43-69.

Beven K.J., and Wood E.F.,1983, Catchment geomorphology and the dy-namics of runoff contributing areas, Journal of Hydrology , 65:139-158.

Beven K.J., 1987, Towards the use of catchment geomorphology in flood frequency predictions, Earth Surf. Processes Landforms, 12: 69-82.

Beven K.J., Lamb R., Quinn P., Romanwicz R., and Freer J., 1995, TOPMODEL, In: V.P. Singh (Ed). Computer Models of Watershed Hydrology, Water Resource Publications, Highlands Ranch, CO., 627-668.

Beven K.J., 2001, Rainfall-Runoff Modelling: the Primer, Wiley, Chichester.

Biftu G.F., and Gan T.Y., 2000, Assessment of evapotranspiration models applied to a watershed of Canadian Prairies with mixed land-uses, Hydrological Processes, 14:1305-1325.

Bigelow S., 2001, Evapotranspiration modeled from stands of three broad-leaved tropical trees in Costa Rica, Hydrological Processes, 15:2779-2796.

Brown K.W., and Rosenberg N. J., 1973, A resistance model to predict vapotranspiration and its application to sugar beer field, Agronomy J., 68: 635-641.

Bruneau P., Gascuel-Odoux C., Robin P., Merot P., and Beven K., 1995, Sensitivity to space and time resolution of a hydrological model using digital elevation data, Hydrological Processes, 9:69-81.

Brutseart W., 1984, Gas Transfer at Water Surfaces, Dordrecht, D. Reidel Publishing Company.

Byun W.D., 1990, On the analytical solutions of flux-profile relationships for the atmospheric surface layer, J. Appl. Meteorol., 29:652-657.

Chen J.M., Rich P.M., Gower S.T., Norman J.M., and Plummer S., 1997, Leaf area index of boreal forests: theory, techniques, and measurements, Journal of Geophysical Research, 29:429-29 443.

Chen S., Liu Y., and THOMAS A., 2006, Climatic change on the Tibetan Plateau: potential evapotranspiration trends from 1961-2000, Climatic Change, 76:291–319.

Choudhury B.J., Reginato R.J., and Idso S.B., 1986, An analysis of infrared temperature observations over wheat and calculation of latent heat flux, Agric. Forest Meteorol., 37:75-88.

Clark C.O., 1945, Storage and the Unit Hydrograph, Transactions, ASCE, 110:1416-1446.

Costa-Cabral M.C., and Burges S.J., 1994, Digital elevation model networks (DEMON): A model of flow over hillslopes for computation of contributing and dispersal areas, Water Resources Research, 30:1681-1692.

Dargic T.C.D., 1984, On the integrated interpretation of indirect site ordinations: a case study using semi-arid vegetation in Southeaster Spain, Vetetation, 55:37-55.

Dargic T.C.D., 1987, An ordination analysis of vegetation patterns on topoclimate gradients in Southeaster Spain, Biogeography, 14:197-211.

Dingman S.L., 2002, Physical Hydrology, second edition.

Dolman A.J., and van den Burg G.J., 1988, Stomatal behaviour in an oak canopy, Agricultural and Forest Meteorology, 43: 99-108.

Fairfield J., and Leymarie P., 1991, Drainage networks from grid digital elevation models, Water resources research, 27:709-717.

Franchini M., Wensling M.J., Obled C., and Todini E., 1996, Physical interpretation and sensitivity analysis of the TOPMODEL, Journal of Hydrology, 175:293-338.

Freeze R.A., 1972, Role of subsurface flow in generating surface runoff, I. Baseflow contributions to channel flow, Water Resources Research, 8: 609-623.

Garratt J.R., 1993, Sensitivity of climate simulations to land-surface and atmospheric boundary-layer treatments—A review, International Journal of Climatology, 6: 419-449.

Güntner A., Uhlenbrook S., Seibert J., and Leibundgut C., 1999, Estimation of saturation excess overland flow areas—comparison of topographic index calculations with field mapping, IAHS Publ., 254: 203-210.

Grace J., Rasehum F.E., and Dixon M., 1980, Boundary layer conductance of the leaves of some tropical timber trees, Plant, Cell and Environment, 3: 443-450.

Granier A., Loustau D., Br'eda N., 2000, A generic model of forest canopy conductance dependent on climate, soil water availability and leaf area index, Annals of Forest Science, 57: 755-765.

Grismer M.E., Orang M., Snyder R., and Matyac R., 2002, Pan Evaporation to Reference Evapotranspiration Conversion Methods, J. Irrigation and Drainage Engineering, 128(3):180-184.

Hatfield J.L., Perrier A., and Jackson R.D., 1983, Estimation of evapotranspiration at one-time-of-day using remotely sensed surface temperature, Agric. Water Manage., 7: 341-350.

Hay L.E., and McCabe G.J., 2002, Spatial Variability in Water Balance Model Performance in the Conterminous United States, Journal of the American Water Resources Association, 38(3):847-860.

Holko L., and Lepisto A., 1996, Modelling the Hydrological Behavier of Mountain Catchment Using TOPMODEL, Journal of Hydrology, 196:361-377.

Holmgren P., 1994, Topographic and geochemical influence on the forest site quality, with respect to Pinus sylvestris and Picea abies in Sweden, Scandinavian Journal of Forest Research, 9(1):75-82.

Hornberger G.M., Beven K.J., Cosby B.J., and Sappington D.E., 1985, Shenandoah Watershed Study: Calibration of a topography-based, variable contributing area hydrological model to a small forested catchment, Water Resources Research, 2:1941-1850.

Horngerger G.M., Raffensperger J.P., Wiberg P.L., and Eshleman K.N., 1998, Elements of Physical Hydrology, The John Hopkinks University Press, Baltimore, Maryland, USA.

Huete A.R., and Justice C., 1999, MODIS vegetation index (MOD13) algorithm theoretical basis document, Ver. 3.

Ingrid H., and Dieter H., 1981, Potential evapotranspiration in mountain geoecosystems of different altitudes and latitudes, Mountain Research and Development, 1(3-4): 267-274.

Iorgulescu I., and Jordan J.P., 1994, Validation of TOPMODEL on a small Swiss catchment, Journal of Hydrology, 159:255-273.

Itenfisu D., 1998, Adaptation resistance-based evapotranspiration function to row crops, PHD thesis, Utah State University.

Jenson S.K., and Domingue J.O., 1988, Extracting topographic structure from digital elevation data for geographic information system analysis, Photogramm. Eng. Remote Sens., 54:1593-1600.

Jensen M.E., Burman R.D. and Allen R.G. (Ed.), 1989, Evaporation and Irrigation Water Requirements, ASCE, Manuals and Reports on Engineering Practice no. 70.

Kite G.W., and Droogers P., 2000, Comparing evapotranspiration estimates from satellites, hydrological models and field data, Journal of Hydrology, 229:3-18.

Kirby C.L., and Ogilvie R.T., 1969, The forest of Marmot Creek watershed research basin, Can.For.Ser.Publ.No.1259.

Kirkby M., 1975, Hydrograph modeling strategies. In Peel R., Chisholm M. and Haggett P. (eds) Processes in Physical and Human Geography, Heinemann, London, 69-90.

Kirkby M., Atkinson K., and Lockwood J.G., 1990, Aspect, vegetation cover and erosion on semi-arid hillslopes, in Vegetation and Geomorphology, editor J.Thomes, John Wiley, 25-39.

Krauth L.G., 1999, Hydrologic Modeling of Floods in an Eastern Kentucky Catchment Using TOPMODEL, Master Thesis, University of Louisville Speed Scientific School.

Lafleur P.M., 1992, Energy balance and evapotranspiration from a subarctic forest, Agricultural and Forest Meteorology, 58:163-175.

Lee H.N., 1997, Notes and correspondence: improvement of surface flux calculation in the atmospheric surface layer, J. Appl. Meteorol., 36:1416-1423.

Lindroth A., 1985, Canopy conductance of coniferous forests related to climate, Water Resources Research, 21: 297-304.

Liu J., Chen J.M., and Cihlar J., 2003, Mapping evapotranspiration based on remote sensing: an application to Canada's landmass, Water Resources Research, 39(7):1189.

Long I.F., Monteith J.L., Penman H.L., and Szeicz G., 1964, The plant and its environment, Meteor, Rundschau, 17(4):97-101.

Louis J.F., 1979, A parametric model of vertical eddy fluxes in the atmosphere, Boundary-Layer meteorology, 17:187–202.

Louis J.F., Tiedtke M., and Geleyn J.F., 1982, A short history of the operational PBL-Parameterization of ECMWF, Workshop on planetary boundary layer parameterization, European center for Medium Range Weather Forecasts, Shinfield Park, Reading Berks, UK.

Mahrt L., and Ek M., 1984, The influence of atmospheric stability on potential evaporation, J. Clim. Appl. Meteorol., 23: 222-234.

Matsushita B., Yang W., Chen J., Onda1 Y., and Qiu G., 2007, Sensitivity of the Enhanced Vegetation Index (EVI) and Normalized Difference Vegetation Index (NDVI) to Topographic Effects: A Case Study in High-Density Cypress Forest, Sensors, 7:2636-2651.

Mcguffie K., and Henderson-Sellers A., 2001, Forty Year of Numerical Climate Modeling, International Journal of Climatology, 21:1067-1109.

Monteith J.L., 1965, Evaporation and environment, Symp. Soc. Exp. Biol, 19: 205-234

Monteith J. L., 1973, Principles of Environmental Physics, Arnold, Paris.

Monteith J.L., 1981, Evaporation and surface temperature, Quarterly Journal of the Royal Meteorological Society, 107: 1-27.

Monteith J.L., and Unsworth M.H., 1990, Principles of environmental physics, Edward Arnold, New York, 291.

Moore I.D., Burch G.J., and Mackenzie D.H., 1988, Topographic effects on the distribution of surface soil water and the location of ephemeralgullies, Trans. Am. Soc. Agric. Eng., 31:1098-1107.

Moore I.D., Grayson R.B., and Ladson A.R., 1991, Digital terrain modelling: A review of hydrological, geomorphological, and biological applications, Hydrologic Process, 5:3-30.

Nash J.E., and Sutcliffe J.V., 1970, River flow forecasting through conceptual models part I — A discussion of principles, Journal of Hydrology, 10(3):282-290.

Nemani R., Keeling R.C.D., Hashimoto H., Jolly W.M., Piper S.C., Tucker C.J., Mtneni R.B., and Running S.W., 2003, Science, 300:1560-1568.

Niyogi, D.S., Raman S., Alapaty K., 1997, Comparison of Four Different Stomatal Resistance Schemes Using FIFE Data. Part II: Analysis of Terrestrial Biospheric-Atmospheric Interactions, J. Appl. Meteor., 36:903-917.

O'Callaghan J.F., and Mark D.M., 1984, The extraction of drainage networks from digital elevation data, Computer Vision, Graphics and Image Processing, 28:323-344.

Osborn G.D., and Jackson L.E., 1974, Physical environment, In the Mountain Environment and Urban Society, Kananaskis Centre for Environmental Research, Univ.of Calgary, Alberta. Kananaskis, 53-150.

Pan F.F, Peters-Lidard C.D., Sale M.J., and King A.W., 2004, A comparison of geographical information systems-based algorithms for computing the TOPMODEL topographic index, Water Resources Research, 40.

Paw U.K., and Meyers T.P., 1987, Zero plane displacement and roughness length variation with stability as predicted by turbulence closure model, Proceedings of the 18th Conference for Agricultural Forest Meteorology and 8th Conference of Biometeorology, West Lafayette, Indiana, April.

Pickup G., and Chewings V.H., 1996, Correlations between dem-derived topographic indices and remotely-sensed vegetation cover in rangelands, Earth Surface Processes and Landforms, 21:517-529.

Pitman A.J., 2003, Review: The evolution of, and revolution in, Land Surface Schemes designed for climate models, International Journal of Climatology, 23: 479-510.

Riou C., 1982, Une expression analytique du flux de chaleur sensible enconditions.

Quinn P.F., Beven K., and Freer J., 1993. TOPMODEL as an application module within WIS. In: K.Kovar and H.P. Nachtnebel (eds.). HydroGIS 93: Application of Geographic Information Systems in Hydrology and Water Resources, IAHS, 211:211-223.

Rouse J.W., Haas R.H., Schell J.A., and Deering D.W., 1974, Monitoring vegetation system in the great plains with ERTS, Proceedings of the Third Earth Resources Technology Satellite-1 Symposium, Greenbelt, USA, NASA SP-351, 3010-3017.

Rutter A.J., 1972, Transpiration, Oxford University Press, London.

Seibert J., Bishop K.H., and Nyberg L., 1997, A test of TOPMODEL's ability of predict spatially distributed groundwater levels, Hydrological Processes, 11:1131-1144.

Seibert J., and McGlynn B. L., 2007, A new triangular multiple flow direction algorithm for computing upslope areas from gridded digital elevation models, Water Resources Research, 43.

Singh T., and Kalra Y.P., 1972, Water quality of an experimental watershed during the calibration period, Trans, Am. Geophys. Union, 54:139.

Sklash M.G., 1978, The role of groundwater in storm and snowmelt runoff generation, Ph.D., thesis, University of waterloo, Waterloo, Ontario.

Stevenson D.R., 1967, Geological and groundwater investigations in the Marmot Creek experimental basin of southwestern Alberta, Canada, M.Sc. thesis, University of Alberta, Edmonton, Alberta.

Storr D., Tomlain J., Cork H.F., and Munn R.E., 1970, An energy budget study above the forest canopy at Marmot Creek, Alberta, 1967, Water Resources Research, 6(3).

Tarboton D.G., 1997, A new method for the determination of flow directions and upslope areas in grid digital elevation models, Water Resources Research, 33(2):309–319.

Telang S.A., Baker B.L., Costerton J.W., Ladd T., Mutch R., Wallis P.M., and Hodgson G.W., 1982, Biogeochemistry of Mountain Stream Waters: the Marmot System, Inland Waters Directorate, Ottawa, Canada.

Thom A. S., 1968, The exchange of momentum, mass and heat between an artificial leaf and the air- flow in a wind-tunnel, Q.J.R.Met.Soc., 9J, 399:44-56.

Thom A.S., 1972, Momentum, mass and heat exchange of vegetation, Q.J.R.Met.Soc., 98:124-134.

Thornthwaite C.W, 1948, An Approach Toward a Rational Classification of Climate, Geograph. Rev., 38 (1):55-94.

Thornthwaite C.W., and Hare F.K., 1965, The loss of water to the air, Agricultural Meteorology, 6(28):163-180.

Tukey J., 1953, Multiple comparisons, Journal of the American Statistical Association, 48:361-376.

Velázquez-Rosas N., Meave J., and Vázquea-Santana, 2002, Elevation variation of leaf traits in montane rain forest tree species at La Chinantla, Southern Mexico, Biotropica, 34(4):534-546.

Verma S.B., Rosenberg N.J., Blad B.L., and Baradas M.W., 1976, Resistance-energy balance method for predicting evapotranspiration: Determination of boundary layer resistance and evaluation of error effects, Agronomy J., 68:776-782.

Verseghy D.L., 1991, CLASS—a Canadian land-surface scheme for GCMs. I. Soil model, International Journal of Climatology, 11:111-133.

Verseghy D.L., McFarlane N.A., and Lazare M., 1993, CLASS—a Canadian land-surface scheme for GCMs. II. Vegetation model and coupled runs, International Journal of Climatology, 13: 347-370.

Verseghy D.L., 2000, The Canadian Land Surface Scheme (CLASS): Its History and Future, ATMOSPHERE-OCEAN, 38: 1-13.

Viney N.R., 1991, An empirical expression for aerodynamic resistance in the unstable boundary layer, Boundary-Layer meteorology, 56: 381-393.

Wallis P.M., 1978, Source, transportation and Utilization of dissolved organic matter in the groundwater and streams, Ph.D., thesis, University of waterloo, Waterloo, Ontario.

Wang J., and Georgakakos K.P., 2007, Estimation of potential evapotranspiration in the mountainous Panama Canal watershed, Hydrological Processes, 21:1901-1917

Western A.W., Grayson R.B., Blo¨schl G., Willgoose G.R., and McMahon T.A., 1999, Observed spatial organisation of soil moisture and its relation to terrain indices, Water Resources Research, 35:797- 810.

Western A.W., Grayson R.B., and Blo¨schl G., 2002, Scaling of soil moisture: A hydrologic perspective, Annu. Rev. Earth Planet. Sci., 30: 149-180.

Wikipedia, 2008, http://en.wikipedia.org/wiki/Krummholz.

Wilson D.J., Western A.W., and Grayson R.B., 2004, Identifying and quantifying sources of variability in temporal and spatial soil moisture observations, Water Resources Research, 40.

Wolock D.M., and Hornberger G.M., 1991, Hydrological effects of changes in atmospheric carbon dioxide levels, J. Forecasting, 10:105-116.

Wolock D.M., 1993, Simulating the variable-source-area concept of streamflow generation with the watershed model TOPMODEL, U.S. Geological Survey Water-Resources Investigations Report, 93-4124

Wolock D.M., and Price C.V., 1994, Effects of Digital Elevation Model Map Scale and Data Resolution on a Topography-Based Watershed Model, Water Resources Research, 30: 3041-3052.

Wolock D.M., 1995, Effects of subbasin size on topographic characteristics and simulated flow paths in Sleepers River watershed, Vermont, Water Resources Research, 31(8): 1989-1997.

Wolock D.M., and McCabe G.J., 1995, Comparison of single and multiple flow-direction algorithms for computing topographic parameters in TOPMODEL, Water Resources Research, 31:1315-1324.

Xie X., 1988, An improved energy balance-aerodynamic resistance model used estimation of evapotranspiration on the wheat field, Acta Meteorology, 46:102-106.

Yang K., Tamai N., and Koike T., 2001, Analytical solution of surface layer similarity equations, J. Appl. Meteorol., 40:1647-1653.

Zhang W., and Montgomery D. R., 1994, Digital elevation model grid size, landscape representation, and hydrologic simulations, Water Resources Research, 30: 1019-1028.